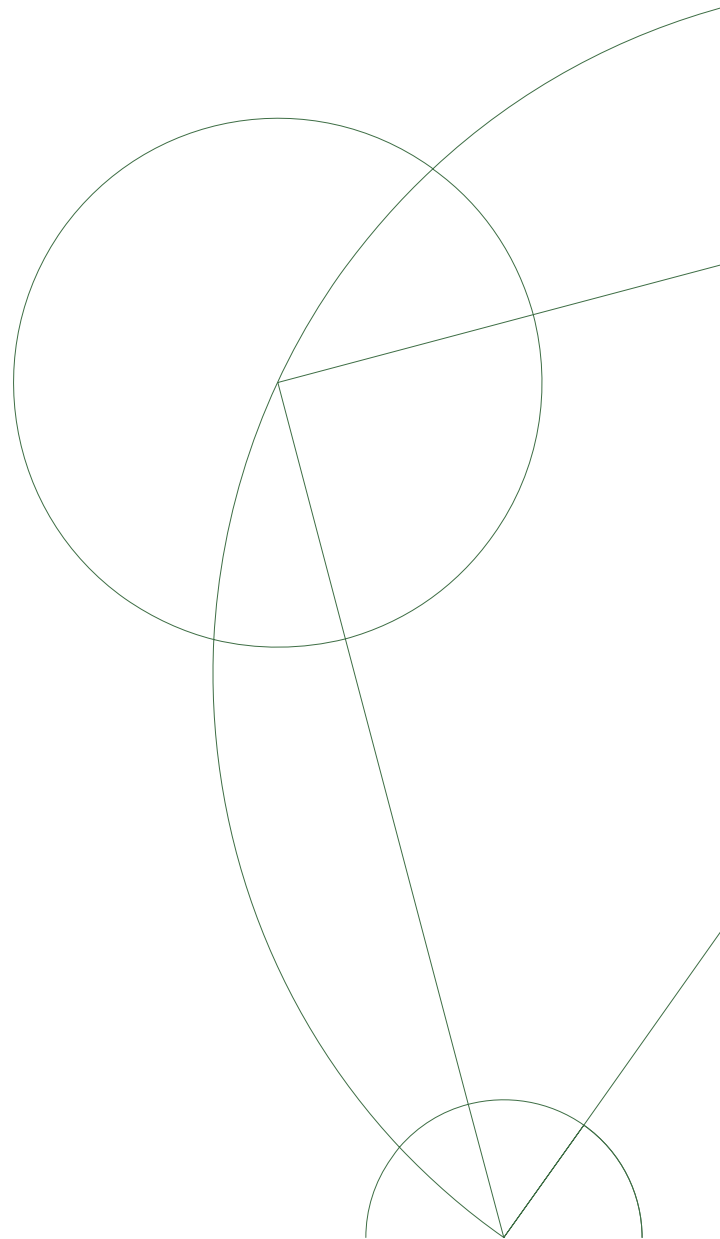Master's thesis

Measurement of the Tau Polarization in $Z \to \tau\tau$ Decays with the ATLAS Detector

Ingrid Deigaard

Summary in English

This thesis presents a measurement of the tau polarization in Z decays in proton-proton collision at $\sqrt{s} = 7$ TeV. The measurement is based on 4.6 fb^{-1} data that was collected in 2011 with the ATLAS experiment situated at the Large Hadron Collider.

The tau polarization in Z decays describes the degree of parity violation by the neutral weak current in the electroweak theory of particle physics. It describes furthermore how strongly the electroweak theory mixes quantum electrodynamics and the weak theory.

A key parameter in the extraction of the tau polarization result is the knowledge of the tau helicity in simulation on an event by event basis. Unfortunately, the tau helicity was not saved in the ATLAS simulations. To be able to measure the tau polarization, a method for re-establishing the tau helicity event by event has been developed.

To separate $Z \rightarrow \tau\tau$ from background, a selection has been performed. Events containing a muon and a hadronically decayed tau was selected, and the tau polarization was measured on the hadronic tau decay. All the electroweak backgrounds, except the $W \rightarrow \ell\nu$ background, were estimated from Monte Carlo simulations. Due to an imprecise description in the simulation of the probability of QCD jet be identified as a tau, the $W \rightarrow \ell\nu$ background estimated from simulation was normalized by a data driven study. The multijet background was estimated with a completely data driven technique.

The polarization was measured in one prong hadronic tau decays, by use of a variable that measures the energy asymmetry between charged and neutral pions. Templates from right- and left-handed taus were fitted to the data. A measurement of the tau polarization was performed and the systematic uncertainties on background and signal were investigated. The result of the measurement was

$$P_\tau = -0.258 \pm 0.048(\text{stat.}) \pm 0.028(\text{MC}) \pm 0.073(\text{sys.})$$

where (stat.) refers to the statistical uncertainty of the fit, (MC) refers to the uncertainty arising from limited statistics in the simulations, and (sys.) refers to the systematic uncertainty.

Resumé på Dansk

Denne afhandling omhandler målingen af polarisationen af tauer i Z-henfald i proton-proton-sammenstød ved kollisionsenergien $\sqrt{s} = 7$ TeV. Målingen er baseret på 4.6 fb^{-1} data indsamlet i 2011 af ATLAS eksperimentet, der er en del af Large Hadron Collider-komplekset på CERN.

Polarisationen af tauer i Z-henfald beskriver, hvor kraftigt paritet brydes af den neutrale, svage strøm i partikelfysikkens elektrosvage teori. Derudover beskriver tauernes polarisationen, hvor meget den elektrosvage teori mikser kvanteelektrodynamik og den svage teori.

En af de vigtigste parametre, når man måler polarisation af tauer, er kendskab til tauens helicitet i hver enkelt begivenhed i simuleringerne. Tauernes helicitet blev desværre ikke gemt i simuleringerne fra ATLAS. For at kunne måle polarisationen af tau blev der udviklet en metode til at gendanne og tildele helicitet af tauerne i hver enkelt begivenhed.

For at kunne adskille $Z \rightarrow \tau\tau$-begivenheder fra baggrundsbegivenheder lavedes en udvægelsesproces. Begivenheder med en muon og en hadronisk henfaldet tau blev udvalgt, og polarisationen af tauerne blev målt på den hadronisk henfaldne tau. Alle elektrosvage baggrundsbegivenheder på nær $W \rightarrow \ell\nu$ blev estimeret ud fra Monte Carlo simuleringer. På grund af en upræcis beskrivelse i simulering af sandsynligheden for at en QCD jet ville blive identificeret som en tau, blev $W \rightarrow \ell\nu$-baggrunden estimeret ud fra simuleringer og normaliseret ved hjælp af et studie drevet af data. Multijetbaggrunden blev estimeret med en teknik fuldstændigt drevet af data.

Polarisationen af tauer blev målt i et-prong hadroniske tauhenfald ved hjælp af en variabel, som måler asymmetrien af energi af ladede og neutral pioner. Fordelinger af højre- og venstrehåndede tauer blev fittet til data. Målingen af tauernes polarisation blev udført, og de systematiske usikkerheder fra både baggrund og signal blev undersøgt. Resultatet af målingen var

$$P_\tau = -0.258 \pm 0.048(\text{stat.}) \pm 0.028(\text{MC}) \pm 0.073(\text{sys.})$$

hvor (stat.) angiver den statistiske usikkerhed af fittet, (MC) usikkerheden som følge af den begrænsede datamængde i simuleringerne og (sys.) den systematiske usikkerhed.

Acknowledgement

First and foremost, I would like to thank my supervisor, Mogens Dam, for his guidance throughout the entire process. I am grateful for and impressed by all his insightful and detailed comments and all the discussions we have had. He has been a great help whenever it was needed and has always taken his time to explain to me things I did not understand.

I would also like to thank Peter Rosendahl for his help with Pythia and TAUOLA and for all the discussions we have had on tau polarization and spin correlations always resulting in white boards filled with fat arrows and taus.

I am thankful for the useful comments from Zofia Czyczula on my work with the tau helicity re-establishment in Monte Carlo and for introducing me to TauSpinner.

Generally, I would like to thank the entire HEP group at the Niels Bohr Institute for the friendly and nice atmosphere and for the many Friday afternoons spent on Friday beers.

Finally, I would like to thank the young people from the Discovery Centre for always showing up when coffee, cake, beer or pizza was announced. The Discovery Youngster coffee breaks have been a good source of procrastination with discussions on physics and more.

Disclaimer

Some of the plots and tables in this thesis are based on data recorded at the ATLAS experiment during 2011. The plots represent the writer's interpretation of the data and are not officially approved by ATLAS.

Contents

Introduction

Particle physics describes the smallest known particles of the Universe and their interactions. The theory of particle physics, the Standard Model, describes three out of the four fundamental forces excluding the gravitational force. The combination of the electromagnetic and the weak theory into one, the electroweak theory, describes four force carrying particles , $W^{\pm}$, Z^0, and the photon.

Since its discovery in 1983, the properties of the Z boson have been studied in detail at several collider experiments. Observations have shown that the Z boson has an asymmetric behavior, where it favors the fermion to have its spin opposite to its direction of flight, left-handed, over the spin in the direction of flight, right-handed. Hence, the fermions will be polarized. The Z couplings violates the symmetry where the entire Universe is mirrored, parity, and the polarization is a measure of the degree of violation.

The spin orientation can be measured in case of taus. Through the kinematics their decay products, information of the spin orientation of the taus can be derived. Especially the hadronic decay channels of the tau lepton are sensitive to the spin orientation of the taus they originated from.

The latest measurement of the tau polarization from Z decays was performed at the Large Electron-Positron collider (LEP) and published in 2005[1]. The result of the combined measurement of the tau polarization from all four LEP experiments was $P_\tau = -0.1439 \pm 0.0043$[1]. The tau polarization in Z decays has never been measured at a hadron collider.

In 2009, the Large Hadron Collider (LHC) at CERN commenced its data taking. The LHC has exceeded its predecessors in both collision energy and amount of data and is thus the most powerful particle accelerator as of today.

One of the main priorities for the first part of the LHC data taking is the search for the Higgs boson. The Higgs boson is associated with the proposed Higgs mechanism that gives the particles of the Standard Model their mass. The coupling of the Higgs boson depends on the mass of the particles to which it decays. Since the mass of a particle is independent of the spin orientation, the spin of the Higgs boson will be a zero.

Since the Higgs is a scalar, taus originating from it will be unpolarized. It has been discussed whether the tau polarization could be used as an extra separator between Higgs and Z. This thesis contributes to this study by showing that it is possible to measure the tau polarization in Z decays at a hadron collider.

The thesis is divided into four parts, Theory, Experiment, Analysis, and Appendix. Theory consists of Chapters 2-4, Experiment of Chapter 5, and Analysis of Chapters 6-9. Chapter 2 describes the Standard Model of particle physics with emphasis on the electroweak theory and the couplings of the gauge bosons. In Chapter 3, the polarization is introduced and a description of kinematic variables of tau decay products sensitive to the tau polarization is provided. Chapter 4 describes particle collisions at hadron colliders and the event generators used to simulate collisions, particle decays, and detector response in this thesis. Chapter 5 provides a description of the Large Hadron Collider, the sub-detector system of the ATLAS experiment, and how particles are reconstructed and identified with ATLAS. Chapter 6 presents the selection criteria for $Z \to \tau\tau$ events used to study the tau polarization. In Chapter 7, a method for re-establishing tau helicity in Monte Carlo is presented. The effect of the selection and sensitivity loss due to the detector is studied for right-handed and left-handed taus. The measurement of the tau polarization is presented in Chapter 8. The impact of systematic uncertainties on the measured tau polarization are evaluated. Chapter 9 summarizes the study and measurement of the tau polarization.

Part I

Theory

The Standard Model

In this chapter the theory of elementary particle physics, the Standard Model, will be presented. The emphasis will be on the couplings to right-handed and left-handed particles in the electroweak theory.

2.1   Particles of the Standard Model

The Standard Model of particle physics describes the smallest known particles of the Universe, the elementary particles, together with their interactions. The Standard Model was founded in 1960's with the combination of electromagnetism with the weak force. It was expanded in the following two decades to include the Higgs mechanism and the strong force.

There are two types of particles in the Standard Model, the matter particles and the force carrying particles.

Matter Particles

The matter particles of the Standard Model are all fermions (spin-$\frac{1}{2}$ particles). As their name indicate these particles build the matter of the Universe. They can be divided into two groups, the leptons and the quarks. The quarks are never observed individually, but form observable collections named hadrons. The leptons on the other hand are observed in isolation.

Among the leptons is the electron which has an electrical charge of $-1e$, where e is the positive unit charge, and is known for orbiting the atomic nuclei. There exists two other types of leptons like the electron, only heavier, the muon, μ, and the tau lepton, τ. The electron, muon and tau each has a corresponding neutrino, ν. Measurement of the neutrino masses have been consistent with zero and they are therefore assumed to be massless in this thesis[1]. Along with their electric charge the leptons have a weak charge indicating that they are affected by the weak force.

The quarks have weak and electric charge as the leptons, but cannot be observed directly due an additional type of charge, the strong (color) charge. Therefore they are bound together to form hadrons consisting of two or three quarks known as mesons and baryons respectively. The quarks carry a fraction of elementary electrical charge, e. The

---

[1]Observations of neutrino oscillations lead to the conclusion that neutrinos are massive. Until now only upper limits of neutrino masses exist.

Particle Name	Symbol	EM Charge [e]	Weak Charge (Isospin)	Strong Charge (Color)	Mass [MeV]
electron	e	-1	$-1/2$	0	0.511
electron neutrino	ν_e	0	$+1/2$	0	$< 2.2 \cdot 10^{-6}$
muon	μ	-1	$-1/2$	0	106
muon neutrino	ν_μ	0	$+1/2$	0	< 0.170
tau	τ	-1	$-1/2$	0	1777
tau neutrino	ν_τ	0	$+1/2$	0	< 15.5
up	u	$+2/3$	$+1/2$	R/G/B	~ 3
down	d	$-1/3$	$-1/2$	R/G/B	~ 5
charm	c	$+2/3$	$+1/2$	R/G/B	~ 100
strange	s	$-1/3$	$-1/2$	R/G/B	$\sim 1.3 \cdot 10^3$
top	t	$+2/3$	$+1/2$	R/G/B	$173 \cdot 10^3$
bottom	b	$-1/3$	$-1/2$	R/G/B	$\sim 4.2 \cdot 10^3$

Table 2.1: The matter particles of the Standard Model and their charges.[3]

lightest quarks are the *up* and *down* quarks who form the proton (two *up*s and one *down*) and the neutron (two *down*s and one *up*). There exist four other quarks, *charm*, *strange*, *top* and *bottom*.

All of the leptons and quarks have a corresponding anti-particle with opposite electric, weak and color charges. The charges of the fermions are listed in Table 2.1.

The fermions are arranged in three generations consisting of two leptons and two quarks. The number of generations of light neutrinos has been studied at the Large Electron-Positron collider (LEP) and has been measured to be 3.27 ± 0.30[2] consistent with the existence of three generations.

Forces and Interactions

There exist four types of fundamental interactions or forces in Nature. These are gravitation, the electromagnetic force, the weak, and the strong nuclear forces. While the Standard Model describes three of the four fundamental forces it does not even attempt to describe the gravitational, because no quantum mechanical description of gravity has yet been formulated.

In the Standard Model interactions between elementary particles are described by an interchange of force particles between the affected particles. All the force carrying particles are spin-1 bosons and each fundamental force has one or more particles associated with it.

The most well known fundamental force is the electromagnetic force. That is the force that provides electricity, magnetism and light. The force particle of electromagnetism is the light particle, the photon, γ. It is massless and has infinite range. Only particles with electric charge can interact via the electromagnetic force, hence from Table 2.1 we see that all matter particles, except the neutrinos, are affected by electromagnetism.

The weak nuclear force is the force responsible for radioactive β-decays. There are three force particles associated with the weak force, W^+, W^- and Z^0. These particles are all massive and therefore they have a very short range ($\sim 10^{-17}$-10^{-16} m). The weak

Particle Name	Symbol	EM Charge	Weak Charge (Isospin)	Strong Charge (Color)	Mass [MeV]
photon	γ	0	no	no	0
Z-boson	Z^0	0	no	no	$91.188 \cdot 10^3$
W-boson	$W^\pm$	± 1	yes	no	$80.4 \cdot 10^3$
gluon	g	0	no	yes	0
Higgs	H^0	0	yes	no	$> 114.4 \cdot 10^3$

Table 2.2: The force particles and the Higgs boson of the Standard Model and their charges.[3]

force particles couples to weak charge and hence all the matter particles. Furthermore they couple to themselves and the $W^\pm$ couples to the photon.

The last force described by the Standard Model is the strong nuclear force which holds the quarks together in protons and neutrons and furthermore holds the neutrons and protons together to form nuclei. As opposed to the other fundamental forces which decrease in strength as the distance between the particles grows, the strong force is constant for large distances holding the quarks together almost like a rubber band. The boson associated with the strong force is the gluon, g, which is massless and has, as the photon, infinite range. The gluon only couples to particles with color charge and therefore only to quarks and itself.

In Table 2.2 the force particles are listed along with their masses and charges.

Masses of the Particles

In its simplest form the Standard Model treats all the particles as being massless, which is clearly not in agreement with observations. For the particles to acquire mass a new field, the Higgs field, is introduced. Through interactions between the Higgs field and the particles, mass is generated and a new particle is introduced, the Higgs boson.

Despite the large effort put into the search for the Higgs boson it is still undiscovered. In Table 2.2 the Higgs particle is listed with the other bosons of the Standard Model

2.2 Quantum Field Theory

The theoretical framework of the Standard Model is Quantum Field Theory. Quantum field theory is a combination of Einstein's theory of special relativity, quantum mechanics and field theory as for example Maxwell's equations of electromagnetism. Particles are in quantum field theory excitations of the quantum fields.

Local Field Theory

The quantity that describes all the dynamics and kinematics of a classical field is the action, S, defined as

$$S = \int L dt = \int (T - V) dt = \int \mathcal{L}(\phi, \partial_\mu \phi) d^4 x \tag{2.1}$$

with L being the Lagrangian, T the kinematic energy, V the potential energy, and $\mathcal{L}$ the Lagrange density which from now on will be denoted as the Lagrangian. The Lagrangian, $\mathcal{L}$, is a function of one or several fields ϕ and their derivatives $\partial_\mu \phi$. In relativistic quantum field theory the Lagrangian is as well used as the description of the dynamics and kinematics. The individual terms in the Lagrangian are Lorentz-invariant and thus a Lorentz-invariant description of quantum field theory.

According to the principle of least action the action must be minimized in a time interval δt leading to the Euler-Lagrange equations of motion

$$\partial_\mu \left(\frac{\partial \mathcal{L}}{\partial \left(\partial_\mu \phi \right)} \right) - \frac{\partial \mathcal{L}}{\partial \phi} = 0 \tag{2.2}$$

In classical field theory the dynamics of a system will always follow the paths satisfying the classical equations of motion. In quantum field theory, however, the system will follow all paths, also the ones not described by the classical equation of motion. This is known as quantum fluctuations that for example can cause a momentarily creation of two new particles even if there is not a sufficient amount of energy. [4]

Symmetries in Quantum Field Theory

A system is said to be symmetric if it is left "unchanged" for an observer under a given transformation. Symmetries can be split into several categories, local or global, continuous or discrete. A global symmetry is as the name might suggest a symmetry that is independent on location in space time. A local or a gauge symmetry on the other hand depends on the space time coordinates of the system. A continuous symmetry is for example the rotation of a sphere which is symmetric under any angle of rotation whereas a hexagon has discrete symmetries since it can only be rotated a multipla of $60°$.

What holds for all types of symmetries is that for a given symmetry a physical quantity is conserved. This is described by Noether's theorem[5] which states that for a symmetric transformation of the system there exists a current which is conserved. We know this for example from rotation of space time which gives us angular momentum conservation.

The Symmetries of the Standard Model

The Standard Model is build up by many symmetries, both local, global, continuous and discrete symmetries.

A group of symmetries of the Standard Model is the Lorentz-transformations which are symmetries of the flat Minkowski spacetime. The Lorentz covariance states that the system, i.e. the Lagrangian, must be invariant under translation, rotation and boost. The group of symmetries of the Lorentz transformation conserves angular momentum, momentum, and energy. The Lorentz covariance symmetry group is global and continuous.

In the Standard Model three discrete transformations are included, Charge conjugation (change of sign on all charges, $c \rightarrow -c$), Parity inversion (change of sign on all spatial coordinates, $x^i \rightarrow -x^i$), and Time reversal (change of sign on time, $t \rightarrow -t$). These three discrete transformations are not symmetries by themselves, i.e. the Standard Model is not invariant under C, P, or T transformations, nor is it invariant under a combination of two of transformations (CP, PT or CT). However, it is invariant when all three transformations

are performed. It is therefore said that the Standard Model is CPT invariant. As a matter of fact it must be CPT invariant since it is not possible to create an invariant quantum field theory with a hermitian hamiltonian if it is not invariant under CPT transformations[5]. In a CPT transformed universe we will se antiparticles going backwards in time which for us would look like particles moving forward in time.

The last type of symmetries in the Standard Model is Gauge or local symmetries. The gauge symmetries gives rise to the gauge bosons or the force particles of the Standard Model. The Standard Model is invariant under the following gauge transformations, $SU(3) \times SU(2) \times U(1)$. The transformation group $SU(3)$ describes the interaction of the gluon and $SU(2) \times U(1)$ describes the weak and electromagnetic interactions of the Standard Model.

As an example it will be described how the photon is introduced to the Standard Model by imposing local $U(1)$ symmetry on the Lagrangian of a free fermion given by

$$\mathcal{L} = \overline{\psi}(x)\left(i\slashed{\partial} - m\right)\psi(x). \tag{2.3}$$

Here $\overline{\psi}(x)$ is the anti-fermion, $\psi(x)$ the fermion, and $\slashed{\partial}$ is a contraction of $\gamma^\mu \partial_\mu$ where γ^μ refers to the 4×4 Dirac gamma matrices composed of the 2×2 Pauli spin matrices, σ^i as

$$\gamma^0 = \begin{pmatrix} 0 & 1 \\ 1 & 0 \end{pmatrix}, \quad \gamma^i = \begin{pmatrix} 0 & \sigma^i \\ -\sigma^i & 0 \end{pmatrix} \tag{2.4}$$

The $U(1)$ symmetry is simply a rotation of the wave function of the particle, ψ, with the spacetime dependent phase $\alpha(x)$.

$$\psi(x) \to \psi'(x) = e^{-i\alpha(x)}\psi(x) \quad , \quad \overline{\psi}(x) \to \overline{\psi}'(x) = \overline{\psi}(x)e^{i\alpha(x)} \tag{2.5}$$

It is easily seen that the mass term of the Lagrangian, $m\overline{\psi}(x)\psi(x)$, is invariant under the $U(1)$ transformation, i.e. $m\overline{\psi}'(x)\psi'(x) = m\overline{\psi}(x)\psi(x)$. The derivative term is, on the other hand, not invariant under the $U(1)$ transformation and therefore a new derivative must be introduced.

$$D_\mu = \partial_\mu + ieA_\mu(x) \tag{2.6}$$

where $A_\mu(x)$ is a new field called the Gauge Field and must transform as

$$A_\mu(x) \to A'_\mu(x) = A_\mu(x) - \tfrac{1}{e}\partial_\mu\alpha(x) \tag{2.7}$$

In order for $A_\mu(x)$ to propagate a term of $F_{\mu\nu}F^{\mu\nu}$, ($F_{\mu\nu} = \partial_\mu A_\nu - \partial_\nu A_\mu$) is added to the Lagrangian in eq (2.3). This leads to the final Lagrangian

$$\mathcal{L}_{QED} = \overline{\psi}(x)\left(i\slashed{D} - m\right)\psi(x) - \tfrac{1}{4}F_{\mu\nu}F^{\mu\nu} \tag{2.8}$$

As seen in Equation 2.8 there is no $A_\mu A^\mu$ term and therefore no mass term for the $A_\mu(x)$ field hence the particle of the A_μ field will be massless. The interaction term, $F_{\mu\nu}F^{\mu\nu}$, describes the Maxwell equations and the particle of the A_μ field is the photon.[5]

From the assumption that the Lagrangian should be invariant under the local Gauge transformations of $U(1)$ the Lagrangian of Quantum Electric Dynamics has been derived and a new gauge field, $A_\mu(x)$, representing a massless gauge boson, the photon.

2.3   The Electroweak Theory

The Electroweak Theory describes both the the weak force and the electromagnetic force. It is invariant under the gauge group $SU(2)_T \times U(1)_Y$ of weak isospin, T, and weak hypercharge, Y. The hypercharge and the third component of the weak isospin are related to the electrical charge, Q, of a particle through

$$Y \equiv Q - T^3 \tag{2.9}$$

Helicity and Chirality

Experiments show that the $W^\pm$ bosons only decay to left-handed particles. Right-handed and left-handed particles must therefore be treated differently and a clear definition of right-handedness and left-handedness is necessary.

A fermion and its antiparticle is described by a four-component bi-spinor and can be written as two two-component spinors.

$$\psi = \begin{pmatrix} \psi_1 \\ \psi_2 \\ \psi_3 \\ \psi_4 \end{pmatrix} = \begin{pmatrix} \phi \\ \chi \end{pmatrix} \quad , \quad \phi = \begin{pmatrix} \phi_1 \\ \phi_2 \end{pmatrix} \quad , \quad \chi = \begin{pmatrix} \chi_1 \\ \chi_2 \end{pmatrix} \tag{2.10}$$

In quantum mechanics the two two-component spinors correspond to spin +1 and -1. When particles are moving at relativistic velocities the notion of spin-up and spin-down is no longer useful and a new classification of the two-component spinors is needed.[6]

The helicity of a particle is the spin projected onto the momentum of the particle.

$$\lambda = \frac{1}{2} \frac{\vec{\sigma} \cdot \vec{p}}{|\vec{p}|}. \tag{2.11}$$

The helicity operator commutes with the Hamiltonian and helicity is therefore a good quantum number. In fact, no other combination of the Pauli spin matrices will commute with the Hamiltonian, leaving helicity as the only good spin dependent quantum number.[7]

The eigenvalues of the helicity operator are $+\frac{1}{2}$ and $-\frac{1}{2}$. Since the helicity depends on the direction of motion of the particle it is not Lorentz-invariant for massive particles. If one accelerates from a velocity below that of the massive particle to a velocity above the particle, the particle will appear to have flipped its helicity. Helicity can therefore only be used under the assumption that the particles are massless.

Helicity in the ultra-relativistic limit ($m \ll E$) is called chirality. The chiral four-component states are the eigenstates of $\gamma^5 = \gamma^0 \gamma^1 \gamma^2 \gamma^3$ with eigenvalues +1 (right-handed) and -1 (left-handed) with the projections

$$\psi_L = \tfrac{1}{2}(1 - \gamma^5)\psi \qquad , \qquad \psi_R = \tfrac{1}{2}(1 + \gamma^5)\psi \tag{2.12}$$

$$\overline{\psi}_L = \overline{\psi}\tfrac{1}{2}(1 + \gamma^5) \qquad , \qquad \overline{\psi}_R = \overline{\psi}\tfrac{1}{2}(1 - \gamma^5) \tag{2.13}$$

By convention the fermion two-component spinor of a left-handed (right-handed) four-component spinor is also called left-handed (right-handed), whereas the anti-fermion two-component spinor is referred to as right-handed (left-handed).[8] In the following left- and right-handedness refer to two-component spinors.

In the massless limit the chirality states and the helicity states become the same.

The Fermion Fields

The left-handed fermion two-components are arranged in $SU(2)_T$ weak isospin doublets whereas the right-handed are arranged in isospin singlets

$$
\begin{aligned}
l_L &= \begin{pmatrix} \nu_{eL} \\ e_L^- \end{pmatrix}, \begin{pmatrix} \nu_{\mu L} \\ \mu_L^- \end{pmatrix}, \begin{pmatrix} \nu_{\tau L} \\ \tau_L^- \end{pmatrix} \\
q_L &= \begin{pmatrix} u_L \\ d_L' \end{pmatrix}, \begin{pmatrix} c_L \\ s_L' \end{pmatrix}, \begin{pmatrix} t_L \\ b_L \end{pmatrix} \\
l_R &= e_R, \mu_R, \tau_R \\
q_R &= u_R, d_R, c_R, s_R, b_R, t_R
\end{aligned}
\tag{2.14}
$$

For anti-fermions the right-handed two-components are arranged in a $SU(2)_T$ weak isospin doublet and the left-handed in isospin singlets [8]. Since there exists no experimental evidence of right-handed neutrinos and left-handed anti-neutrinos these are not included among the singlets.

The mass eigenstates of the quarks are not the same as the eigenstates of the weak isospin. To obtain the weak isospin eigenstates the lower component of the quark doublets, d, s, and b, is unitary transformed using the Cabibbo-Kobayashi-Maskawa (CKM) mixing matrix

$$
\begin{pmatrix} d' \\ s' \\ b' \end{pmatrix} = \begin{pmatrix} V_{ud} & V_{us} & V_{ub} \\ V_{cd} & V_{cs} & V_{cb} \\ V_{td} & V_{ts} & V_{tb} \end{pmatrix} \begin{pmatrix} d \\ s \\ b \end{pmatrix} \approx \begin{pmatrix} \cos\theta_C & \sin\theta_C & 0 \\ -\sin\theta_C & \cos\theta_C & 0 \\ 0 & 0 & 1 \end{pmatrix} \begin{pmatrix} d \\ s \\ b \end{pmatrix}
\tag{2.15}
$$

In the last part of Equation 2.15 the mixing of (u, d) with the b-quark has been neglected. The value of the Cabibbo angle, θ_C, is $13.1°$.[9]

Gauge Bosons and Interactions of the Electroweak Theory

By requiring $SU(2) \times U(1)$ gauge invariance, four gauge fields are introduced W_μ^1, W_μ^2, W_μ^3, and B_μ. W_μ^a only couples to the isospin triplet current

$$
J_\mu^a = \tfrac{1}{2} \overline{\Psi}_L \gamma_\mu \tau_a \Psi_L, \quad a = 1, 2, 3
\tag{2.16}
$$

where τ_a is the Pauli spin matrices. Ψ_L denote the isospin doublets and $\overline{\Psi}_L$ is the adjoint of Ψ_L ($\overline{\Psi}_L = \Psi_L^\dagger \gamma^0$). The B_μ field couples to the weak hypercharge current

$$
j_\mu^Y = Y \overline{\Psi} \gamma_\mu \Psi
\tag{2.17}
$$

where the chirality of Ψ is not specified since the weak hypercharge current does not depend on chirality [7].

The Lagrangian with the proper covariant derivative of the $SU(2) \times U(1)$ gauge group working on left and right-handed particles is then

$$
\begin{aligned}
\mathcal{L} &= \overline{\psi}_L \gamma^\mu \left(i\partial_\mu - \frac{g}{2}\tau^a W_\mu^a - g' Y_W B_\mu \right) \psi_L \\
&+ \overline{\psi}_R \gamma^\mu \left(i\partial_\mu - g' Y_W B_\mu \right) \psi_R - \tfrac{1}{4} W_{\mu\nu}^a W^{a\mu\nu} - \tfrac{1}{4} B_{\mu\nu} B^{\mu\nu}
\end{aligned}
\tag{2.18}
$$

where $W_{\mu\nu}^a = \partial_\mu W_\nu^a - \partial_\nu W_\mu^a + g\epsilon^{abc} W_\mu^b W_\nu^b$, where ϵ^{abc} is the Levi-Civita symbol, and $B_{\mu\nu} = \partial_\mu B_\nu - \partial_\nu B_\mu$. g and g' are the coupling constants between the weak isospin current and the W and B fields respectively. The bosonic fields, W_μ^a and B_μ, describe the force carrying particles of the electroweak theory, $W^\pm$, Z^0, and γ.

There are no mass terms for the gauge bosons nor the fermions in Equation 2.18 thus they are massless. This contradicts experimental evidence and in order for the gauge bosons to acquire mass without breaking the gauge symmetry an isospin doublet of complex scalar fields, the Higgs field, ϕ, is introduced with Lagrangian term

$$
\mathcal{L} = \left| \left(i\partial_\mu - \frac{g}{2}\tau^a W_\mu^a - g' Y_W B_\mu \right) \phi \right|^2 - V(\phi)
\tag{2.19}
$$

where $V(\phi)$ is the potential given by

$$
V(\phi) = -\mu^2 \phi^\dagger \phi + \frac{\lambda}{2} \left(\phi^\dagger \phi \right)^2 \quad , \quad \mu^2 > 0
\tag{2.20}
$$

By requiring $\mu^2 > 0$, the Higgs field will have a non-zero vacuum expectation value of

$$
v = \sqrt{\frac{\mu^2}{\lambda}}.
\tag{2.21}
$$

The vacuum state of ϕ can be written as[5]

$$
\langle \phi \rangle = \frac{1}{\sqrt{2}} \begin{pmatrix} 0 \\ v \end{pmatrix}
\tag{2.22}
$$

The Higgs field spontaneously breaks the symmetry of the Lagrangian and due to the choice of gauge three massive bosons appears and one boson remains massless. The massive (physical) gauge bosons are a combination of the original gauge bosons, W_μ^a and B_μ

$$
W_\mu^\pm = \frac{1}{\sqrt{2}} \left(W_\mu^1 \mp W_\mu^2 \right) \qquad M_W = \frac{1}{2} v g
\tag{2.23}
$$

$$
Z_\mu = \cos\theta_W W_\mu^3 - \sin\theta_W B_\mu \qquad M_Z = \frac{v}{2}\sqrt{g^2 + g'^2}
\tag{2.24}
$$

$$
A_\mu = \cos\theta_W W_\mu^3 + \sin\theta_W B_\mu \qquad M_A = 0
\tag{2.25}
$$

θ_W is referred to as the weak mixing angle and is given by

$$
\cos\theta_W = \frac{g}{\sqrt{g^2 + g'^2}}, \quad \sin\theta_W = \frac{g'}{\sqrt{g^2 + g'^2}}
\tag{2.26}
$$

The weak mixing angle depends on the masses of the Z and W-bosons:

$$\sin^2 \theta_W = 1 - \left(\frac{M_W}{M_Z}\right)^2 \approx 0.226. \tag{2.27}$$

The masses of the fermions can be acquired by interaction between the Higgs field and the fermionic fields and give rise to a mass of each of the fermions, f, of [5]

$$m_f = \frac{\kappa_f v}{\sqrt{2}} \tag{2.28}$$

The constant κ_f is not constrained through the theory and must be determined experimentally through measurement of the fermion masses.

Now it is easy to define the interaction of the mass eigenstate bosons of the electroweak theory and the covariant derivative can be rewritten to

$$
\begin{aligned}
D_\mu &= \partial_\mu + i \frac{g}{\sqrt{2}} \left(W_\mu^+ T^+ + W_\mu^- T^-\right) \\
&+ i \frac{1}{\sqrt{g^2 + g'^2}} Z_\mu \left(g^2 T^3 - g'^2 Y\right) + i e A_\mu \left(T^3 + Y\right)
\end{aligned}
\tag{2.29}
$$

where $e = g \sin \theta_W = g' \cos \theta_W$ and $T^\pm = \frac{1}{2}(\sigma^1 \pm i\sigma^2)$, T^3, and Y are the operators for isospin and weak hypercharge.

Recalling Equation (2.9) the coupling to Z_μ and A_μ can be rewritten resulting in the interaction terms of the Lagrangian to take the form

$$
\begin{aligned}
\mathcal{L}_I &= \mathcal{L}_I^{EM} + \mathcal{L}_I^{CC} + \mathcal{L}_I^{NC} \\
&= -eQ\overline{\psi}\gamma^\mu \psi A_\mu - \frac{g}{2\sqrt{2}} \overline{\Psi}_L \gamma^\mu \left(T^+ W_\mu^+ + T^- W_\mu^-\right) \Psi_L \\
&\quad - \frac{g}{2\cos\theta_W} \overline{\psi}\gamma^\mu \left(g_V - g_A \gamma^5\right) \psi Z_\mu
\end{aligned}
\tag{2.30}
$$

where g_V and g_A refer to the vector and axial-vector coupling to the fermions:

$$
\begin{aligned}
g_V^f &= T_f^3 - 2Q_F \sin^2\theta_W, \\
g_A^f &= T_f^3.
\end{aligned}
\tag{2.31}
$$

By construction the $W^\pm$ bosons only couple to left-handed particles. This is known as the V-A structure. In the neutral current the vector and axial-vector couplings differ for charged fermions and will therefore give rise to a difference in the amplitudes of vector and axial-vector contributions. The Z will therefore couple to both left-handed and right-handed particles, but with different strength unlike the photon that couples with equal strength to right-handed and left-handed charged fermions.

2.4 Quantum Chromo Dynamics

The last part of the Standard Model is Quantum Chromo Dynamics (QCD) describing the strong force that only affects particles that carry color charge (only quarks and gluons).

The gauge group for QCD is $SU(3)$. There are three color charges for the quarks, Red, Green, and Blue (Anti-Red, Anti-Green, and Anti-Blue for the anti-quarks) and eight different gluons that couple to different color states of the quarks. Since gluons themselves carry color charge, unlike the photon, they can selfinteract.[8]

The Lagrangian for the strong force is

$$\mathcal{L} = \bar{q} \left(i\gamma^\mu D_\mu - m\right) q - \tfrac{1}{4} G^a_{\mu\nu} G^{\mu\nu a} \tag{2.32}$$

where $D_\mu = \partial_\mu + ig_\mathrm{s} T_a G^a_\mu$ is the covariant derivative, G^a_μ is the gluon field, T_a is the generator of the gauge group, and $G^a_{\mu\nu} = \partial_\mu G^a_\nu - \partial_\nu G^a_\mu - g_\mathrm{s} f_{abc} G^b_\mu G^c_\mu$ describes the gluon propagation. g_s is the coupling of QCD, and f_{abc} is the structure constant of the gauge group ($[T_a, T_b] = i f_{abc} T_c$). [7]

The coupling of the strong force differs from the coupling of the electroweak force by the fact that it is constant at large distances whereas the electroweak coupling decreases with growing distance. At short distances the strong and electroweak coupling show the same behavior. When two quarks are close together the coupling constant is small there is thus no gluon field between them and they can move freely (asymptotic freedom). If the quarks moving apart, they will be pulled together again due to field lines of the strong force connecting them (color confinement). If the force pulling the quarks apart is sufficiently strong a quark-anti-quark pair will be created from the vacuum and what was once one hadron has now split into two. Due to this effect quarks are glued together to form colorless objects known as hadrons.

Tau Polarization in Z Decays and its Measurement

In this chapter the polarization asymmetry in Z^0 decays will be presented along with the basic properties of tau decays and how to use tau decays as spin analyzers.

3.1 The Z Boson

In hadron collisions, Z bosons are produced in quark-antiquark annihilations as shown in Figure 3.1. The antiquarks are present in the proton through quantum fluctuations creating a sea of quarks and antiquarks. Quark pairs can also create off-shell, virtual photons, γ^* causing interference between contributions from γ^* and contributions from Z.
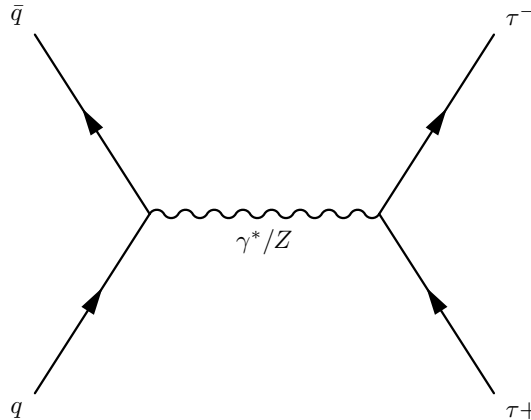
Figure 3.1: Feynman diagram for the leading order $q\bar{q} \rightarrow Z \rightarrow \tau\tau$ process.

As seen in Figure 3.2, the Z peak at ~ 90 GeV lies on top of the smoothly decreasing γ^* distribution. At hadron colliders the energy of the quarks colliding varies between the events depending on the energy carried by the quarks and antiquarks. A range of energies will therefore be studied at the Large Hadron Collider and it is not possible to study the physics exactly at or near the Z peak in $Z \rightarrow \tau\tau$ decays where undetectable neutrinos are present in the decays of the tau leptons.

15
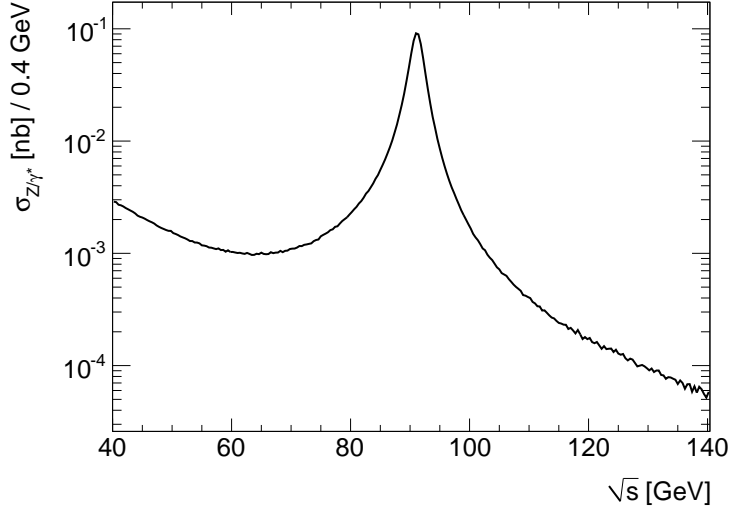
Figure 3.2: The number of produced Z/γ^* in proton collisions as a function of the center of mass energy. The distribution is made from simulations.

The width of the Z boson is given by

$$\Gamma_Z = \sum_f N_c^f \frac{G_F M_Z^3}{6\pi\sqrt{2}} \left[g_A^{f\,2} + g_V^{f\,2} \right] \tag{3.1}$$

where f denotes the fermion flavour, N_c^f is the number of color charges, G_F the Fermi coupling constant ($G_F = 1.16637(1) \times 10^{-5}$ GeV^{-2} [3]), M_Z the mass of the Z, and g_V^f (g_A^f) is the vector (axial-vector) coupling between the fermion and the boson Z. The width of the Z is inversely proportional to its lifetime.

The cross section for $q\bar{q} \to Z/\gamma^* \to ff$ is given by [7]

$$
\begin{aligned}
\sigma(s) =& \quad \sigma^\gamma(s) + \sigma^{Z\gamma}(s) + \sigma^Z(s) \\
=& \frac{1}{3} N_c^f \frac{4\pi\alpha(s)^2}{3s} \left[Q_q^2 Q_f^2 + 2 Q_q Q_f \mathrm{Re}(r(s)) g_V^f g_V^q + |r(s)|^2 \left(g_V^{f\,2} + g_A^{f\,2} \right) \left(g_V^{q\,2} + g_A^{q\,2} \right) \right]
\end{aligned}
\tag{3.2}
$$

where $\alpha(s)$ is the electroweak coupling constant dependent on the center of mass energy squared, s. $r(s)$ is a propagator given by

$$r = \frac{G_F M_Z^2}{2\pi\sqrt{2}\alpha(s)} \cdot \frac{s}{s - M_Z^2 + iM_Z\Gamma_Z} \tag{3.3}$$

In Equation 3.2, σ^Z is the Z cross section, $\sigma^{Z\gamma}$ is the interference term between Z and γ^*, and σ^γ is the γ^* cross section. The Z/γ^* cross section is dominated by the Z cross section near the Z peak at $\sqrt{s} = M_Z$.

3.2 Polarization

As described in Section 2.3, the Z^0 couples differently to right-handed and left-handed fermions. When a fermion-anti-fermion pair annihilate to create a Z^0 (or a photon) the fermion and the anti-fermion must have opposite helicities due to conservation of angular momentum. The fermion-anti-fermion pair created when the Z^0 or photon decays must similarly have opposite helicities. In Figure 3.3 the helicity combinations for the $q\bar{q} \to Z/\gamma^* \to \tau^-\tau^+$ process are shown.
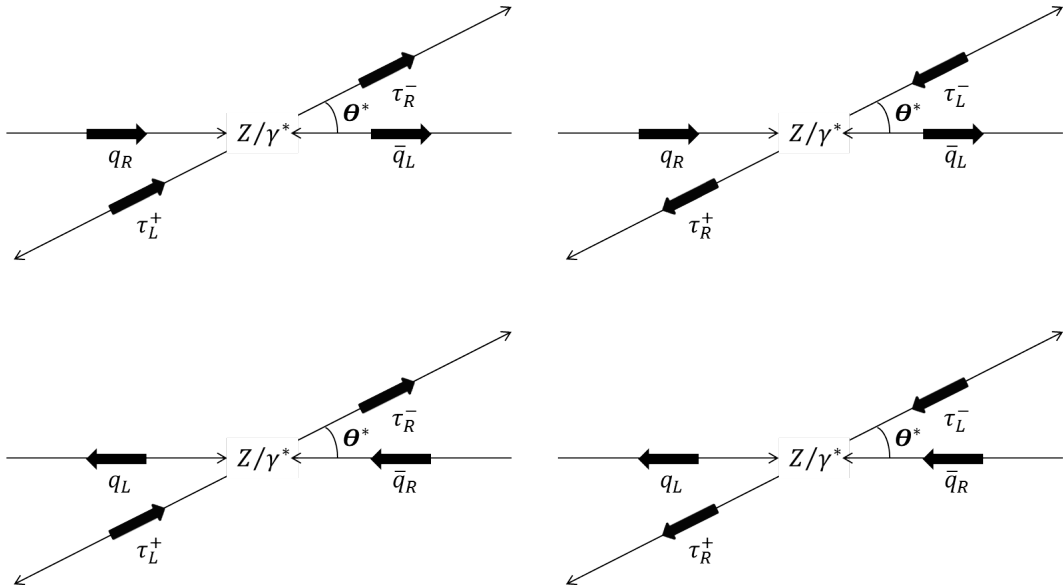
Figure 3.3: Helicity combination in $q\bar{q} \to Z/\gamma^* \to \tau^-\tau^+$. The thick arrows denote the helicity of the quarks and taus.

The derivations in this section follow the argumentation in Ref. [10].

The cross section for $q\bar{q} \to Z/\gamma^* \to \tau^-\tau^+$ depends on θ^* which is the angle between the initial state quark and the final state fermion in rest frame of the Z. The cross sections for the helicity combinations shown in Figure 3.3 are

$$\frac{\mathrm{d}\sigma}{\mathrm{d}\cos\theta^*}\left(q_L\bar{q}_R \to \tau_L^-\tau_R^+\right) = \frac{1}{3}\frac{4\pi\alpha\left(s\right)^2}{s} \times$$

$$\left[Q_q^2 Q_\tau^2 + 2\mathrm{Re}\chi\left(s\right)Q_q Q_\tau \bar{g}_L^q \bar{g}_L^\tau + \left|\chi\left(s\right)\right|^2 \bar{g}_L^{q\,2}\bar{g}_L^{\tau\,2}\right]\left(1+\cos\theta^*\right)^2$$

$$\frac{\mathrm{d}\sigma}{\mathrm{d}\cos\theta^*}\left(q_L\bar{q}_R \to \tau_R^-\tau_L^+\right) = \frac{1}{3}\frac{4\pi\alpha\left(s\right)^2}{s} \times$$

$$\left[Q_q^2 Q_\tau^2 + 2\mathrm{Re}\chi\left(s\right)Q_q Q_\tau \bar{g}_L^q \bar{g}_R^\tau + \left|\chi\left(s\right)\right|^2 \bar{g}_L^{q\,2}\bar{g}_R^{\tau\,2}\right]\left(1-\cos\theta^*\right)^2$$

$$\frac{\mathrm{d}\sigma}{\mathrm{d}\cos\theta^*}\left(q_R\bar{q}_L \to \tau_L^-\tau_R^+\right) = \frac{1}{3}\frac{4\pi\alpha\left(s\right)^2}{s} \times$$

$$\left[Q_q^2 Q_\tau^2 + 2\mathrm{Re}\chi\left(s\right)Q_q Q_\tau \bar{g}_R^q \bar{g}_L^\tau + \left|\chi\left(s\right)\right|^2 \bar{g}_R^{q\,2}\bar{g}_L^{\tau\,2}\right]\left(1-\cos\theta^*\right)^2$$

$$\frac{\mathrm{d}\sigma}{\mathrm{d}\cos\theta^*}\left(q_R\bar{q}_L \to \tau_R^-\tau_L^+\right) = \frac{1}{3}\frac{4\pi\alpha\left(s\right)^2}{s} \times$$

$$\left[Q_q^2 Q_\tau^2 + 2\mathrm{Re}\chi\left(s\right)Q_q Q_\tau \bar{g}_R^q \bar{g}_R^\tau + \left|\chi\left(s\right)\right|^2 \bar{g}_R^{q\,2}\bar{g}_R^{\tau\,2}\right]\left(1+\cos\theta^*\right)^2$$

$$(3.4)$$

where $\chi\left(s\right)$ is a propagator given as

$$\chi\left(s\right) = \frac{G_F M_Z^2}{2\pi\sqrt{2}\alpha\left(s\right)} \cdot \frac{s}{s - M_Z^2 + is\Gamma_Z/M_Z} \tag{3.5}$$

By comparing the $r(s)$ propagator of Equation 3.3 with $\chi(s)$ it is seen that the only difference is in the denominator. This is due to an s dependence of Γ_Z ($\Gamma_Z(s) = \frac{s}{M_Z^2}\Gamma(M_Z^2)$). Γ_Z denotes the width at the Z peak, $\sqrt{s} = M_Z$.

In Equation 3.4 the correction due to interference between Z^0 and photons is taken into account. $\bar{g}_L^f$ and $\bar{g}_R^f$ are the effective[1] chiral couplings in the neutral current for a fermion with flavour f. They can be expressed in terms os the vector and axial vector couplings, $\bar{g}_V^f$ and $\bar{g}_A^f$, as

$$\bar{g}_L^f = \frac{\bar{g}_V^f + \bar{g}_A^f}{2}$$

$$\bar{g}_R^f = \frac{\bar{g}_V^f - \bar{g}_A^f}{2} \tag{3.6}$$

The first term in the parenthesis in Equation 3.4 is the pure Z contribution, the second term is the interference term between Z and γ^*, and the last term is the pure γ^* contribution.

With unpolarized beams the differential cross section can be expressed as

$$\frac{\mathrm{d}\sigma_\tau}{\mathrm{d}\cos\theta^*}\left(s, \cos\theta^*; \lambda\right) = \left(1+\cos^2\theta^*\right)F_0^\tau\left(s\right) + 2\cos\theta^* F_1^\tau\left(s\right)$$

$$-\lambda\left[\left(1+\cos^2\theta^*\right)F_2^\tau\left(s\right) + 2\cos\theta^* F_3^\tau\left(s\right)\right] \tag{3.7}$$

---

[1]The effective couplings take into account the electroweak radiative corrections in the $q\bar{q} \to Z/\gamma^* \to \tau^-\tau^+$ process

with λ being the helicity of τ^-. The four form factors are given as

$$
\begin{aligned}
F_0^\tau(s) &= \frac{1}{3}\frac{\pi\alpha(s)^2}{2s}\left[Q_q^2 Q_\tau^2 + 2\mathrm{Re}\chi(s)\,Q_q Q_\tau \bar{g}_V^q \bar{g}_V^\tau + |\chi(s)|^2\left(\bar{g}_V^{q\,2}+\bar{g}_A^{q\,2}\right)\left(\bar{g}_V^{\tau\,2}+\bar{g}_A^{\tau\,2}\right)\right] \\
F_1^\tau(s) &= \frac{1}{3}\frac{\pi\alpha(s)^2}{2s}\left[\qquad\quad 2\mathrm{Re}\chi(s)\,Q_q Q_\tau \bar{g}_A^q \bar{g}_A^\tau + |\chi(s)|^2 2\bar{g}_V^q \bar{g}_A^q 2\bar{g}_V^\tau \bar{g}_A^\tau\right] \\
F_2^\tau(s) &= \frac{1}{3}\frac{\pi\alpha(s)^2}{2s}\left[\qquad\quad 2\mathrm{Re}\chi(s)\,Q_q Q_\tau \bar{g}_V^q \bar{g}_A^\tau + |\chi(s)|^2\left(\bar{g}_V^{q\,2}+\bar{g}_A^{q\,2}\right) 2\bar{g}_V^\tau \bar{g}_A^\tau\right] \\
F_3^\tau(s) &= \frac{1}{3}\frac{\pi\alpha(s)^2}{2s}\left[\qquad\quad 2\mathrm{Re}\chi(s)\,Q_q Q_\tau \bar{g}_A^q \bar{g}_V^\tau + |\chi(s)|^2 2\bar{g}_V^q \bar{g}_A^q\left(\bar{g}_V^{\tau\,2}+\bar{g}_A^{\tau\,2}\right)\right]
\end{aligned}
\tag{3.8}
$$

The longitudinal polarization asymmetry of τ^- is the asymmetry between the number of right-handed and left-handed τ^- (N_R and N_L respectively), i.e.

$$
P_\tau = \frac{N_R - N_L}{N_R + N_L} = \frac{\sigma_\tau(\lambda=1)-\sigma_\tau(\lambda=-1)}{\sigma_\tau(\lambda=1)+\sigma_\tau(\lambda=-1)}
\tag{3.9}
$$

Equation 3.9 is valid in the ultra-relativistic limit ($m_\tau \ll E_\tau$), which is appropriate for taus from Z-decays. In this limit, the tau helicity and chirality states are identical. The polarization , P_τ, is defined for τ^- and will have the opposite sign for τ^+. In terms of the form factors in Equation 3.8 the longitudinal polarization can be rewritten to

$$
P_\tau = -\frac{\left(1+\cos^2\theta^*\right)F_2^\tau(s)+2\cos\theta^* F_3^\tau(s)}{\left(1+\cos^2\theta^*\right)F_0^\tau(s)+2\cos\theta^* F_1^\tau(s)}
\tag{3.10}
$$

At the Z^0 pole ($\sqrt{s}\approx M_Z$) the polarization integrated over $\cos\theta^*$ becomes

$$
\langle P_\tau\rangle = -\frac{2\bar{g}_V^\tau \bar{g}_A^\tau}{\bar{g}_V^{\tau\,2}+\bar{g}_A^{\tau\,2}} = -\mathcal{A}_\tau
\tag{3.11}
$$

Here the last equation defines the so-called chiral coupling asymmetry, $\mathcal{A}$. Values of g_A, g_V, and $\mathcal{A}$ for different fermions are given in Table 3.1.

Recalling Equation 2.31 and observing that $\bar{g}_A^\tau \gg \bar{g}_V^\tau$ (see Table 3.1), the expression for polarization asymmetry reduces to

$$
\langle P_\tau\rangle \approx -2\frac{\bar{g}_A^\tau}{\bar{g}_V^\tau} = -2\left(1-4\sin_{eff}^2\theta_W\right)
\tag{3.12}
$$

In this limit the dependence on the weak mixing angle is particularly simple. The polarization asymmetry is thereby a measure of the effective weak mixing angle, θ_W.

3.3 Tau Decays

The tau lepton was discovered in 1975 and since its discovery measurements have shown that the tau lepton behaves as the electron and the muon and is thus consistent with a third family lepton.

The tau lepton is the heaviest of the leptons with a mass of 1.777 GeV and therefore it has a very short lifetime ($\tau_\tau = (290.6\pm1.0)\times10^{-15}$ s [3]). Due to its large mass the tau

f	T_3^f	Q_f	g_A^f	g_V^f	$\mathcal{A}_f$
ν_τ	1/2	0	1/2	1/2	1
τ^-	-1/2	-1	-1/2	-0.04	0.16
u	1/2	2/3	1/2	0.19	0.67
d	-1/2	-1/3	-1/2	-0.35	0.94

Table 3.1: Numeric values of quantum numbers, vector and axial vector couplings, and the chiral coupling asymmetry, $\mathcal{A}_f$. A value of $\sin^2 \theta_W = 0.23$ has been used.

Decay Modes	Branching fraction [%]
$e^- \bar{\nu}_e \nu_\tau$	17.82 ± 0.04
$\mu^- \bar{\nu}_\mu \nu_\tau$	17.39 ± 0.04
$\pi^- \nu_\tau$	10.91 ± 0.07
$K^- \nu_\tau$	0.696 ± 0.023
$\rho^- \nu_\tau$	25.94 ± 0.09
$K^{*-} \nu_\tau$	0.429 ± 0.015
$h^- 2\pi^0 \nu_\tau$	10.85 ± 0.11
$h^- \geq 3\pi^0 \nu_\tau$	1.34 ± 0.07
$h^- h^+ h^- \nu_\tau$	9.80 ± 0.07
$h^- h^+ h^- \geq 1\pi^0 \nu_\tau$	5.38 ± 0.07

Table 3.2: Branching fraction of the most common tau decays [3]. $h^\pm$ stands for $\pi^\pm$ or $K^\pm$.

lepton is sufficiently heavy to decay to an up and a Cabibbo mixed down quark, unlike the electron and the muon. Thus, the tau lepton has two different decay modes, it can decay leptonically or hadronically.
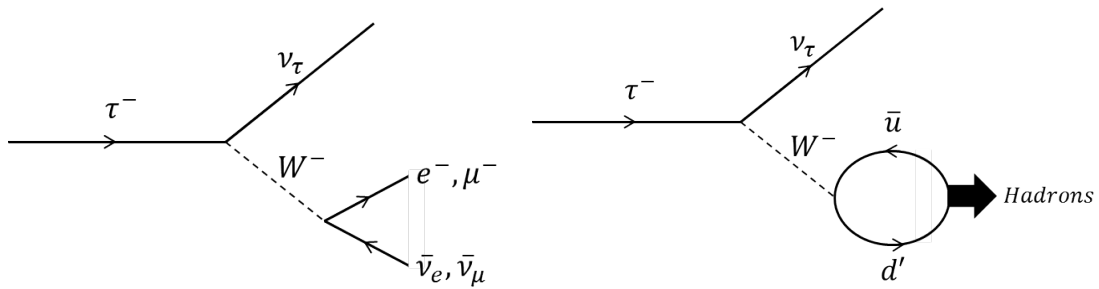
Figure 3.4: Leptonic and hadronic decay of the tau lepton.

In Figure 3.4 the two decay modes of the tau lepton are illustrated. To first order one expects the branching fraction to hadrons to be three times as big as the branching fraction to electrons and muons due to the color charges of the quarks.

In Table 3.2 branching fractions for both hadronic and leptonic decays are stated. The leptonic decays have a total branching fraction of $\sim 35\%$ and the hadronic decays have a

Meson	Quark Composition	Mass [MeV]	Dominating Decay Mode
π^-	$\bar{u}d$	139.6	-
ρ^-	$\bar{u}d$	775.5	$\pi^-\pi^0$
a_1^-	$\bar{u}d$	1230	$\rho^-\pi^-$
K^-	$\bar{u}s$	493.7	-
K^{*-}	$\bar{u}s$	891.6	$K^-\pi^0$
K_1^-	$\bar{u}s$	1403	$K^{*-}\pi^0$

Table 3.3: Mass, quark composition and dominating decay mode of the mesons from the main hadronically tau decays.[3]

total branching fraction of $\sim 65\%$. This is consistent with the expected branching fraction when QCD corrections are included.

The tau lepton can decay to mesons being pseudo-scalars, vector or axial-vector particles that are either Cabibbo-favoured $\left(\pi^-, \rho^-, a_1^-\right)$ or Cabibbo-suppressed $\left(K^-, K^{*\,-}, K_1^-\right)$. In Table 3.3 the mass, quark composition, and dominating decay mode for both the Cabibbo-favoured and Cabibbo-suppressed mesons are listed.

3.4 Tau Decays as Spin Analyzers

It was already predicted in 1971, four years before the discovery of the tau lepton, by Tsai [11] that if a lepton heavy enough to decay to quarks existed the helicity of the lepton would be accessible through the angular distribution of the decay products due to the maximal parity violation in the decay of the heavy leptons. Tau leptons can thus be used as spin analyzers.

In the following sections, differential distributions are derived for τ^- decays. The corresponding distributions for τ^+ decays can be found by a change of sign on the helicity dependent term. Since $P_{\tau-}$ has the opposite sign of $P_{\tau+}$, the distributions for a left-handed τ^- is the same as for a right-handed τ^+. There is therefore no need to split the analysis into τ^- and τ^+. For a given polarization, the kinematic distributions of the decay products of τ^+ and τ^- will be identical.

Hadronic Decays as Spin Analyzers

In the case of a tau decaying to a pion and a neutrino, the neutrino is preferably emitted opposite the spin orientation of the tau to conserve angular momentum. This is due to the left-handed nature of the neutrino. Hence, the pion will preferably be emitted in the direction of the spin orientation of the tau. The angle θ is defined to be the angle in the rest frame of the tau lepton between the direction of flight of the tau in the laboratory rest frame and the direction of flight of the pion, as illustrated in Figure 3.5. The decay distribution as a function of θ is be given as [12]

$$\frac{1}{\Gamma}\frac{\mathrm{d}\Gamma}{\mathrm{d}\cos\theta} = \tfrac{1}{2}\left(1 + P_\tau \cos\theta\right) \tag{3.13}$$

where P_τ is the average polarization of the sample. In the case of a sample consisting completely of right-handed taus P_τ equals to 1 and in the case of a sample of left-handed taus P_τ equals to -1.
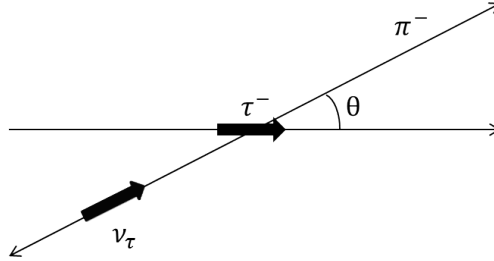

Figure 3.5: $\tau^- \to \pi^- \nu_\tau$. The thick arrows denote the helicity of the particles.

The angle θ is given by the kinematics of the decay in the following form

$$\cos\theta = \frac{2x - 1 - a^2}{\beta(1 - a^2)} \tag{3.14}$$

where $\beta = \sqrt{1 - m_\tau^2/E_{\tau^2}}$ is the velocity of the tau, x is the fraction of the energy of the tau carried away by the pion ($x = E_\pi/E_\tau$), and $a = m_\pi/m_\tau$. In the case of the pion decay, terms of order a^2 can be ignored. The velocity of the tau, β, can be put to one since the $E_\tau \gg m_\tau$ in the case of Z decays.

The differential distribution in Equation 3.13 can be rewritten in terms of x_π to

$$\frac{1}{\Gamma}\frac{d\Gamma}{dx} = 1 + P_\tau(2x - 1) \tag{3.15}$$

From this it is clear that a right-handed τ^- (left-handed τ^+) will preferably decay into a hard pion, whereas a left-handed τ^- (right-handed τ^+) will decay into a soft pion. The polarization of an ensemble of taus can be measured by measuring the slope of the distribution of x.

When a tau decays into a vector meson, V, and a tau neutrino, there are two possible helicity configurations of the vector meson. As shown in Figure 3.6 the vector meson can either be longitudinally polarized (helicity equals 0) or transversely polarized (helicity equals -1). In case of a longitudinally polarized vector meson, the differential distribution is similar to that of the pion decay with the only difference being $x = E_V/E_\tau$ and the terms of order a^2 can no longer be neglected. When a tau decays to a transversely polarized vector meson, the sign of the spin of the final state is flipped. Since there will be a mixture of longitudinally and transversely polarized vector mesons the differential distribution becomes

$$\frac{1}{\Gamma}\frac{d\Gamma}{d\cos\theta} = \tfrac{1}{2}(1 + \alpha P_\tau \cos\theta) \tag{3.16}$$
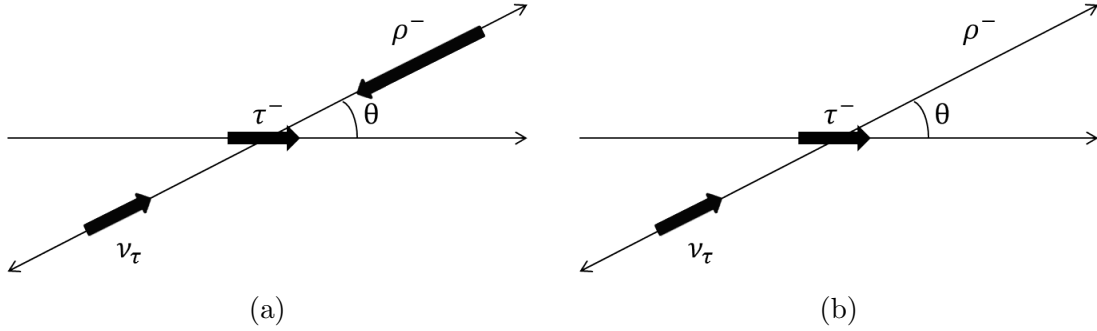
Figure 3.6: $\tau^- \to \rho_T^- \nu_\tau$ (a) and $\tau^- \to \rho_L^- \nu_\tau$(b). The thick arrows denote the helicity of the particles.

where α is given by

$$\alpha = \frac{m_\tau^2 - 2m_V^2}{m_\tau^2 + 2m_V^2} \tag{3.17}$$

For rho decays α has the value of 0.46 and for a_1 decays a value of 0.12. The differential distribution can be rewritten in terms of the energy fraction carried by the vector meson, x, to

$$\frac{1}{\Gamma}\frac{d\Gamma}{dx} = \frac{1}{1 - a^2}\left(1 + \alpha P_\tau \frac{2x - 1 - a^2}{1 - a^2}\right) \tag{3.18}$$

As seen in Figure 3.7(b) the distribution of energy fraction carried by the rho meson will run from $a^2 = (m_\rho/m_\tau)^2$ to one.
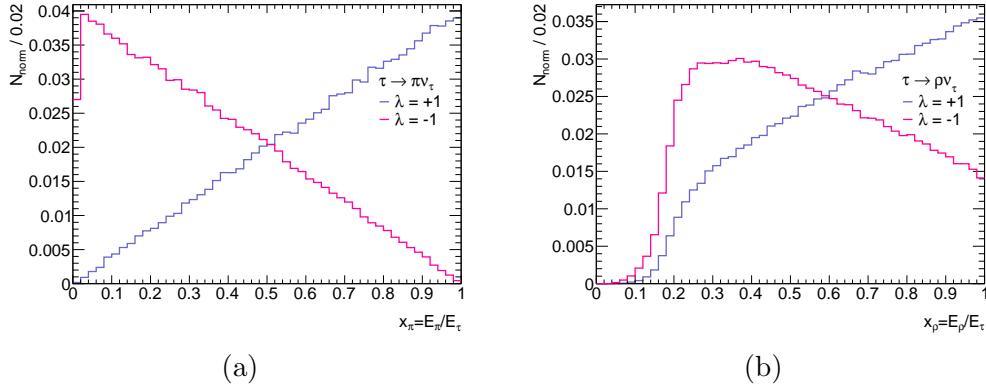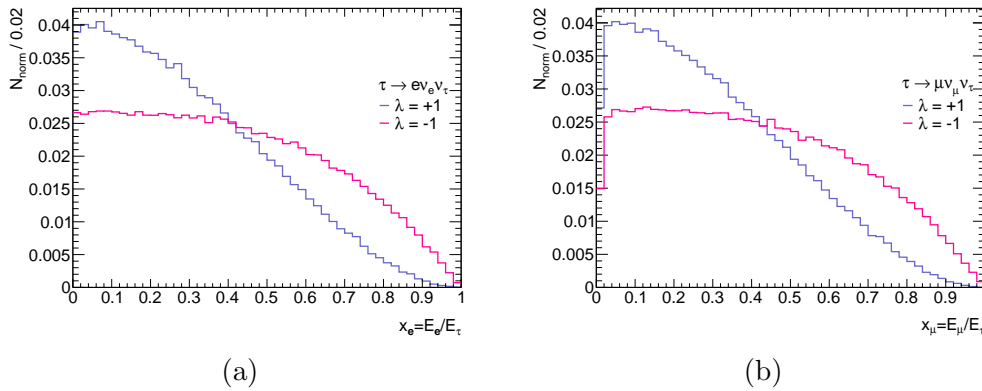

Figure 3.7: Distribution of fraction of visible energy, x, in pion (a) and rho (b) decays divided into left-handed (pink) and right-handed (blue) samples.

A lot of sensitivity of the polarization is lost in Equation 3.18 compared to the pion decay due to the mixing of longitudinally and transversely polarized vector states. Some of the sensitivity can be regained by considering other variables sensitive to the tau helicity.
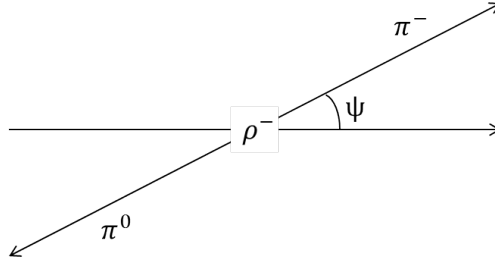
Figure 3.8: $\rho^- \to \pi^- \pi^0$.

For decays into a rho-meson another variable sensitive to tau helicity is the angle between the direction of flight of the vector meson and the π^- in the rest frame of the vector meson as illustrated in Figure 3.8. The angle is given by [13]

$$\cos \psi = \frac{m_\rho}{\sqrt{m_\rho^2 - 4m_\pi^2}} \cdot \frac{E_{\pi^-} - E_{\pi^0}}{|\vec{p}_{\pi^-} + \vec{p}_{\pi^0}|} \qquad (3.19)$$

The angle is sensitive to the helicity of the rho meson and therefore also to the helicity of the tau, that the vector meson originated from. This is due to the fact that right-handed τ^- produce more longitudinally polarized rhos whereas left-handed τ^- produce more transversely polarized rhos. When a longitudinally polarized rho decays the decay angle, ψ, will preferably be $0°$ or $180°$. In a transversely polarized rho decay the decay angle, ψ, will preferably be $90°$ due to conservation of angular momentum. From Equation 3.19 it is seen that the angle depend on the energy sharing between the charged and the neutral pion. Hence in a decay of a transversely polarized rho the energy tends to be shared equally between the charged and the neutral pion. On the contrary, when a longitudinally polarized rho decays one of the pions will tend carry most of the available energy.

The distributions of $\cos \psi$ for right-handed and left-handed taus from rho decays are shown in Figure 3.9.
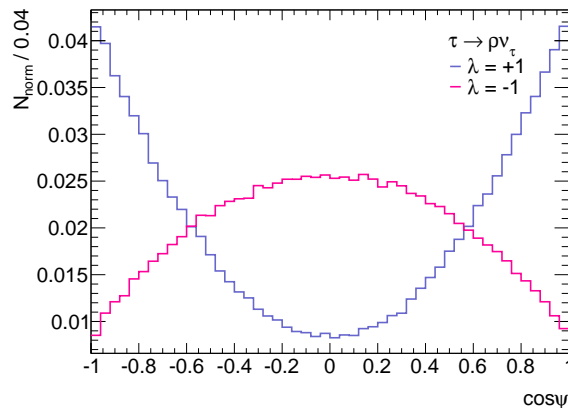
Figure 3.9: The distribution of $\cos \psi$ from rho decays divided into left-handed (pink) and right-handed (blue) samples. Each sample is normalized to one.

In the decay of heavier vector mesons such as a_1 there will be three pions. This gives rise to six kinematic variables used to extract the tau helicity. [13]

Leptonic Decays as Polarization Analyzers

When a tau lepton decays leptonically there will be two neutrinos in the final state which makes this decay channel less sensitive to the tau helicity than the hadronic channels. Since we do not have access to the helicity of the final state lepton, the differential distribution is averaged over both helicities of the lepton. Ignoring terms containing m_ℓ/m_τ the differential distribution can be written as [12]

$$\frac{1}{\Gamma}\frac{d\Gamma}{dx} = \tfrac{1}{3}(1-x)\left(\left(5+5x-4x^2\right)+P_\tau\left(1+x-8x^2\right)\right) \tag{3.20}$$

where $x = E_\ell/E_\tau$.

Figure 3.10: Distribution of fraction of visible energy, x, in electron (a) and muon (b) decays divided into left-handed (pink) and right-handed (blue) samples.

In Figure 3.10 it is seen that the distributions of the visible energy fraction, x, looks similar for left-handed and right-handed taus. The dip at $x_\mu = 0$ in Figure 3.10(b) which is not present in Figure 3.10(a) is due to the larger mass of the muon compared to the mass of the electron since x will be within the range from $\left(m_\ell/m_\tau\right)^2$ to one.

Sensitivity

To quantify how suited different tau decays are as polarization analyzers the concept of sensitivity is introduced. For every decay channel the n kinematic variables usable for polarization measurements are arranged in a vector, $\vec{\xi}$. The decay distribution can then be written as [14]

$$W(\vec{\xi}) = f(\vec{\xi}) + P_\tau g(\vec{\xi}) \tag{3.21}$$

Decay Mode	Sensitivity S	Branching Fraction $\mathcal{B}$	Relative Weight $\propto S^2\mathcal{B}$
$e^-\bar{\nu}_e\nu_\tau$	0.22	0.1782	0.06
$\mu^-\bar{\nu}_\mu\nu_\tau$	0.22	0.1739	0.06
$\pi^-\nu_\tau$	0.58	0.1091	0.30
$\rho^-\nu_\tau$	0.49	0.2594	0.44
$\pi^-\pi^+\pi^-\nu_\tau$	0.45	0.0980	0.13

Table 3.4: Sensitivity, branching fraction, and relative weight for the tau decays most frequently used for polarization measurements. An input of $P_\tau = -0.15$ has been used. The relative weights are normalized to add up to unity. In case of the vector meson decay modes all the variables sensitive to the tau polarization have been used.[10][13]

where f and g fulfills

$$\int f(\vec{\xi})\,\mathrm{d}^n\vec{\xi} = 1, \quad \int g(\vec{\xi})\,\mathrm{d}^n\vec{\xi} = 0, \quad f \geq 0 \text{ and } |g| \leq f \tag{3.22}$$

where f is the sum of the distributions coming from a right-handed and a left-handed sample of taus while g is the difference. The sensitivity is then defined as [14]

$$S^2 = \int \frac{g^2}{f + P_\tau g} d^n\vec{\xi} \tag{3.23}$$

The sensitivity of different decay channels is listed in Table 3.4. The weight of the decay channels in an ideal polarization measurement is the sensitivity squared times the branching fraction. It is clear from Table 3.4 that the lepton channels have a very low weight while the rho decay has the highest among the hadronic channels. The low sensitivities of the lepton channels are due to the two undetectable neutrinos in the final state.

3.5   Polarization Observables at Hadron Colliders

In Section 3.4 it was shown that especially the pion and rho channel are sensitive to the spin orientation of the tau. When using x to measure the polarization of the taus knowledge of the energy of the tau is required. At electron-positron colliders the tau energy is known since the exact collision energy is known through the beam constraint and the tau polarization can be measured with x. At hadron colliders the energy of a collision is in general not known, since it is the gluons and quarks inside the hadrons that collide and the tau energy is therefore not known through a beam constraint. It is only known that the energy in the transverse plane to the beam is equal to zero before the collision. The tau energy would be known if the momentum of the tau neutrinos were reconstructed. The sum of the momentum of the tau neutrinos in the transverse plane can be reconstructed through the transverse energy. In the collinear approximation [15] the tau neutrino energy is reconstructed by projecting the missing transverse energy onto the tau directions. The collinear approximation requires that the tau pair must not be back-to-back, which will cut away a lot of the signal.

Instead of using the x distributions the $\cos\psi$ (Equation 3.19) distribution of the rho decay can be used. However, the width of the rho mass is large and the mass not measured well at the Large Hadron Collider. At the expense of sensitivity, the first part of Equation 3.19 is dropped, and the charged energy asymmetry is used instead [16]

$$\Upsilon = \frac{E_{ch} - E_{\pi^0}}{E_{ch} + E_{\pi^0}} \tag{3.24}$$

where E_{ch} is the energy of the charged mesons and E_{π^0} is the neutral energy of the π^0s. The charged energy asymmetry do not require knowledge of the tau energy. The charged energy asymmetry is optimized for the rho decay, but in this thesis it is studied inclusively for all decays with one charged meson in the final state.

In Figure 3.11 the charged energy asymmetry is shown for right-handed and left-handed taus. The difference between the charged energy asymmetry in Figure 3.11 and the $\cos\psi$ distribution in Figure 3.9 is that the charged energy symmetry is zero at $\Upsilon = \pm 1$ for both right-handed and left-handed taus. This causes the sensitivity of the charged energy asymmetry to be lower than the sensitivity of $\cos\psi$.
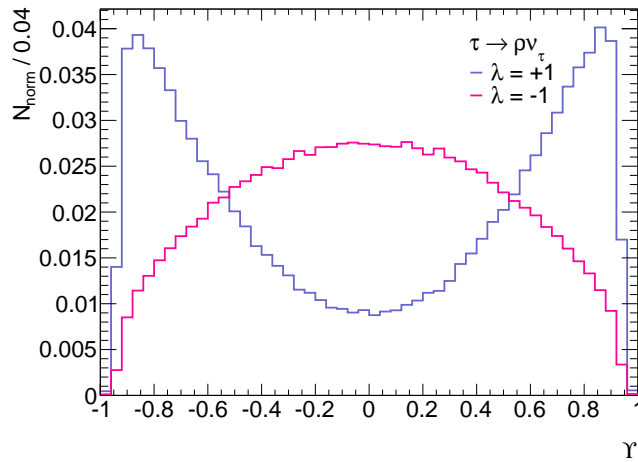
Figure 3.11: The distribution of the charged energy asymmetry, Υ, from rho decays divided into left-handed (pink) and right-handed (blue) samples. Each sample is normalized to one.

Particle Physics at Hadron Colliders

In this chapter, an overview of the structure of collisions at hadron colliders will be given together with a description of Monte Carlo techniques and the event generators used in this thesis.

4.1 Collisions at Hadron Colliders

At the Large Hadron Collider (LHC) protons are collided to study the physics of the elementary particles. At the elementary level, it is, however, not the protons that are colliding, but rather the constituents of the protons, the gluons and the quarks. The protons consists of three valence quarks, two up quarks and one down quark, and a sea of quark-anti-quark pairs held together by gluons. Most often the protons will collide in soft collisions. We are interested in a hard collision that happens rarely.

In Figure 4.1 a schematic view of a proton-proton collision is seen. Here follows a short summary of the different parts of a proton-proton collision:

Hard Process: When partons collide at high energy different processes can occur. One process if the scattering of two partons creating two high p_T partons. This will be observed as jets in the detector. An alternative process is the creation of a new, short-lived particles. In this thesis, the hard process of interest is $q\bar{q} \to Z/\gamma^* \to \tau^-\tau^+$.

Underlying Event: The cross section for soft QCD is large compared to the cross section for the hard scattering. The probability for the partons not participating in the hard scattering to interact softly is therefore non-vanishing. The soft interaction creates many soft jets.

Initial State Radiation (ISR): All partons can radiate gluons. The gluon will primarily be radiated parallel to the original parton. In ISR, most of the radiated gluons will move along the beam-axis and thus not detected. A gluon can be radiated in a large angle creating additional jets observed in the detector, but this happens rarely.

Final State Radiation (FSR): Like the initial state partons could radiate a gluon or a photon so can the final states. In case of lepton final states there will only be radiated photons since leptons do not couple to gluons.

Jet Fragmentation: Due to color confinement described in section 2.4 the initial state and final state radiated gluon and quarks, and partons from the hard scattering cannot be observed alone, they need to be in a color neutral state. The gluons and quarks will therefore radiate more soft and collinear gluons that can split into a quark pair to smear out the color charge they are carrying. At an energy scale of $\sim$ 1GeV the pertubative description of QCD breaks down. It is in this non-pertubative regime that hadrons (mostly pions) are created. This is what is defined as a jet.

Beam Remnants: A part of the beam will not participate in the hard process nor the underlying event and will continue along the beam axis. The beam remnants will carry color charge and will thus interact with the rest of the collision (the hard scattering and the underlying event).
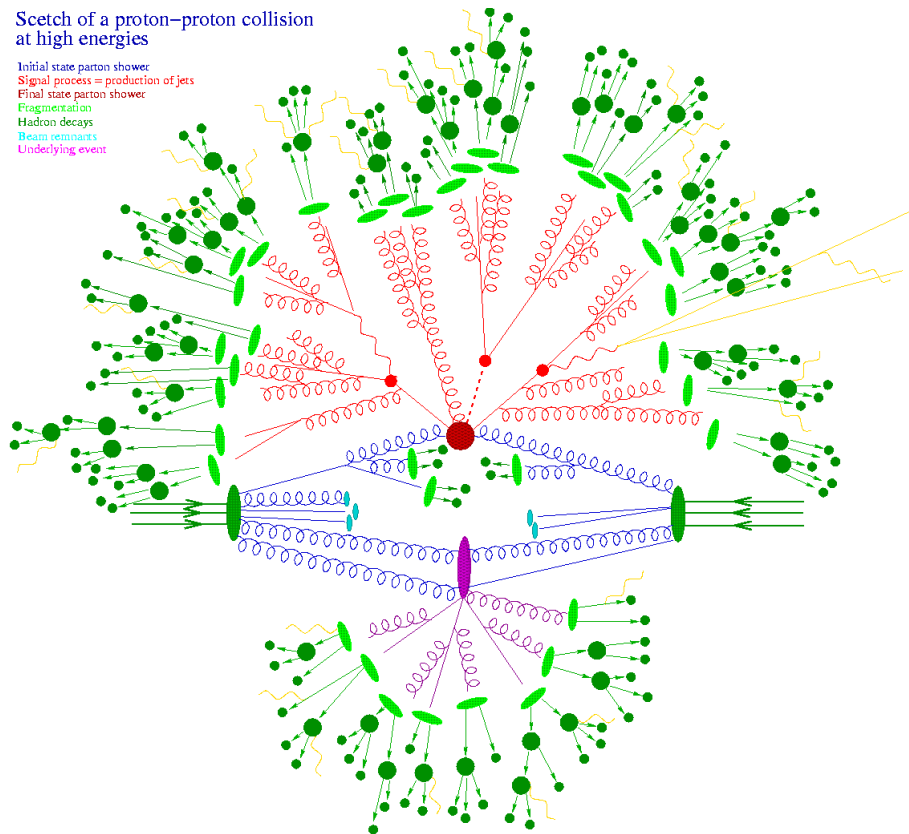
Figure 4.1: Schematic overview of a proton collision.[17]

We see that even though we are only interested in the hard process in hadron collisions we will get extra collisions in the underlying event and jets from initial state and final state radiation. The hard process studied in this thesis is $q\bar{q} \rightarrow Z \rightarrow \tau\tau$. The final state will therefore consist of two tau decays and is thus not as complicated as the final state in Figure 4.1.

The momentum along the beam-axis of the incoming partons is not known. The longitudinal momentum of the final state particles do therefore not carry much useful information. Under the assumption that the incoming partons move along the beam-axis, the initial transverse momentum is known to be zero, and the transverse momentum and energy are used to study the collisions. We therefore wish to split the momentum into momentum transverse to the hadron beam, p_T, and momentum parallel to the hadron beam, $p_{||}$. Instead of using $p_{||}$ rapidity is introduced, which is a relativistic generalization of speed and adds under Lorentz transformations. The rapidity is given by

$$y = \tfrac{1}{2} \ln \left(\frac{E + p_z}{E - p_z} \right) \tag{4.1}$$

where the z-direction is parallel to the beam-axis.

In the massless limit, $m^2 \ll E$, the rapidity reduces to the pseudorapidity, η, that is directly connected to the angle, θ, between beam axis and the direction of flight of the particle:

$$\eta = -\ln \left[\tan \left(\frac{\theta}{2} \right) \right] \tag{4.2}$$

Experimentally the pseudorapidity is used.

4.2   Parton Distribution Functions

The proton, as described previously, consists of three valence quarks and a sea of gluons and quark-anti-quark pairs. For the description of parton-parton interactions, the concept of parton distribution functions is introduced. The parton distribution functions (PDFs) can to lowest order be described as the probability of finding a given parton with a specific momentum fraction inside the proton.

The parton distribution functions, $f_i(x)$, depend on the energy fraction, x given by

$$x = \frac{|\vec{p}_{parton}|}{|\vec{p}_{proton}|} \tag{4.3}$$

and the momentum transfer between partons inside the proton, Q. In the case of Z production. the average x will be

$$\langle x \rangle = \frac{M_Z}{\sqrt{s}} = \frac{91.1876 \text{ GeV}}{7 \text{ TeV}} \approx 1.30 \cdot 10^{-2} \tag{4.4}$$

since a energy corresponding to the mass of the Z will be needed to create a Z boson.

The energy of the hard scattering squared, $\hat{s}$, puts further restrictions on the momentum fraction of the incoming particles, x_1 and x_2, by requiring:

$$\hat{s} = x_1 x_2 s \tag{4.5}$$

where s is the collision energy of the protons squared.

In Figure 4.2 parton distribution functions for two different momentum transfers are shown. It is seen that the dominant parton is the gluon which at the average value of

x is an order of magnitude larger than the quarks. Notice that for high values of x the dominant parton distribution functions are the u and d quarks. This is due to the up and down quarks being the valence quarks.
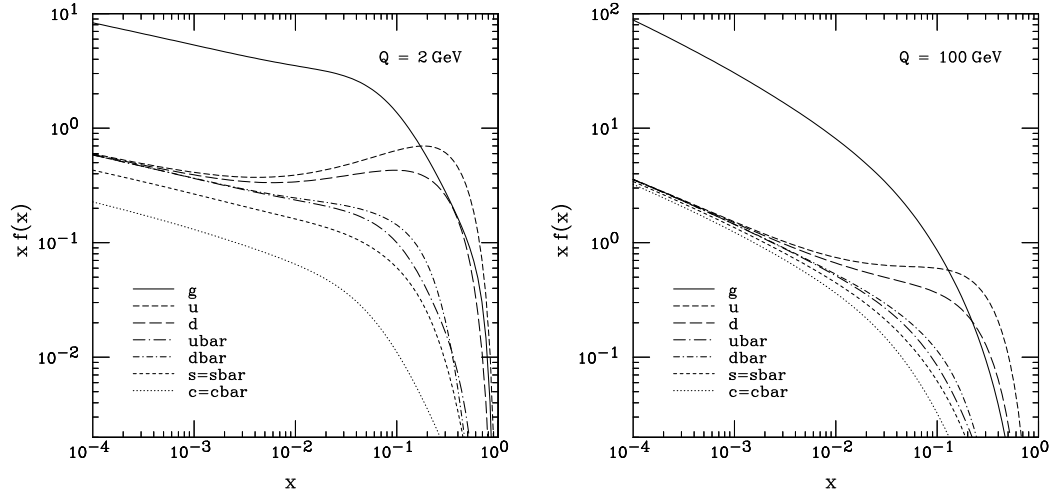
Figure 4.2: Parton distribution functions from CTEQ6M[18].

Even though the gluon is dominating for low values of x it is not a leading order part of the creation of Z bosons since they can only be created in quark-anti-quark annihilation. However, at next-to-leading order (NLO) the gluons play a part in the creation of Z bosons, since gluons can split into quark-anti-quark pairs which then can interact with quarks from the other proton. In Figure 4.3 the NLO processes for $pp \to Z/\gamma^* \to \tau\tau$ are shown.
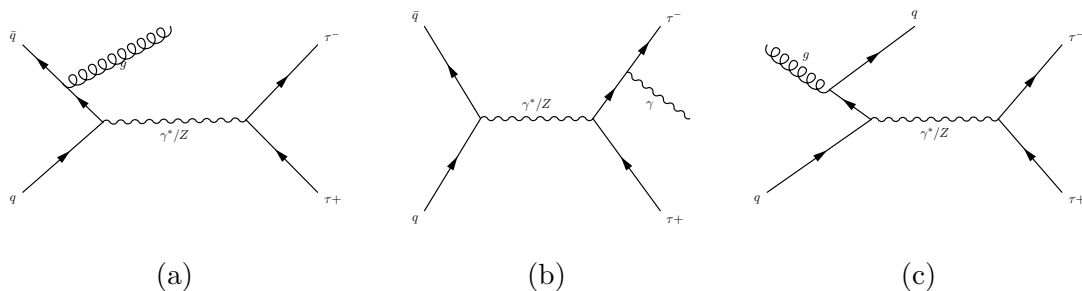
Figure 4.3: Next to leading order Feynman diagrams for the $Z/\gamma^* \to \tau\tau$ process. The diagrams are initial state gluon radiation (a), final state photon radiation (b), and initial state gluon splitting (c).

4.3 Cross Sections at a Hadron Collider

A cross section, σ, of a process is a measure of the probability of that process to take place. It is measured in barns, b, and the amount of data, the integrated luminosity, $\mathcal{L}$, is measured in inverse barns, b^{-1}. The expected number of events, N, of a given process is given as

$$N = \sigma\mathcal{L} \tag{4.6}$$

Cross sections are calculated from known initial states, but there are, as described in Section 4.2, multiple initial states in hadron collisions with different momentum fractions, x_a and x_b. The cross section of a process $ab \to X$ can be calculated by averaging over all initial states and convolute the cross section with the respective parton distribution functions. This is known as the factorization theorem and is given by: [19]

$$\sigma_{AB} = \int \, dx_a \, dx_b f_{a/A} \left(x_a, Q^2\right) f_{b/B} \left(x_b, Q^2\right) \sigma_{ab \to X} \tag{4.7}$$

The cross section of the hard scattering, $q\bar{q} \to Z/\gamma^* \to ff$, $\sigma(\hat{s})$, is given by Equation 3.2. Using Equation 4.7 the differential cross section of the hard scattering is found to be

$$\frac{d\sigma}{d\hat{s}} (pp \to \ell\ell X) = \sigma(\hat{s}) \int \, dx_a \, dx_b f_{a/A} \left(x_a, Q^2\right) f_{b/B} \left(x_b, Q^2\right) \delta \left(1 - x_a x_b \frac{s}{\hat{s}}\right) \tag{4.8}$$

with the constraint on x_a and x_b given by Equation 4.5.

In Figure 4.4 cross sections for the production of various particles are shown as a function of the collision energy. From this it is seen that it will only be one in a million events that produces a Z boson. The W boson will be produced 10 times as often due to the lower mass of the W boson and the V-A couplings of the Z described in Section 2.3.

4.4 Event Generators

In particle physics, simulations play a major role. Due to the complexity of the theory, simulations of what we expect are compared to data to see if there are any deviations and measure properties as for example the tau polarization. All event generators use a Monte Carlo method to generate random events with the frequency that we expect from Nature. Instead of providing all different processes simultaneously, the event generators generate one event type at a time, which must then be reweighted according to their respective cross section.

There are several event generators available for proton-proton collisions and they treat the different parts of the collisions described in Section 4.1 in various ways. Many simulations use a combination of two or more event generators each providing the simulation of one or more of the parts of a proton collision.

Event generators can be split into two groups, parton shower generators and matrix element generators.

The parton showering (PS) generators calculate the hard process to lowest order. A showering algorithm is then performed on the outgoing partons so they radiate gluons and the gluons split into quark pairs. When the invariant mass of the partons is sufficiently
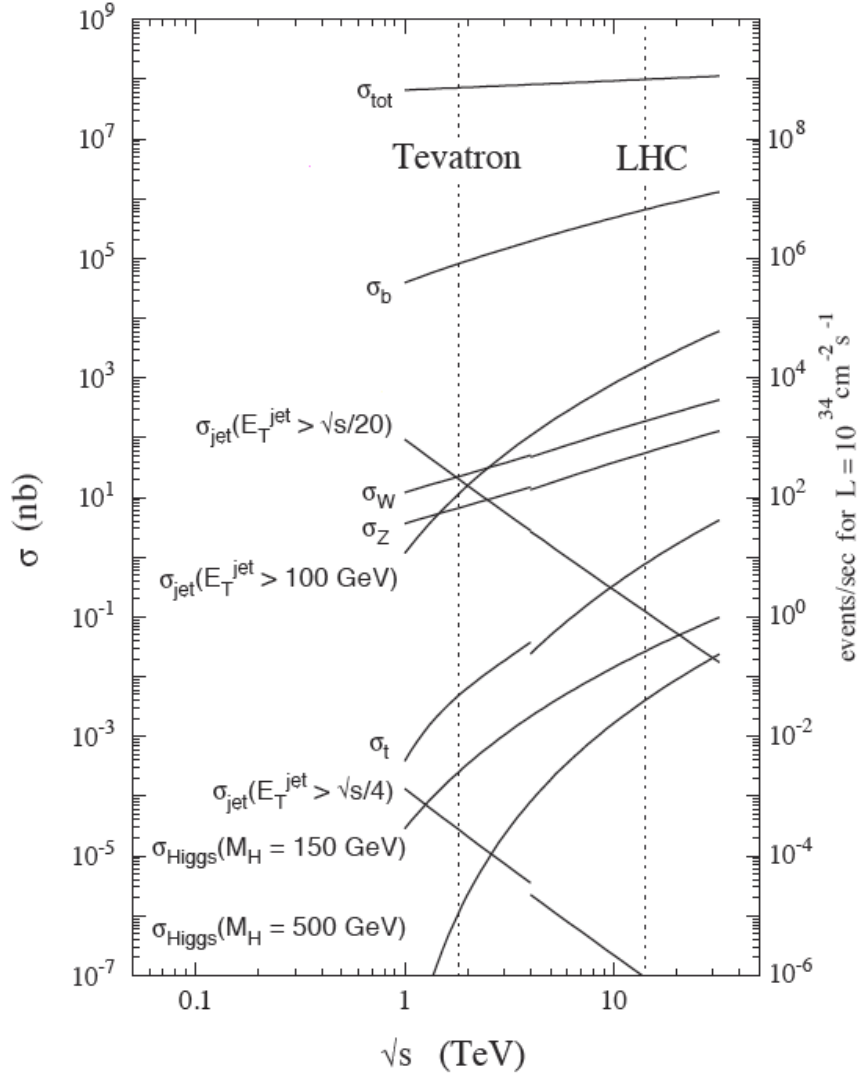
Figure 4.4: Cross sections at the Large Hadron Collider.[20] Please note that the Large Hadron Collider was running at $\sqrt{s} = 7$ TeV in 2011 and the cross section should be evaluated at that energy.

low ($\sim$ 1GeV), the pertubative gluon and quark radiation breaks down and the partons are combined into colorneutral states. The original partons will then have evolved into jets.

The matrix element (ME) generators calculate the matrix elements to leading order with different number of final state partons, i.e. $Z \to \ell\ell$ + additional jets created from initial and final state radiation as shown in Figure 4.3. The ME generators do not include any hadronisation and the final state is single partons. To get to an observable state, the jets must be created with a parton showering algorithm.

In Figure 4.5 the difference between the matrix element and the parton shower approach is shown.
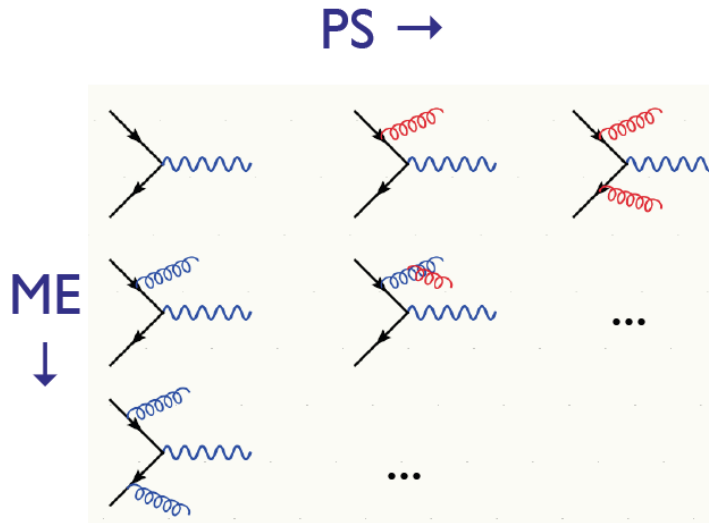
Figure 4.5: Graphical interpretation of the matrix element (ME) method versus the parton shower (PS) method.[21] All the blue gluons are calculated exact with matrix elements and all the red gluons are produced with parton showering algorithms.

Besides the many event generators there exist programs made for a specific parts of the physics processes. TAUOLA, for example, provides a detailed description of tau decays.

In the following, descriptions of the event generators used for simulations in this thesis are presented.

PYTHIA

Pythia[22] is a widely used general purpose event generator in high energy physics for both Standard Model and Beyond the Standard Model physics. The advantage of Pythia is that it simulates all the parts of a proton collision, from the hard process to the underlying event, to beam remnants, to jet formation. For the parton distribution functions, Pythia uses CTEQ 5L[23] as default for protons.

The hard scattering processes in Pythia is limited to leading order $2 \rightarrow 2$, and $2 \rightarrow 1$ processes. Additional jets are created through hard radiation during the parton showering mechanism. Pythia is therefore not good at estimating the cross section for events with a high jet multiplicity in the final state.

The underlying event consists of multiple parton interactions and scatterings. In Pythia the underlying event is described as several independent $2 \rightarrow 2$ processes along with prompt photons, charmonia and bottomonia creation, low-mass Drell-Yan pairs, and t-channel $\gamma^*/Z^0/W^\pm$ exchange. The many scattering partons are color connected to each other and to the beam remnants.

Pythia uses the Lund string fragmentation model[24] for hadronisation, where quark pairs are held together by a color string which represents a gluon. When the quarks move apart the color string will break creating a new quark pair. When the energy of the quarks is sufficiently low they can no longer break the color strings and hadrons will be formed.

HERWIG

Herwig[25] is a general purpose event generator simulating all parts of a proton collision. It works in many ways like Pythia, but can be interfaced with more programs than Pythia. It has available a large number of $2 \to 2$ processes both for the Standard Model and Super Symmetry. It decays almost all particles with full spin correlations, but can also be interfaced to programs dedicated to special particle decays. The main focus of Herwig is a detailed simulation of QCD jets. As with Pythia, the hard processes are treated at tree level, and additional radiated partons are generated through the parton showering process.

The underlying event is originated from a minimum bias pp generator developed by UA5, but modified to use the hadronisation algorithm developed in Herwig.

The hadronisation process in Herwig is cluster based. Partons are, after parton showering, combined into colorless clusters of either quark-anti-quark pairs or diquark-anti-diquark pairs. If the formed clusters are too light to decay into two hadrons the cluster is formed into a light hadron. If the cluster is heavy enough to decay into two hadrons, it will do so and the decay products will continue to decay until the clusters are too light to decay.

AlpGEN

AlpGEN[26] is a Matrix Element generator. It is designed for generating Standard Model processes in hadronic collisions with main focus on final states containing multiple jets. The processes $Z/\gamma^* \to f\bar{f} + N$ jets and $W \to f\bar{f}' + N$ jets processes have been calculated with $N_{\text{jets}} \leq 6$.

Parton showering is not included in AlpGEN and must be handled by another program, for example Herwig or Pythia with which Alpgen can interface. After parton showering the showers must be matched to the matrix element to avoid double counting.

MC@NLO

MC@NLO[27] is a matrix element event generator with the hard scattering calculated including Next-to-Leading-Order QCD corrections. MC@NLO includes cross sections for electroweak processes, and $t\bar{t}$ and $b\bar{b}$ production. It can simulate final state with two or three jets. To get the correct jet multiplicity MC@NLO interfaces with Herwig to create parton showers and hadronisation. Since the jet multiplicity in the hard scattering is limited it is not as precise in predicting the jet multiplicity as Alpgen.

The Underlying Event

There exists dedicated generators for underlying events. One of those is JIMMY[28] which uses a leading order multiple scattering model. It can be interfaced with Herwig to generate the underlying event instead of the generator included in Herwig.

TAUOLA

TAUOLA[29] is a program made specifically to handle tau decays. It takes into account all the spin effects of the particles that the taus originate from and calculates the kinematics of the tau decay products according to their helicity. It can be interfaced with both Herwig and Pythia. If the taus have already decayed in the preceding event generator TAUOLA will "undecay" them and afterwards decay the taus properly.

Detector Simulation

To compare simulations to real data, the events generated by an event generator will be propagated through a detector simulation, so detector responses will be available for the comparison. In ATLAS the detector simulations can be done with two different programs, ATLFAST II[30] and Geant4[31]. Geant4 is more precise than ATLFAST II and is used for the detector simulations in all the used Monte Carlo samples in this thesis.

Geant4 is a full detector simulation where every final state particle is followed through the detector and all physics processes that can occur in interactions between the particle and the detector material is simulated. The response from every active detector element is simulated, and the signal is digitalized for the final output of the simulation to have the same structure as recorded data so all reconstruction algorithms can run on simulated data.

Part II

The Experiment

The Large Hadron Collider and the ATLAS Experiment

This chapter contains a short description of the Large Hadron Collider and the ATLAS Experiment. The main focus in this chapter is particle reconstruction and identification using the ATLAS detector.

5.1   The Large Hadron Collider

The Large Hadron Collider (LHC) is the largest particle accelerator on Earth. It is located at CERN (Conseil Européen pour la Recherche Nucléaire) at the boarder between France and Switzerland. CERN is a collaboration between the 20 European member states and non-member states from the rest of the world.

The Large Hadron Collider is approximately 27 km in circumference and lies 100 m below the ground. There are four interaction points where protons or lead ions are collided at high energies. At the four interaction points, gigantic experiments (ALICE, ATLAS, CMS and LHCb) are recording every detail of the particle collisions. The design collision energy for protons is 14 TeV, but the LHC has in 2010 and 2011 been run at a collision energy of 7 TeV, 3.5 TeV per proton beam. At this level of energy, the protons move with a speed very close to the speed of light.

The proton beams consist of 2808 bunches of protons 50 ns seconds apart. Each bunch contains $\sim 10^{11}$ protons so many proton collisions can happen at each bunch crossing. This is known as in time pile up. The protons are held in the accelerator ring by 1232 superconducting dipole magnets with a maximum magnetic field of 8.33 T. The beams are focused and defocused by 392 quadropole magnets.

In Figure 5.1 an overview of the accelerator complex at CERN is seen. The protons begin their acceleration in the linear accelerator LINAC 2, where they are accelerated from rest to an energy of 50 MeV. They are then fed to the Booster to be accelerated to 1.4 GeV after which they are injected into the Proton Synchrotron to be accelerated to 25 GeV. The last acceleration before the Large Hadron Collider is the Super Proton Synchrotron where they are accelerated to 450 GeV. In the LHC the protons are accelerated from 450 GeV to 3.5 TeV by radio frequency (RF) cavities situated on the ring between ALICE and CMS.

The Large Hadron collider is build to have a peak instantaneous luminosity of $L = 10^{34} \text{cm}^{-2}\text{s}^{-1}$ at ATLAS and CMS and many factors of tens lower at LHCb and ALICE. So far the design peak luminosity has not been reached and the maximum instantaneous

luminosity in 2011 was $L \approx 3.7 \cdot 10^{33} \mathrm{cm}^{-2}\mathrm{s}^{-1}$. In Figure 5.2 the integrated luminosity delivered by the LHC and recorded by ATLAS in 2011 is shown. It is seen that ATLAS has recorded over 90% of the collisions provided by the LHC which adds up to 5.25 fb^{-1} compared to the 45.0 pb^{-1} recorded by ATLAS in 2010. In this thesis all of the data of 2011 has been used for the analysis.
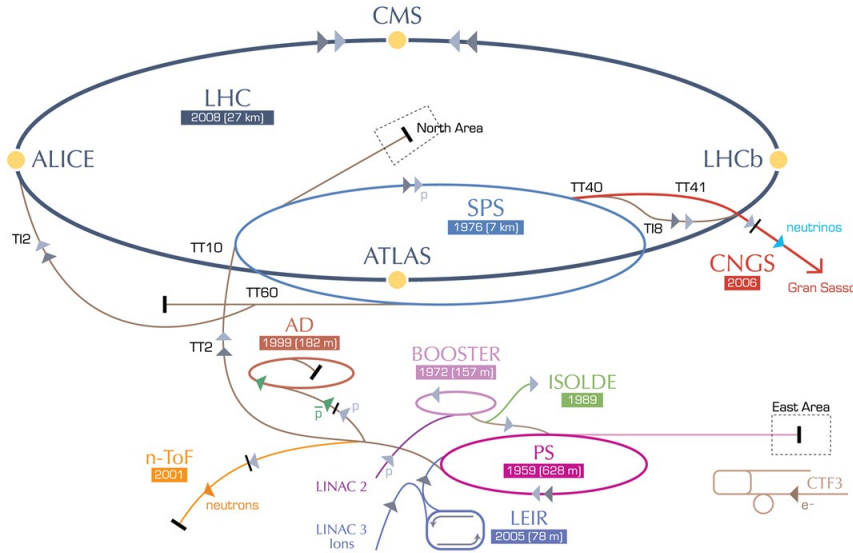
Figure 5.1: The accelerator complex at CERN. [32]
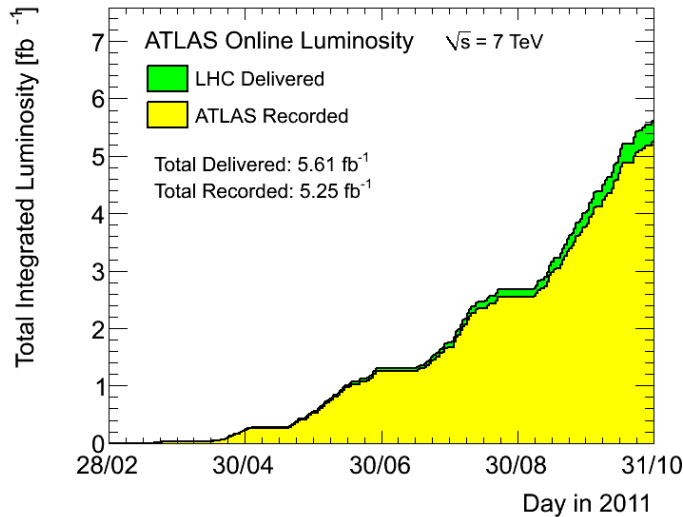
Figure 5.2: Integrated luminosity delivered by LHC (green) and recorded by ATLAS (yellow) in 2011.

There are four large detectors placed at the four interaction points at the Large Hadron Collider. Two of them, ATLAS and CMS, are general purpose detectors in the sense that they do not search anything specific, but cover a wide area of searches of physics beyond the Standard Model. The ALICE experiment is build to look at heavy ion collisions and in order to investigate the physics that governed the Universe shortly after the Big Bang. The LHCb experiment studies physics with b quarks and in particular CP violation which might describe the matter-antimatter asymmetry in our Universe.

5.2 The ATLAS Experiment

The ATLAS (A Toroidal LHC ApparatuS) detector is 44 meters long, 25 meters tall, 25 meters wide, and weighs approximately 7000 tons. It is build to explore particle physics at the TeV scale and look for phenomena not described by the standard model.

The xyz-coordinate system for ATLAS originates in the interaction point with the z-direction in the beam direction and x and y in the orthogonal plane with x pointing towards the centre of the LHC ring and y pointing upwards. Often a polar coordinate system is used, where instead of the polar angle, θ, we use the pseudorapidity introduced in Section 4.1, η.
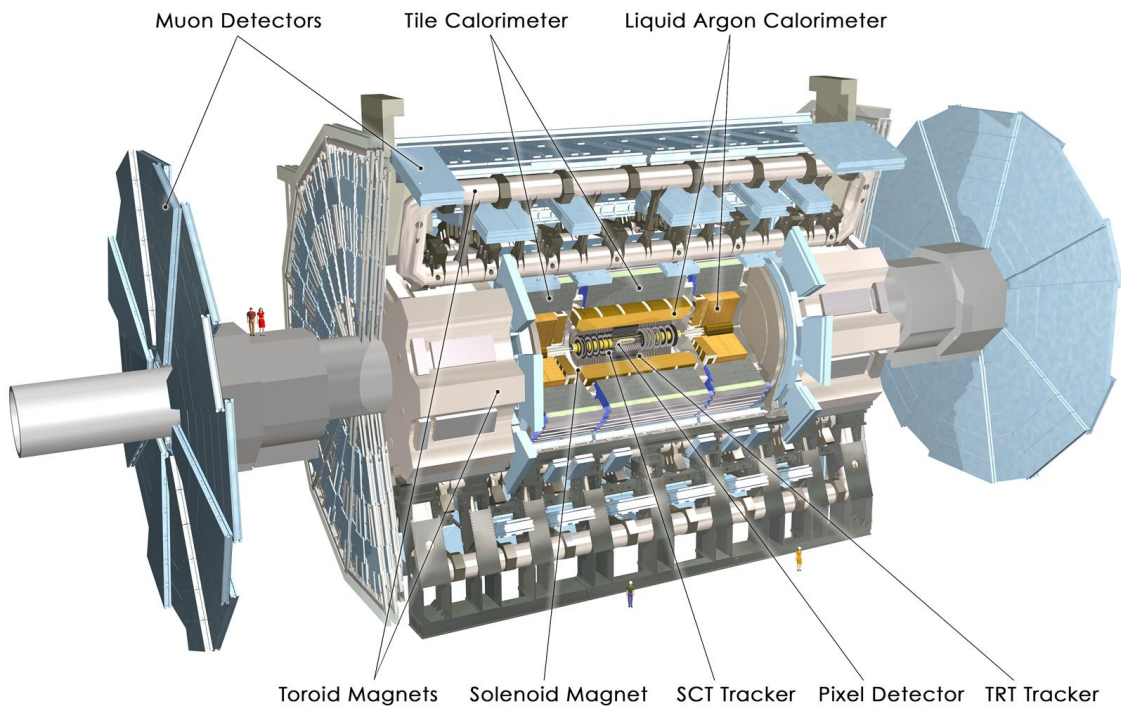
Figure 5.3: The ATLAS detector.[33] Please notice the size of the experiment by comparing to the humans standing in front of it.

In Figure 5.3 an overview of the ATLAS detector is shown. ATLAS consists of several subdetector systems each with a special task in measuring properties of the particles. From the centre and out the subdetector systems are the inner tracking detector, the electromagnetic calorimeter, the hadronic calorimeter, and the muon system. All of the subdetectors consist of a barrel detector around the centre of the collision and an end-cap detector to be able to detect particles with high η.

The Inner Detector

The purpose of the inner detector is to reconstruct trajectories of the charged particles traversing the detector with minimal energy loss and find secondary vertices from τ and b decays. An applied magnetic field bends the tracks of the charged particles and makes it possible to measure the momentum and the charge of the particles as well.

The inner detector consists of three subdetectors, the pixel detector, the silicon tracker (SCT), and the transition radiation tracker (TRT) shown in Figure 5.4.
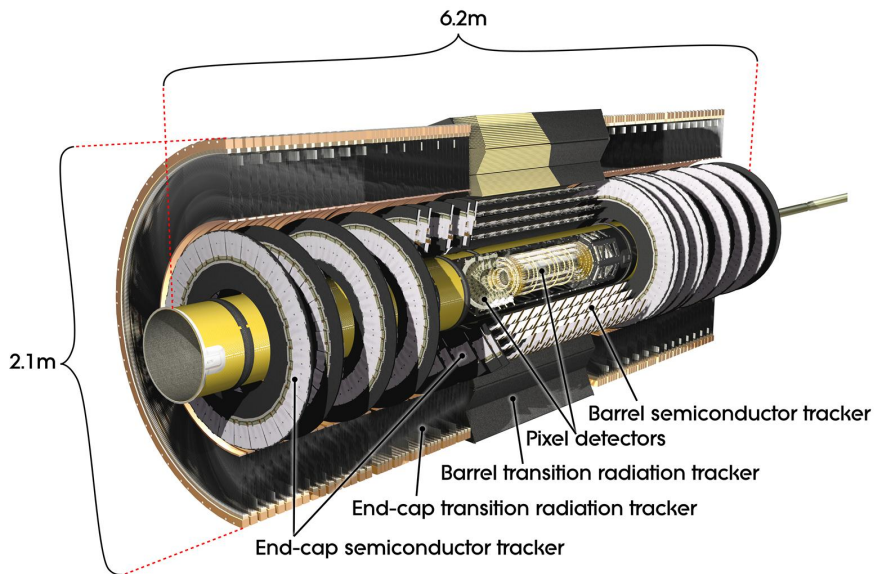
Figure 5.4: The inner detector ATLAS. [33]

The Pixel Detector

The pixel detector is build of three cylindrical pixel layers in the barrel region at a radii of ~ 5 cm, 9 cm, and 12 cm and three disks at each side of the interaction point as end-cap detectors with a distance between 9 cm and 15 cm away from the interaction point. There are 1456 pixel modules in the barrel detectors and 288 in the end-cap detectors. The pixel detector covers $|\eta| < 2.5$ and a charged particle leaves three hits. The pixel detector provides a measurement of the hit in three dimensions. The accuracy of the pixel detector

is 10 μm in the $R - \phi$ plane and 115 μm in the z direction in both barrel and end-cap regions.[33]

The Silicon Tracker

The silicon tracker (SCT) covers the same η region as the pixel detector, $|\eta| < 2.5$. The SCT uses semiconductor silicon strips to measure the passage of a charged particle. It consists of 4 cylindrical modules each of 2 layers of silicon microstrips in the barrel region and nine disks on each side of the interaction point. A charged particle will leave 8 hits in the SCT. The SCT measures the track hits in three dimensions and has a precision of 17 μm in the $R - \phi$ plane and 580 μm in the z direction in both barrel and end-cap regions.[33]

The Transition Radiation Tracker

The transition radiation tracker (TRT) is a straw tube detector consisting of ~ 400000 4 mm thick straws. It can measure the tracks within $|\eta| < 2.0$ and only in the $R - \phi$ plane. The trajectories are reconstructed by particles hitting the straws and a charge particle will leave a large number of hits (approximately 36 per track). In the end-cap region region straws are arranged radially in wheels. The precision of the TRT is 130 μm per strawtube.[33]

Besides measuring the track of the particles the TRT also provides a separation between electrons and charged pions by their different transition radiation. The transition radiation is the radiation of particles, when they move between media with different refractive indices. The TRT exploits that the transition radiation is different for electrons and charged pions.

The Magnet System

Just outside the inner detector is the central solenoid magnet providing a magnetic field of 2 TeV aligned with the beam axis. It is this magnet that gives the possibility of measuring the momentum and charge of the charged particles traversing the inner detector by measuring the bending of the tracks. Since the magnet is in front of the calorimeters the amount of material in the magnet is kept at a minimum to avoid too much energy loss.

The muon system is placed within another magnet system. The toroid magnets bend the trajectories of the muons improving the momentum resolution of the muons. The toroid magnet system consists of three air-core toroids, one barrel toroid and two end-cap toroids, with 8 coils each.

The Electromagnetic Calorimeter

The electromagnetic calorimeter measures the energy of electrons and photons by stopping the particles. It consists of a barrel detector covering $|\eta| < 1.475$ and two end-cap detectors covering $1.475 < |\eta| < 3.2$. The end-cap detector is divided further into two subdetectors covering $1.375 < |\eta| < 2.5$ and $2.5 < |\eta| < 3.2$.

The detector is build up by layers of lead that absorb the energy of the particles and liquid argon that measures the energy of the electromagnetic shower generated by the particles interacting with lead. In the electromagnetic calorimeter the layers are accordion shaped in the radial direction to ensure full ϕ coverage with no cracks (Figure 5.5).
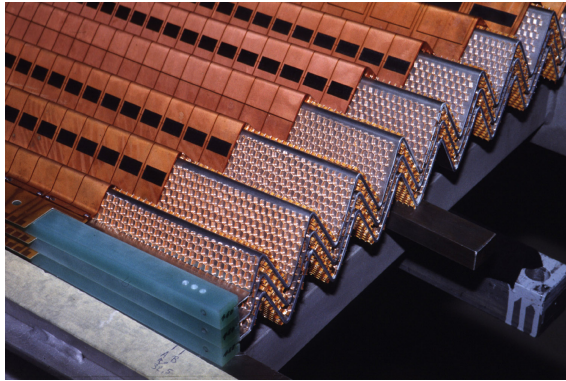

Figure 5.5: The accordion geometry of the electromagnetic calorimeter. [33]

The electromagnetic calorimeter has three calorimeter layers for $|\eta| < 2.5$ and two layers in $2.5 < |\eta| < 3.2$. In the region $|\eta| < 1.8$, a presampler calorimeter is installed to correct for energy loss before the electromagnetic calorimeter. The presampler is a thin liquid argon plate that measures the energy before the particles hit the lead in the rest of the detector. Since the only purpose of the presampler is an energy measurement its granularity is lower than the rest of the calorimeter. The three layers in the central part of the calorimeter are divided into $\Delta\eta \times \Delta\phi$ cells with different granularity. The second layer is thickest and has a granularity of 0.025×0.025.[33]

The energy resolution of the electromagnetic calorimeter is $\sigma_E/E = 10\%/\sqrt{E} \oplus 0.7\%$ in both the barrel and end-cap regions.

The Hadronic Calorimeter

The purpose of the hadronic calorimeter is to measure the energy of particles that interact through the strong force, i.e. hadrons, and thereby also hadronically decaying taus, by stopping them. It is a sampling calorimeter like the electromagnetic calorimeter with sampling layers that measure the energy, and layers of dense material that create particle showers.

The hadronic calorimeter covers up to 4.9 in $|\eta|$ and is divided into several sub-systems. In the barrel region ($|\eta| < 1.7$) is the central tile calorimeter ($|\eta| < 1.0$) and an extended barrel on each side covering $0.8 < |\eta| < 1.7$. The sampling material in the tile calorimeter is scintillating tiles, that becomes fluorescent when it is hit by a charged particle. The $\Delta\eta \times \Delta\phi$ granularity in the tile calorimeter is in the range of 0.1×0.1 to 0.2×0.1.

There are two types of calorimeters in the end-cap region, the liquid argon end-cap calorimeter (HEC), and the liquid argon forward calorimeter (FCAL).
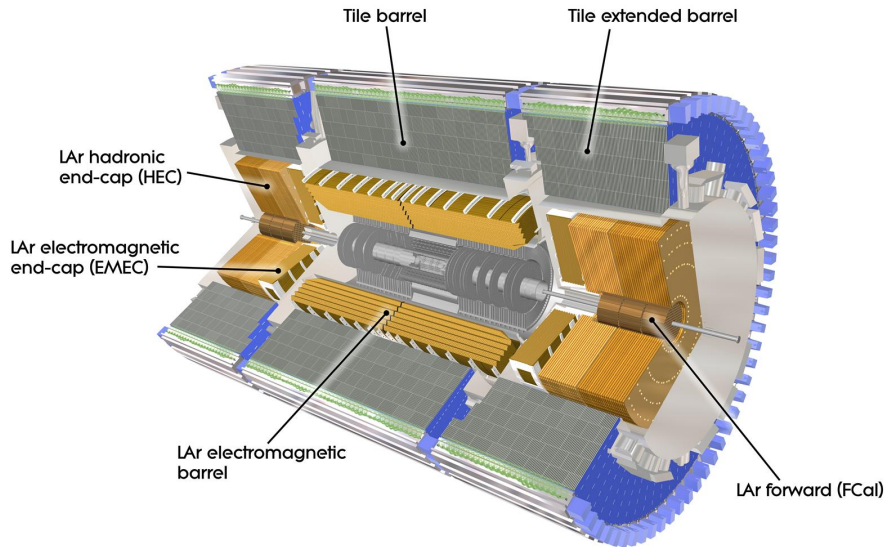
Figure 5.6: The electromagnetic and hadronic calorimeter in ATLAS. [33]

The end-cap calorimeter covers $1.5 < |\eta| < 3.2$. The sampling material of HEC is the same as in the electromagnetic calorimeter, liquid argon, and the stopping material creating showers is copper. It has a $\Delta\eta \times \Delta\phi$ granularity of 0.1×0.1 for $1.5 < |\eta| < 2.5$ and 0.2×0.2 for $2.5 < |\eta| < 3.2$.

The forward calorimeter also uses liquid argon as the active material. As the stopping material is copper (inner disk) and tungsten. The η region covered by FCAL is $3.1 < |\eta| < 4.9$. The large η region is due to measurement of missing transverse energy, where it is important that no energy escapes detection.

The energy resolution of the barrel and the end-dap calorimeters is $\sigma_E/E = 50\%/\sqrt{E} \oplus 3\%$ and for the forward calorimeter the energy resolution is $\sigma_E/E = 100\%/\sqrt{E} \oplus 10\%$.[33]

The Muon Spectrometer

Because of their relatively high mass the non-strongly interacting muons are very penetrating and traverses the calorimeter system. The toroid magnets provides a magnetic field that bends the tracks of the muons so the momentum can be measured with high precision.

The muon spectrometer covers $|\eta| < 2.7$ and consists of four different types of detectors, monitored drift tubes (MDT), cathode strip chamber (CSC), resistive plate chambers (RPC), and thin gap chamber (TGC) (Figure 5.7). The MDTs and the CSCs are used for precision tracking while the RPCs and the TGCs are used to trigger on muons and measure the muon momentum orthogonal to the momentum measured by MDTs and CSCs.
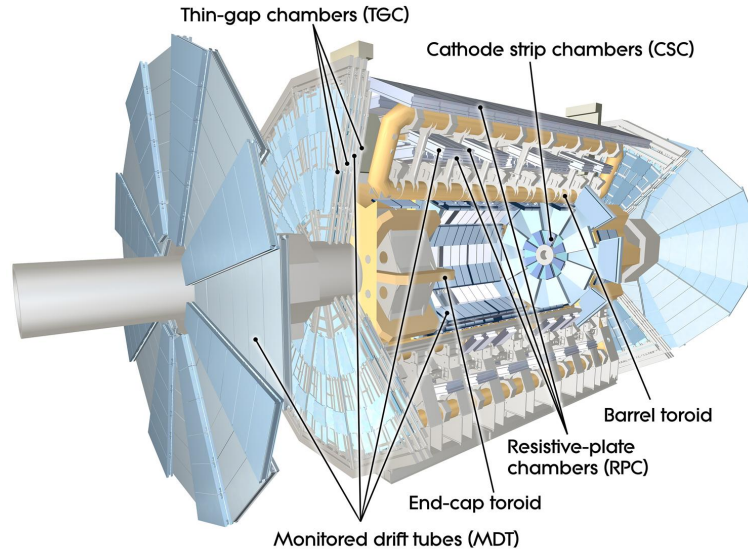
Figure 5.7: The muon spectrometer system in ATLAS. [33]

Trigger and Data Acquisition

As seen in Figure 4.4, the total cross section is large compared to the cross section of processes of interest as W, Z, and Higgs production. The collisions will therefore undergo a selection before the data is recorded, the collision will have to *trigger* the data recording. An event that will fire a trigger can for instance be an event having high a p_T physics object such as an electron, photon, muon, tau or jet.

The trigger system of ATLAS is build of three parts called Level 1 (L1), Level 2 (L2), and Event Filter (EF). Each trigger system is more sophisticated than the previous.

L1 is a hardware trigger system that searches for regions in the detector where a high p_T physics object is identified. The L1 trigger looks for muons, electrons/photons, taus, and jets in the muon spectrometer and the calorimeters. The Level 1 trigger system has to make a decision on whether to fire or not within $2.5\mu s$ and has a maximum firing rate of 75 kHz. If an event passes a L1 trigger, it is passed on to the Level 2 trigger system. L1 provides L2 with the Regions of Interest (RoIs) corresponding to the trigger objects identified at L1.

The Level 2 trigger system reconstructs all data in the RoIs and from that information makes a decision within 40 ms whether the event is of interest or not. The L2 system reduces the maximum rate from 75 kHz to 3.5 kHz. If an event passes a Level 2 trigger, it is passed to the Event Filter trigger system.

The EF trigger system investigates the event further and can combine several L1 and L2 triggers to make complex event composition. Normally, the data is only reconstructed in the RoIs, but some event filter triggers reconstructs response from the whole detector. The EF system reduces the maximum rate to 200 Hz.

L1 triggers are hardware based, whereas L2 and EF triggers are software based and are run on large computer farms.

The naming scheme for triggers is that it starts with the trigger system (L1, L2, or EF), then provides the kind of particle that triggered (j(et), mu(on), e(lectron), tau, x

(missing E_T), and so on) and finally the momentum cut given in GeV.

Some triggers fire too often and are therefore prescaled. Prescaled triggers will only be passed to the next trigger level once for every n times it fires, where n is the prescale.

The data are written out into three different streams depending on the event filter trigger. The three streams are Muon, Electron and JetTauEtmiss. It is very likely that one event fires more than one type of EF trigger. A bookkeeping system is required to ensure that the same event is not used more than one time in the analysis.

5.3 Particle Identification with the ATLAS Detector

The detector is build in such a way that different physical objects leaves different traces so particles are reconstructed and identified by the fingerprints they leave in the detector. In Figure 5.8 the characteristic left by different particles traversing the ATLAS detector is shown.
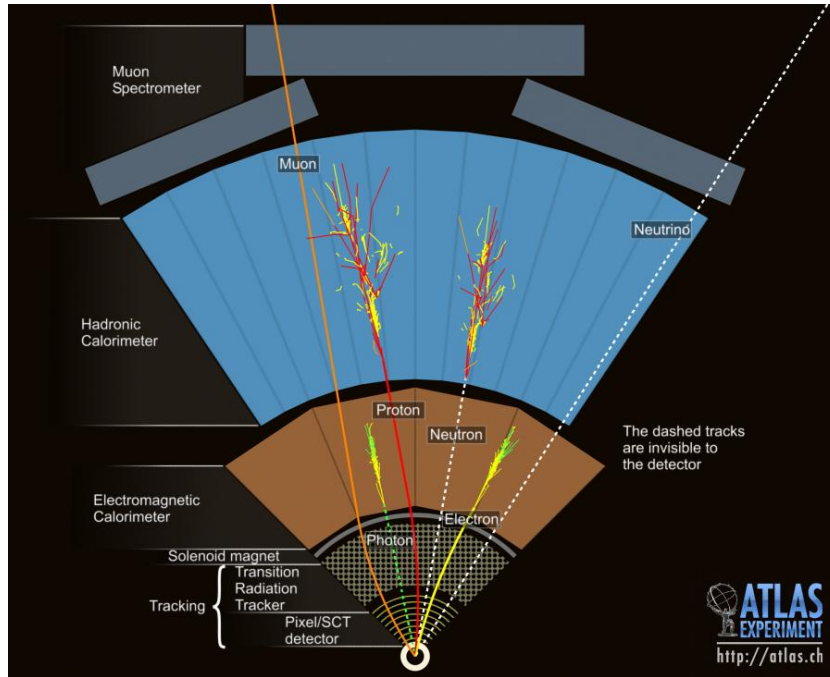
Figure 5.8: The characteristics of different particles traversing the ATLAS detector.[34]

Jet Reconstruction

Clusters are formed by combining cells in the calorimeter with an energy deposit over a certain threshold (topological clusters). Jets are then reconstructed by combining clusters using jet finding algorithms.

The ATLAS experiment uses an algorithm where clusters are paired together depending on their distance and their energy. The jet reconstruction algorithm used by ATLAS is the anti-k_T algorithm. [35]

The distance between to objects is

$$d_{ij} = \min\left(p_{T_i}^{-2}, p_{T_j}^{-2}\right)\frac{(\Delta R_{ij})^2}{R^2} \tag{5.1}$$

where $\Delta R_{ij} = \sqrt{(\eta_i - \eta_j)^2 + (\phi_i - \phi_j)^2}$. The radius parameter, R, used for jet reconstruction in this thesis is 0.4 and the jet p_T reconstruction threshold is 7 GeV. If the smallest d_{ij} is smaller than the threshold momentum, p_T^{-2}, jet i and j are joined. If it is equal or larger than the threshold momentum, p_T^{-2}, the jet is taken as an individual jet. The anti-k_T algorithm will group the objects with highest p_T first.

Electron Reconstruction and Identification

Electrons are reconstructed from clusters in the electromagnetic calorimeter and must be matched to a track in the inner detector.[36]

To avoid hadronic jets faking the electron reconstruction, a cutbased method is used to identify electrons. There are three levels of cuts, loose, medium, and tight, with increasing jet rejection. The loose cut consists of simple cuts on the shape of the shower and with a loose matching between the track and the calorimeter clusters. The medium cut makes a tighter cut on the shower shape using the shape in the first part of the calorimeter and includes cut on the quality of the track in the inner detector. The tight cut increases the cut on the track cluster matching and uses the TRT to eliminate pions.

Muon Reconstruction and Identification

Muons can be reconstructed either with a track in the inner detector matched to a hit in the muon spectrometer (Combined muons) or only hits in the muon spectrometer (Standalone muons). The combined muons are only available within $|\eta| < 2.5$ since it is the coverage of the inner detector.

The muons used in this thesis are combined muons reconstructed by the Staco algorithm[37] which begins with hits in the muon spectrometer and propagates the track inwards to match it to a track in the inner detector taking into account the energy loss of the muon when it traverses the detector. The Staco algorithm uses statistical tools to match tracks to hits in the muon spectrometer.

To reduce the number of fake muons, cuts on the track quality can be applied.

Tau Reconstruction and Identification

Taus refer to hadronically decaying taus, since the leptonically decaying taus will be reconstructed and identified as muons or electrons.

Hadronic tau identification uses reconstructed jets as basis. All jets are thus considered as reconstructed taus. Tracks with $p_T > 1\text{GeV}$ satisfying a set of track quality requirements are matched to the reconstructed tau if the distance, ΔR, from the jet axis is less than 0.2. [38]

In order to separate taus from the overwhelming background of QCD jets, cuts are performed on the substructure of the tau candidate. The tau identification requires that the reconstructed tau has collimated energy deposit in the calorimeter, few number

of isolated tracks (if there is more than one, they should be collimated as well), and a good geometric matching between the tracks and the energy deposit.[38] There are three different methods for identifying taus, the cut-based (Cut), the likelihood-based (LLH), and the boosted decision tree (BDT). All three methods have three levels of cuts, loose, medium, and tight, with increasing jet rejection. The LLH and the BDT are both multivariate methods. In this thesis the boosted decision tree-based jet discriminant is used.

Since electrons can fake taus, an electron veto cut is also applied in tau identification. There are two methods, cut-based, and boosted decision tree-based. In this thesis the boosted decision tree-based electron veto is used.

The energy of the taus are calibrated using Monte Carlo samples. The tau energy scale has an uncertainty of $2.5\% - 3\%$ depending on the momentum of the taus and the η region. [38]

Reconstruction of Missing Transverse Energy

The Missing Transverse Energy (MET) holds information on the particles that do not interact in the detector and thus leave no trace, such as neutrinos.

The Missing Transverse Energy can either be measured using cells in the detector or reconstructed and identified objects. The algorithm used in this thesis to reconstruct the MET is cell-based and known as MET_RefFinal.

The cell-based reconstruction uses the energy from the calorimeter, corrected for the energy loss in the cryostat (cooling) and the energy of the muons. The calorimeter cells are associated with high p_T reconstructed and identified objects such as electrons, muons, taus, jets, etc. The energy of the objects are calibrated according to the object type. Overlap-removal is performed to eliminate double counting. Besides the cells associated with objects the cells not matched to any objects are also included.[37]

The MET is calculated as

$$
\begin{aligned}
\vec{E}_T^{\text{miss}} = & -\left(\vec{E}_T^{\text{RefEle}} + \vec{E}_T^{\text{RefGamma}} + \vec{E}_T^{\text{RefTau}} + \vec{E}_T^{\text{RefJet}} + \vec{E}_T^{\text{RefMuon}} + \vec{E}_T^{\text{CellOut}} \right) \\
& + \vec{E}_T^{\text{miss,Cryo}} + \vec{E}_T^{\text{miss,Muon}}
\end{aligned}
\tag{5.2}
$$

where $\vec{E}_T^{\text{RefObj}}$ is the transverse energy of the associated objects, $\vec{E}_T^{\text{CellOut}}$ is the transverse energy of the cells not associated with an object, $\vec{E}_T^{\text{miss,Cryo}}$ is the MET from the cryostat and $\vec{E}_T^{\text{miss,Muon}}$ is the MET from the muon spectrometer. In Figure 5.9 the MET calculation is shown schematically.
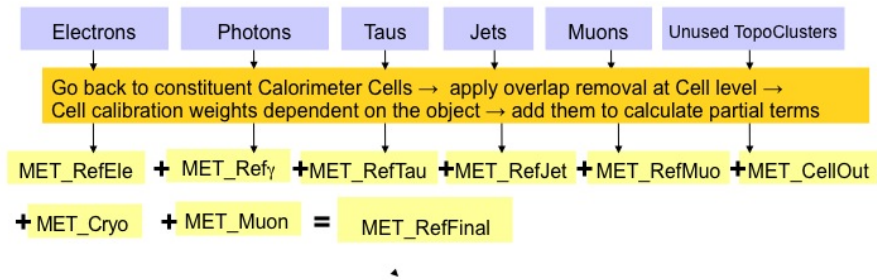
Figure 5.9: The Missing Transverse Energy refined final reconstruction. Courtesy of the ATLAS JetETmiss Group.

Part III

Analysis

$Z \rightarrow \tau\tau$ Selection

This chapter describes the selection of events that will be used in the measurement of the tau polarization in Z decays. The events we wish to select are events where one tau has decayed to a muon and one tau to hadrons known as the semileptonic channel.

The event selection is inspired by the $Z \rightarrow \tau\tau$ cross section measurement at the ATLAS experiment[39], but has been modified to run over the full 2011 data set.

6.1 Data set and Monte Carlo Samples

The data sample used for this analysis is the full 2011 data set. First one needs to ensure that the run is on the GoodRunsList (GRL) since some of the data recorded can be flagged bad as in some parts of the detector. In this analysis all parts of the detector are used and they must therefore all be well functioning in all the runs. The luminosity of the data sample is calculated from the GRL and the trigger used. It was calculated to be 4.63 fb^{-1} corresponding to 88% of the data recorded by ATLAS.

There are background processes that can mimic $Z \rightarrow \tau\tau$, both electroweak and QCD. The electroweak backgrounds taken into account in this analysis are $Z(\rightarrow \mu\mu)$ + jets, $W(\rightarrow \mu\nu_\mu)$ + jets, $W(\rightarrow \tau\nu_\tau)$ + jets, WW, WZ, ZZ, and top pair production. The W + jets backgrounds can fake a signal by a jet faking a tau. $Z \rightarrow \mu\mu$ fakes the signal primarily by a muon being misidentified as a tau. In WW, WZ, ZZ, and top pair production events two taus can be produced and thereby fake the signal.

For the signal process, a Monte Carlo sample generated with AlpGEN, hadronised with Herwig, and with the underlying event simulated by JIMMY, is used. The W + jets backgrounds are simulated with the same tools as the signal. The $Z \rightarrow \mu\mu$ sample is generated with Pythia, the diboson samples are generated with Herwig and the top pair production with MC@NLO. In all samples the taus are decayed using TAUOLA. In Table 6.1 all used Monte Carlo samples are listed with their integrated luminosities calculated using the cross sections given in Reference [40].

The 2011 runs are split into run periods A to M. Run periods B-M are used in this analysis. The Monte Carlo samples are split into four different run numbers, each simulating collision conditions and triggers in the different run periods.

Process	Event Generator	Luminosity [fb^{-1}]
$Z/\gamma* \to \tau\tau + 0$ jets ($M_Z > 40$GeV)	AlpGEN+Herwig+JIMMY	12.7
$Z/\gamma* \to \tau\tau + 1$ jet ($M_Z > 40$GeV)	AlpGEN+Herwig+JIMMY	19.8
$Z/\gamma* \to \tau\tau + 2$ jets ($M_Z > 40$GeV)	AlpGEN+Herwig+JIMMY	19.9
$Z/\gamma* \to \tau\tau + 3$ jets ($M_Z > 40$GeV)	AlpGEN+Herwig+JIMMY	36.2
$Z/\gamma* \to \tau\tau + 4$ jets ($M_Z > 40$GeV)	AlpGEN+Herwig+JIMMY	41.6
$Z/\gamma* \to \tau\tau + 5$ jets ($M_Z > 40$GeV)	AlpGEN+Herwig+JIMMY	46.8
$Z/\gamma* \to \tau\tau + 0$ jets ($M_Z < 40$GeV)	AlpGEN+Herwig+JIMMY	0.26
$Z/\gamma* \to \tau\tau + 1$ jet ($M_Z < 40$GeV)	AlpGEN+Herwig+JIMMY	2.83
$Z/\gamma* \to \tau\tau + 2$ jets ($M_Z < 40$GeV)	AlpGEN+Herwig+JIMMY	9.62
$Z/\gamma* \to \tau\tau + 3$ jets ($M_Z < 40$GeV)	AlpGEN+Herwig+JIMMY	14.4
$Z/\gamma* \to \tau\tau + 4$ jets ($M_Z < 40$GeV)	AlpGEN+Herwig+JIMMY	17.3
$Z/\gamma* \to \tau\tau + 5$ jets ($M_Z < 40$GeV)	AlpGEN+Herwig+JIMMY	17.4
$Z/\gamma* \to \mu\mu$ ($M_Z > 60$GeV)	Pythia	5.05
$W \to \tau\nu + 0$ jets	AlpGEN+Herwig	0.41
$W \to \tau\nu + 1$ jet	AlpGEN+Herwig	1.60
$W \to \tau\nu + 2$ jets	AlpGEN+Herwig	8.34
$W \to \tau\nu + 3$ jets	AlpGEN+Herwig	8.32
$W \to \tau\nu + 4$ jets	AlpGEN+Herwig	8.10
$W \to \tau\nu + 5$ jets	AlpGEN+Herwig	7.77
$W \to \mu\nu + 0$ jets	AlpGEN+Herwig	0.42
$W \to \mu\nu + 1$ jet	AlpGEN+Herwig	1.60
$W \to \mu\nu + 2$ jets	AlpGEN+Herwig	8.34
$W \to \mu\nu + 3$ jets	AlpGEN+Herwig	8.29
$W \to \mu\nu + 4$ jets	AlpGEN+Herwig	8.29
$W \to \mu\nu + 5$ jets	AlpGEN+Herwig	8.37
WW	Herwig	146
WZ	Herwig	45.1
ZZ	Herwig	198
ttbar	MC@NLO	165

Table 6.1: Monte Carlo samples used for signal and electroweak background, their event generators and the integrated luminosity of the samples.

Data Skimming

In order to ease the data-handling, a very loose selection is performed prior to the real analysis. This skimming is performed both on data and on the Monte Carlo samples so the number of events can be compared. The skimming cuts are:

- Passed GoodRunsList (only data)

- Passed muon trigger (EF_mu18 or EF_mu18_medium)

- At least one reconstructed muon with $p_T > 15\text{GeV}$ and within $|\eta| < 2.4$

- At least one reconstructed tau with $p_T > 10\text{GeV}$ and within $|\eta| < 2.47$ excluding $1.37 < |\eta| < 1.52$

Since all jets are reconstructed as tau candidates the last cut is extremely loose.

Pileup Reweighting

Pileup refers to multiple proton collisions in one bunch collision. The pileup is measured as the number of primary vertices in a bunch crossing and it has grown throughout 2011 ending up at an average of 12-15 vertices per bunch crossing. Pileup makes it hard to separate the detector response from different hard processes happening simultaneously.

Pileup conditions are included in the Monte Carlo simulations. To obtain the same pileup profile in Monte Carlo and data, the Monte Carlo samples are reweighted event by event. Since pileup has grown with time the different run periods in the Monte Carlo samples are used to simulate pileup conditions for different run periods. In Figure 6.1 the average number of vertices per bunch crossing for the 2011 data set and $Z \to \tau\tau + 0$ jets are shown. It is seen that a reweighting is needed to make the distributions agree.
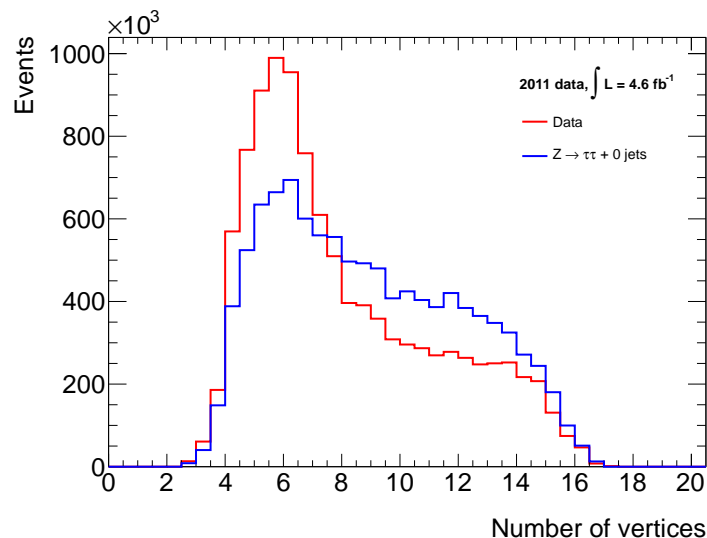
Figure 6.1: Number of vertices in data (red) and the $(Z \to \tau\tau)+0$ jets Monte Carlo sample (blue).

6.2   Event Preselection

Number of Vertices

A collision event candidate is required to have at least one reconstructed primary vertex with at least four reconstructed tracks.

Trigger

Two muon triggers are used to select the events, EF_mu18 and EF_mu18_medium. Both triggers will fire at a muon with $p_\mathrm{T} > 18\mathrm{GeV}$ at Event Filter level, but they are passed from different level 1 triggers, L1_MU10 and L1_MU11, respectively. The luminosity recorded with EF_mu18 is 1.45 fb^{-1} and 3.18 fb^{-1} with EF_mu18_medium. Both triggers are fully efficient at reconstructed muon $p_\mathrm{T} > 20\mathrm{GeV}$.

In the Monte Carlo samples weights corresponding to the fraction of luminosity taken by each trigger are applied to the samples to ensure the correct fraction of EF_mu18 and EF_mu18_medium in the results.

6.3   Object Preselection

Objects (muons, electrons, and taus) undergo a looser selection, preselection, before the final object selection to be able to perform cleaning cuts and overlap removal on the preselected objects.

Muons

Muon candidates are reconstructed using the staco algorithm described in Section 5.3. The candidates must lie within $|\eta| \leq 2.4$ and have $p_\mathrm{T} \geq 20\mathrm{GeV}$. They are required to satisfy loose selection requirements which include both standalone muons, that only leave hits in the muon spectrometer, and combined muons, that leave hits in the muon spectrometer combined with a track in the inner detector. The muon candidates must be no further away than 10 mm from the primary vertex in the longitudinal direction, $|z_0| \leq 10$ mm. The preselection cuts for muons are summarized in Table 6.2.

Electrons

Electron candidates are required to be within $|\eta| \leq 2.47$ to be within the coverage of the inner detector. The crack regions between the barrel and end-cap detectors in the electromagnetic calorimeter are avoided by requiring the electron to lie outside $1.37 < |\eta| < 1.52$. The electrons must have $p_\mathrm{T} \geq 15\mathrm{GeV}$ and must have passed the medium cut-based electron identification described in Section 5.3. The electron candidates must either be seeded by the calorimeter only or by the calorimeter and a track. The electron preselection cuts are summarized in Table 6.2.

Jets

Jets are reconstructed using the anti-k_T algorithm described in Section 5.3 with a R parameter equal to 0.4. The jets are required to have $p_\text{T} > 20\text{GeV}$.

Taus

Taus are reconstructed using the anti-k_T algorithm with a R parameter of 0.4 as described in Section 5.3. The tau candidates are required to have $p_\text{T} > 20\text{GeV}$ and lie within $|\eta| \leq 2.47$ excluding the crack region in the electromagnetic calorimeter, $1.37 < |\eta| < 1.52$. To reduce the number of electrons faking taus, the track with the highest momentum, the leading track, is required to be outside the central part of the detector, $|\eta| > 0.03$. In Table 6.2 the preselection cuts for tau candidates are summarized.

Overlap Removal

To avoid counting the same detector response as two different objects, an overlap removal between different types of objects is performed. The overlap removal defines a cone of radius $\Delta R = \sqrt{\Delta\eta^2 + \Delta\phi^2}$ around an object. If there is another type of object inside this cone, one of the objects will be removed. The overlap removal is hierarchical: it chooses muons over electron, electrons over taus and taus over jets. The cone size is 0.2 for overlap removal between muons and electrons and 0.4 for all other overlap removals. Overlap removal also removes objects of the same type overlapping leaving the preselected object with the highest p_T.

"Hole" in the Liquid Argon Calorimeter

In April 2011, a failure occurred affecting a part of the electromagnetic calorimeter. The calorimeter was repaired in June, but in the period between April and June the energy could not be measured within $0 < \eta < 1.4$ and $-0.8 < \phi < -0.6$. Since the electromagnetic calorimeter is a vital part of the measurement of missing transverse energy, an event with a preselected jet, tau or electron within the affected area will be removed. The liquid argon calorimeter "hole" is also taken into account in the Monte Carlo samples where a luminosity weight is used to identify the amount of data affected by the "hole".

Jet Cleaning

There is a very small probability that signals from cosmic rays or noise in the calorimeter electronics can be reconstructed as jets. To avoid this, quality cuts are imposed on the reconstructed jets and taus. If a reconstructed jet/tau fails the cuts the entire event is rejected. The cuts used for jet/tau cleaning are the recommended cuts from the Tau Working Group in ATLAS, see Appendix A.1. The cuts are applied to all reconstructed jets and taus with $p_\text{T} > 20\text{GeV}$ and $|\eta| < 2.5$.

Event Selection Based on Preselected Objects

The events are required to have at least one preselected muon and one preselected tau after overlap removal.

6.4   Object Selection

After overlap removal has been performed on preselected objects, a further and tighter selection of physics objects is done. All objects are required to have passed the preselection requirements.

Muons

All muons are required to have passed the preselection cuts. Muon candidates are required to have hits in the muon spectrometer combined with a track in the inner detector. The distance from the muon to the primary vertex, $|d_0|$, must be smaller than 10 mm. Track quality cuts are applied to clean the track of the muon candidate. The track quality cuts are cuts on number of hits in different parts of the inner detector and are described in detail in appendix A.2. The final object selection cuts are summarized in Table 6.2.

Electrons

All electrons must have passed the preselection. The only extra cut in the final object selection for electrons is to require the tight cut-based electron identification as described in Section 5.3.

Jets

Jets are restricted to be within the coverage of the hadronic calorimeter, $|\eta| < 4.5$.

Taus

All taus must have passed the preselection cuts. Tau candidates are required to have one or three tracks and unit charge. To suppress jet contamination, a tight cut on the boosted decision tree (BDT) discrimination variable is required as describe in Section 5.3. The electron contamination is restricted by a medium electron veto using boosted decision tree (BDT) and a cut-based muon veto is applied. A summary of the final selection for tau candidates is given in Table 6.2. If more than one tau pass the cuts, the tau with the highest p_T will be used in the study of tau polarization.

6.5   Muon Isolation

Muons from semileptonic $Z \to \tau\tau$ decays are expected to be isolated with no energy deposits around the track and only one track. Since muon candidates in QCD multijet background are expected to be near jets, isolation criteria are applied on the muon to reduce the number of multijet background events.

In muon isolation cuts, cones of size $\Delta R = \sqrt{\Delta\eta^2 + \Delta\phi^2}$ are investigated for energy deposits not caused by the muon and number of tracks within the cone. The cuts are

- $E_T \mathrm{cone}/p_T < 0.04$ within a cone of radius $\Delta R = 0.2$

- No other track within a cone of radius $\Delta R = 0.4$

	Preselection	Selection
Muon	Loose $p_T^\mu \geq 20$ GeV $\|\eta\| \leq 2.4$s $\|z_0\| \leq 10$ mm	Muon is Combined $\|d_0\| < 10$ mm Track quality cuts
Electron	Medium $p_T^e \geq 15$ GeV $\|\eta\| \leq 2.47$, excluding $1.37 < \|\eta\| < 1.52$	Tight
Jet	$p_T^{\text{jet}} \geq 20$ GeV	$\|\eta\| < 4.5$
Tau	$p_T^\tau \geq 20$ GeV $\|\eta\| \leq 2.47$, excluding $1.37 < \|\eta\| < 1.52$ Leading Track $\|\eta\| > 0.03$	Tau ID BDT Tight 1 or 3 tracks Unit charge Electron veto BDT Medium Muon veto

Table 6.2: Object preselection and selection cuts. Objects are required to have passed both the preselection and the selection cuts.

where $E_T$cone is the sum of transverse energy in the calorimeter within the cone (corrected for the energy deposited by the muon) and p_T is the transverse momentum of the muon The transverse energy investigated is the original transverse energy subtracted the energy of the muon.

6.6 Event Selection

In the event selection, properties in the entire event of all the objects are investigated. The objects are required to have passed the full object preselection and selection.

Event Selection Based on Selected Objects and Muon Isolation

An event must fulfill the following requirements on the number of selected objects:

- At least one selected and isolated muon

- At least one selected tau

Events not passing the object selection cuts are rejected.

Opposite Sign Charge

Since the hadronic tau and the muon will originate from a electrically neutral particle they must have opposite electrical charge.

Dilepton Veto

A veto on preselected electrons and more than one preselected muon is therefore applied after the opposite sign charge requirement. This will reduce the $Z(\to \mu\mu)$ + jets back-

ground sufficiently since there will most likely be two preselected muons. In Figure 6.2 it is seen that there are very few signal events with more than one preselected lepton.
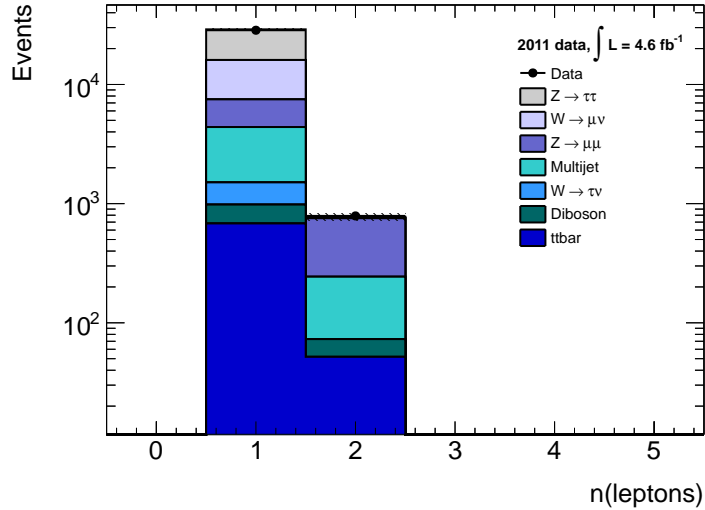
Figure 6.2: Number of preselected muons and electrons after object selection cuts and opposite sign charge cut.

W Suppression Cuts

In order to reduce the number of $W(\to \mu\nu)$ + jets and $W(\to \tau\nu)$ + jets that pass the selection two cuts are applied.

Since the mass of the Z is much larger than the mass of the τ lepton, the taus will be highly boosted and the neutrinos originating from their decay will be highly collinear with the tau direction. If the Z is not boosted in the transverse plane, the muon and the tau will lie back-to-back and the missing transverse energy caused by the neutrinos will lie either in the direction of the muon or the tau. If the Z is boosted in the transverse plane, the E_T^{miss} will lie in the narrow angle between the muon and the tau as shown in Figure 6.3 (a). In W + jets events the missing E_T will lie in the wide angle between the muon and the jet faking a tau as shown in Figures 6.3 (b) and (c).

The angles between the missing E_T and the tau candidate and the missing E_T and the muon can thus be used as a discriminator for W + jets background. The angles are combined into the variable

$$\Sigma \cos \Delta\phi = \cos\left(\phi\left(\mu\right) - \phi\left(E_T^{\mathrm{miss}}\right)\right) + \cos\left(\phi\left(\tau_h\right) - \phi\left(E_T^{\mathrm{miss}}\right)\right) \tag{6.1}$$

It is seen that for transversely boosted $Z \to \tau\tau$ events $\Sigma \cos \Delta\phi$ will be positive, and it will be zero when the muon and tau are back-to-back. In W + jets events $\Sigma \cos \Delta\phi$ will be negative. A cut of $\Sigma \cos \Delta\phi > -0.15$ is therefore applied. The $\Sigma \cos \Delta\phi$ distribution is shown in Figure 6.4 (a).
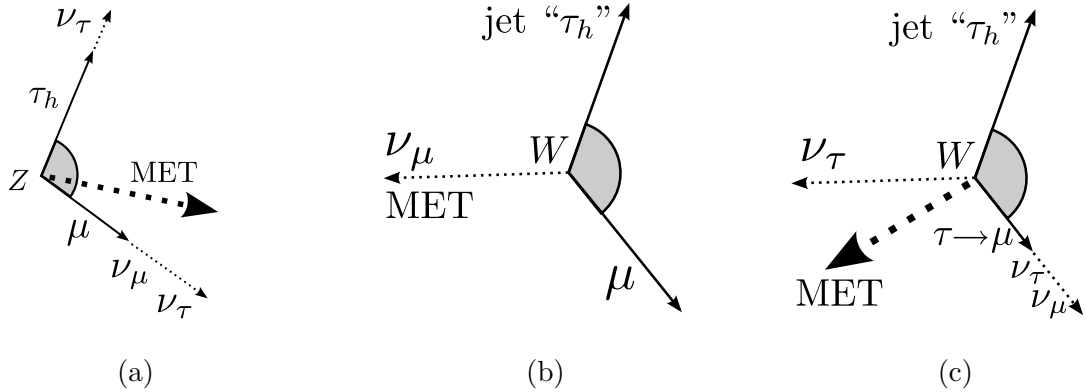
Figure 6.3: Position of Missing E_T in $Z \to \tau\tau$ (a), $W \to \mu\nu$ (b), and $W \to \tau\nu$ (c) events. Courtesy of Ryan Reece.

The other W suppression cut is on the transverse mass of the muon and the $E_\mathrm{T}^\mathrm{miss}$, m_T, given by

$$m_\mathrm{T}(\mu, E_\mathrm{T}^\mathrm{miss}) = \sqrt{2p_\mathrm{T}^\mu E_\mathrm{T}^\mathrm{miss} \cdot \left(1 - \cos\left(\phi\left(\mu\right) - \phi\left(E_\mathrm{T}^\mathrm{miss}\right)\right)\right)} \qquad (6.2)$$

which must be above 50 GeV. The transverse mass distribution is shown in Figure 6.4 (b).

The events are required to pass both the cut on $\Sigma\cos\Delta\phi$ and the m_T.
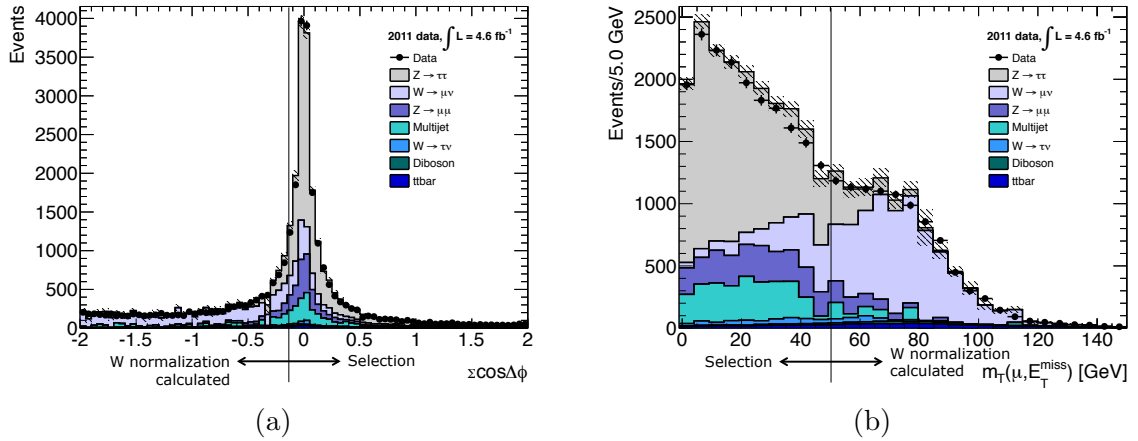
Figure 6.4: $\Sigma\cos\Delta\phi$ (a) and the transverse mass of the muon and missing transverse energy (b) after all prior cuts. The vertical lines describe the regions for selection and the control regions for W + jets normalization.

Visible Mass

A cut on the invariant mass of the selected muon and tau, the visible mass, is performed to reduce events coming from $Z \to \mu\mu$ and multijet QCD background. The visible mass

is used due to the amount of neutrinos in the signal final state. The visible mass window used for selection is $35\text{GeV} < m_{\text{vis}}(\mu, \tau_h) < 75\text{GeV}$.
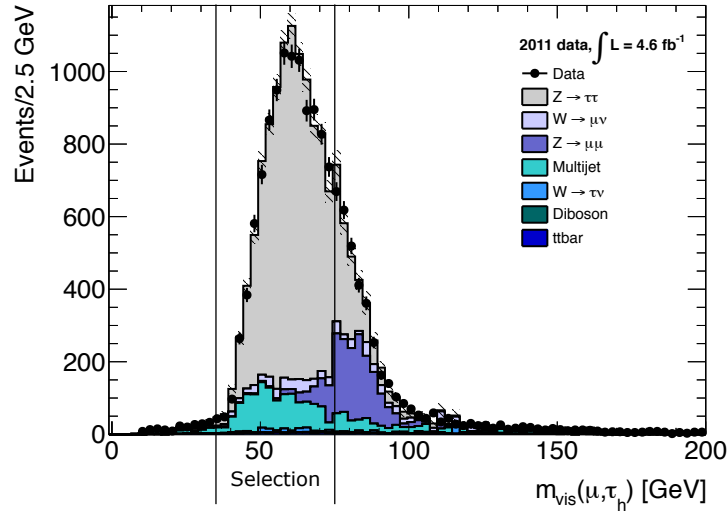
Figure 6.5: Visible mass of the isolated muon and the hadronic tau after all prior cuts. The vertical line indicate the selection cut.

Number of Tracks

In the measurement of the polarization only object selected taus with one track is as described in Section 3.5. This cut is not part of the event selection in the $Z \to \tau\tau$ cross section measurement at ATLAS[39]. In Figure 6.6 the number of tracks for the hadronic decaying tau is shown. A good agreement in tau track multiplicity is seen between data and Monte Carlo.

6.7 Background Estimation

The number of background events passing the selection is estimated in two ways, with Monte Carlo samples, and with data-driven methods. In general the electroweak background is estimated from Monte Carlo samples, but some samples need further normalization to data. The multijet QCD background is estimated completely from data using the "ABCD"-method.

Electroweak Background

The electroweak backgrounds completely estimated from Monte Carlo are the diboson (WW, WZ, and ZZ) background and the top pair background. They are used without any other scale than a luminosity scale found from the luminosity in the samples.
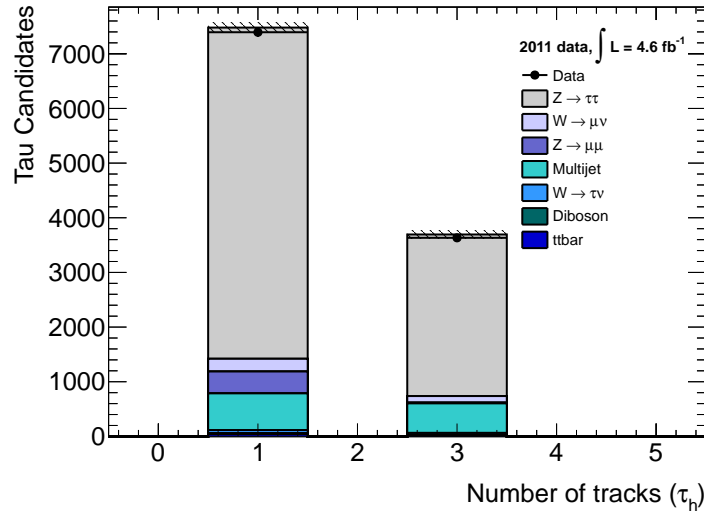
Figure 6.6: Track multiplicity for tau candidates after all event selection cuts.

Though, for the standard event selection, opposite sign charge of the muon and the tau is required, here a study is presented of the W + jets background both for opposite sign (OS) and for the same sign (SS) case. This will be needed for the estimation of the multijet background.

The W + jets background needs a further normalization since the rate of jets faking taus is not well described in Monte Carlo. The normalization factor for W + jets is different for regions with opposite and same sign charge of the muon and the hadronically decaying tau, because quark jets will primarily be biased towards the opposite sign charge region while gluon jets will be equally distributed between opposite and same sign charge regions. The quark jets have a higher probability of faking a tau than a gluon jet and the normalization factors are therefore different in the opposite sign charge and same sign charge regions.

The scale factors are measured by investigating the number of events passing all cuts prior to the W suppression cuts and both W suppression cuts reversed. The scale factors for the W + jets background are found to be

$$
\begin{aligned}
k_W^{\mathrm{OS}} &= 0.604 \pm 0.008 \\
k_W^{\mathrm{SS}} &= 0.720 \pm 0.017
\end{aligned}
$$

The W + jets background is scaled with this factor and a luminosity scale. In all figures in Section 6.6, the W + jets background is scaled.

As the rate of jets faking taus in W + jets backgrounds is not well described, it is investigated whether it is the same for $Z(\to \mu\mu)$ + jets background. The scale factor is only measured in the opposite charge region. The selection requirements used to measure the Z + jets normalization factor is two muons, W suppression cuts, selected tau, one isolated muon, and $66\mathrm{GeV} < m_{\mu\mu} < 116\mathrm{GeV}$. The normalization factor for Z + jets is found to be consistent with one and the Z + jets background will therefore not be scaled with anything else, but the luminosity weight.

Multijet Background

The multijet QCD background is not well modeled in Monte Carlo and furthermore the cross section for QCD is very high compared to the electroweak processes. A completely data-driven method is therefore used to estimate the amount and shape of the QCD background passing the selection cuts.

The multijet background is estimated with the entirely data-driven method known as the "ABCD"-method[41]. Data is divided into four regions, one signal dominated region and three background dominated regions. The division is defined by two criteria: isolated/non-isolated muon and opposite/same sign charge. The signal region (A) has an isolated muon and opposite sign charge, the other regions (B, C, and D) have the other three combinations, as shown in Figure 6.7.
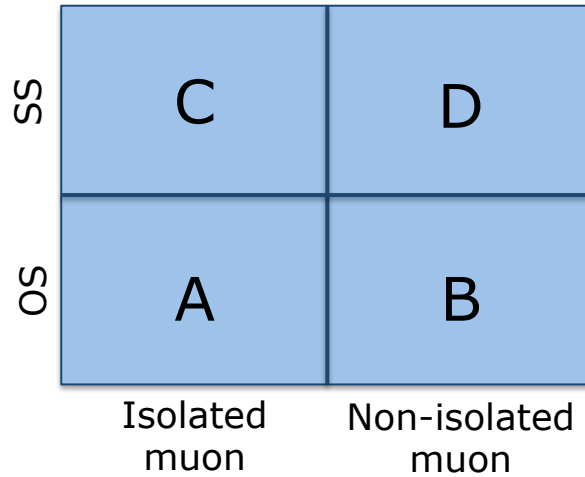
Figure 6.7: Regions for the "ABCD"-method. OS/SS stands for opposite/same sign charge.

The assumptions required by the "ABCD"-method are:

- There are enough events in region B, C, and D to propagate the statistical uncertainty linearly to region A.

- The cuts applied (muon isolation and charge product) are uncorrelated.

- Region B, C, and D (muon anti-isolation cuts) consist almost entirely of QCD multijet background. If there are other background sources (electroweak), it will be subtracted prior to the determination of number of multijet events in region A.

The number of multijet events in the signal region A is given by

$$N_A^{\text{QCD}} = \frac{N_B^{\text{QCD}}}{N_D^{\text{QCD}}} \cdot N_C^{\text{QCD}} \tag{6.3}$$

where $N_i^{\mathrm{QCD}} = N_i^{\mathrm{data}} - N_i^{\mathrm{MC_{EW}}}$, and $\mathrm{MC_{EW}}$ is the electroweak Monte Carlo samples including both signal and background.

The shape of QCD background is assumed to be the same in opposite sign and same sign regions for all variables. The shape is thus found from region C.

In all the figures in Section 6.6, the multijet background is estimated using the number of QCD events from the "ABCD" method and the shape from region C. A good agreement is observed between the expected and observed number of events in all variables.

6.8 Summary of $Z \to \tau\tau$ Selection

In Table 6.3, a summary of number of events passing the selection are listed. After background normalization, a good agreement is seen between expected and observed number events. The $Z \to \tau\tau$ cross section is thus as expected.

In Figures 6.8 and 6.9, kinematic variables of the tau, the muon and the missing transverse energy of events passing the entire event selection except the cut on track multiplicity of taus are shown. A good agreement between both the number and the shape of expected and observed events are seen of all variables after the selection.

Through the event selection, Figures 6.2 to 6.5 have also shown good agreement of the shape of all variables used in the selection.

Cut	Data	$Z \rightarrow \tau\tau$	$Z \rightarrow \mu\mu$	$W \rightarrow \tau\nu_\tau$
Trigger + Skimming	$153.84 \cdot 10^6 \pm 12.4 \cdot 10^3$	$210.3 \cdot 10^3 \pm 0.4 \cdot 10^3$	$1.983 \cdot 10^6 \pm 2 \cdot 10^3$	$477.0 \cdot 10^3 \pm 2.2 \cdot 10^3$
Object Selection	35917 ± 190	13127 ± 106	4375 ± 92	617 ± 42
Opposite Sign Charge	29312 ± 171	12967 ± 171	3617 ± 85	526 ± 41
Dilepton Veto	28519 ± 169	12953 ± 105	3106 ± 82	526 ± 41
W cuts	14703 ± 121	10560 ± 96	1892 ± 68	193 ± 22
$35\text{GeV} < m_{\text{vis}} < 75\text{GeV}$	10244 ± 101	8679 ± 88	386 ± 29	89 ± 13
One track taus	6857 ± 83	5832 ± 71	372 ± 29	56 ± 10
(Polarization measurement only)				

Cut	$W \rightarrow \mu\nu_\mu$	Multijet	Diboson	ttbar
Trigger + Skimming	$7.302 \cdot 10^6 \pm 8.718 \cdot 10^3$	-	33244 ± 63	91628 ± 90
Object Selection	11074 ± 211	-	394 ± 7	831 ± 9
Opposite Sign Charge	8563 ± 161	3953 ± 217	322 ± 6	735 ± 8
Dilepton Veto	8555 ± 161	3243 ± 214	300 ± 5	682 ± 8
W cuts	839 ± 41	1873 ± 66	57 ± 3	156 ± 4
$35\text{GeV} < m_{\text{vis}} < 75\text{GeV}$	338 ± 24	1166 ± 51	27 ± 2	56 ± 2
One track taus	224 ± 19	616 ± 36	20 ± 2	37 ± 2
(Polarization measurement only)				

Table 6.3: Cut flow summary
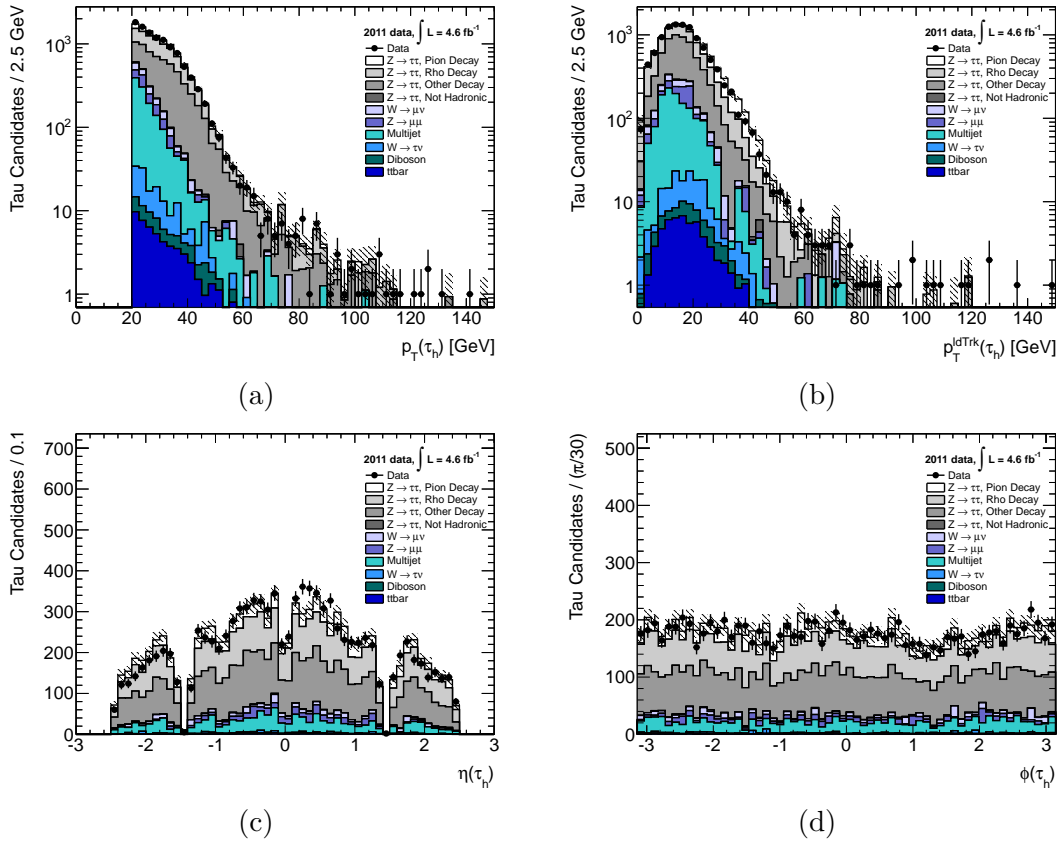
Figure 6.8: Distribution of transverse momentum (a), p_T of leading track (b), pseudo-rapidity (c), and azimuthal angle (d) of taus passing the selection.
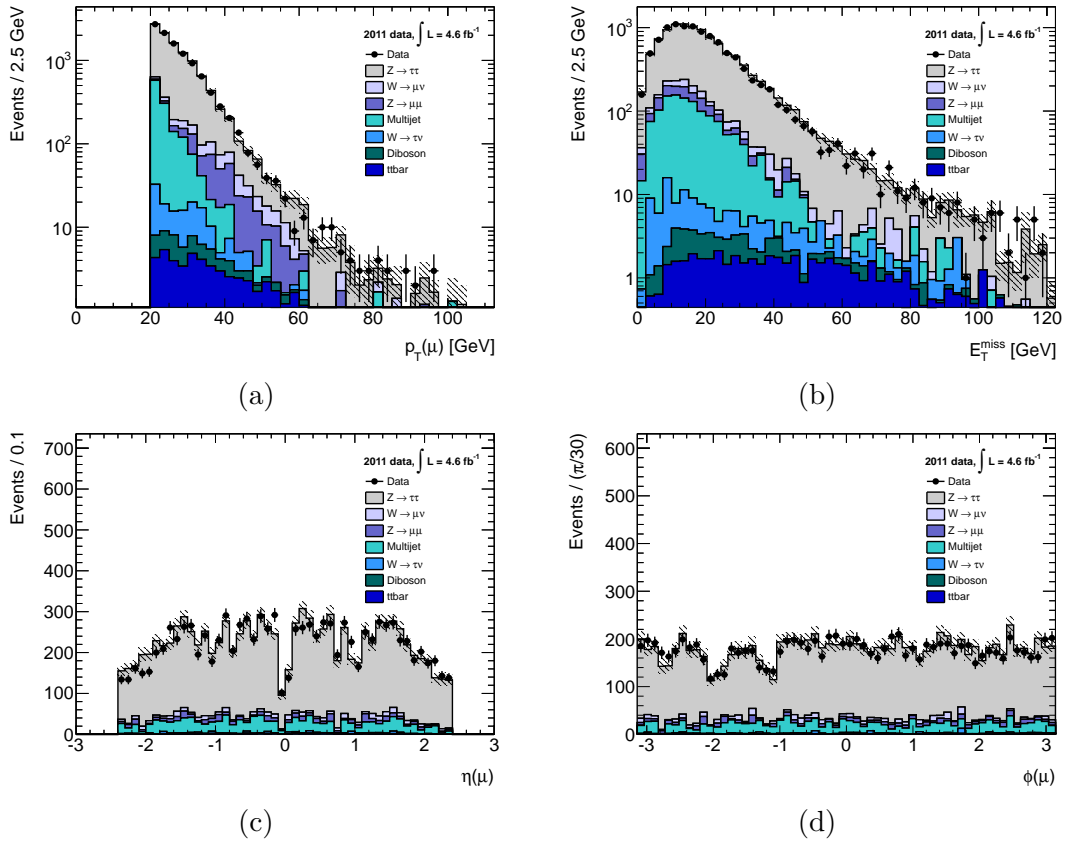
Figure 6.9: Distribution of muon p_{T} (a), $E_{\mathrm{T}}^{\mathrm{miss}}$ (b), pseudo-rapidity of the muon (c), and azimuthal angle of the muon (d) of events passing the selection.

7

Tau Helicity in Monte Carlo Samples

Knowledge of the true tau helicity in the Monte Carlo simulations is a vital part in the extraction of the tau polarization result from real data. Very unfortunate, the tau helicity was not saved in the ATLAS Monte Carlo simulations. This chapter will describe how the tau helicity is re-established. Also studies of the detector smearing and the event selection on the tau polarization are presented.

7.1 Re-establishing the Tau Helicity Event-by-Event in Monte Carlo

In the ATLAS simulation, tau decays are handled by TAUOLA[29], which assigns helicity to the taus and decays them accordingly. In this process, unfortunately, the tau helicity was not saved and thus it is not available in the data stream.

Tau Helicity in TAUOLA

In the ATLAS Monte Carlo samples the spin effects are simulated using TAUOLA[29], which calculates weights for the tau pairs according to their kinematics. The weights are given as

$$w = \tfrac{1}{4} \sum_{i,j=0}^{4} h_i^+ h_j^- R_{ij} \tag{7.1}$$

where h^+ and h^- are the so-called polarimeter vectors for the τ^+ and τ^- decays, respectively, and the matrix R_{ij} describing the spin orientation of the system, in the case of a Z decay, takes the form

$$R = \begin{pmatrix} 1 & 0 & 0 & -P_\tau \\ 0 & 0 & 0 & 0 \\ 0 & 0 & 0 & 0 \\ -P_\tau & 0 & 0 & 1 \end{pmatrix} \tag{7.2}$$

Here P_τ is the tau polarization given by Equation 3.10. Equations 7.1 and 7.2 are expressed in the rest frame of the Z with the z-axis in the direction of flight of the τ^-. By inserting Equation 7.2 into Equation 7.1 one obtains

$$w = \tfrac{1}{4} \left[1 + h_z^+ h_z^- - P_\tau \left(h_z^+ + h_z^- \right) \right] \tag{7.3}$$

where we have used, that $h_0^+ = h_0^- = 0$. It is seen, that only the z-component of the polarimeter vectors appear in the expression for w: The event weight thus only depends on the longitudinal part of the polarization.

The polarimeter vectors, h, contain information on the helicity dependent part of the kinematics of tau decays, and thus the variables described in Section 3.4. In $\tau^- \to \pi^- \nu_\tau$ decays, for example, the z-component is $h_z = \cos\theta$, c.f Equation 3.13.

It is decided whether a tau pair is saved by generating a random number between 0 and 1. If the weight, w, is greater than the random number the tau pair if saved. If on the other hand w is smaller than the random number the tau pair is rejected and the tau pair must be regenerated.

Method for Extracting the Tau Helicity

The tau helicity in a sample decayed with spin effects can be re-established using reverse engineering[14]. We do not know the truth tau polarization, but we know the polarimetric vectors h^+ and h^- from the tau pair since they only depend on kinematics of the tau pair. From h^+ and h^- we can find the probability that the τ^- is left-handed or right-handed.

When studying the tau helicity event-by-event, the polarization in Equation 7.3 is substituted with the helicity, λ_τ, that can either be $+1$ or -1 for right-handed and left-handed τ^-, respectively. Using the tau helicity, two weights can be generated from Equation 7.3:

$$
\begin{aligned}
w_{\mathrm{R}} &= \tfrac{1}{4}\left[1 + h_z^+ h_z^- - (h_z^+ + h_z^-)\right] \\
w_{\mathrm{L}} &= \tfrac{1}{4}\left[1 + h_z^+ h_z^- + (h_z^+ + h_z^-)\right]
\end{aligned}
\tag{7.4}
$$

The polarimeter vectors, h, are calculated with TauSpinner[42] that uses the same algorithm as TAUOLA.

With the two weight, w_{R} and w_{L}, one could assign the spin-configuration event-by-event in an unpolarized sample by comparing the probability of the τ^- to be right-handed given by

$$
p_{\tau_R^- \tau_L^+} = \frac{w_{\mathrm{R}}}{w_{\mathrm{R}} + w_{\mathrm{L}}}
\tag{7.5}
$$

to a random number between 0 and 1. If $p_{\tau_R^- \tau_L^+}$ is greater than the random number, the event will be assigned with the $\tau_R^- \tau_L^+$ spin-configuration. Otherwise it will be assigned the $\tau_L^- \tau_R^+$ spin-configuration.

If the sample is polarized, as in the case of Z decays, the probability, $p_{\tau_R^- \tau_L^+}$ will instead be given by

$$
p_{\tau_R^- \tau_L^+} = \frac{(1 + \Pi)\, w_{\mathrm{R}}}{(1 + \Pi)\, w_{\mathrm{R}} + (1 - \Pi)\, w_{\mathrm{L}}}
\tag{7.6}
$$

where Π is the average tau polarization of the sample. Information of the average polarization of the Z in the sample is thus required.

The Π depends both on center of mass energy and scattering angle of the Z, as seen in Figure 7.1. Figure 7.1 (a) and (b) are made analytically from the expression in Equation 3.10. The contributions from up-type quarks and down-type quarks are taken to be 50% each in Figure 7.1. Even though there are two u valence quarks in the proton, the stronger coupling of the Z to the down-type quarks will to some extend even out the contributions.

(a)

(b)
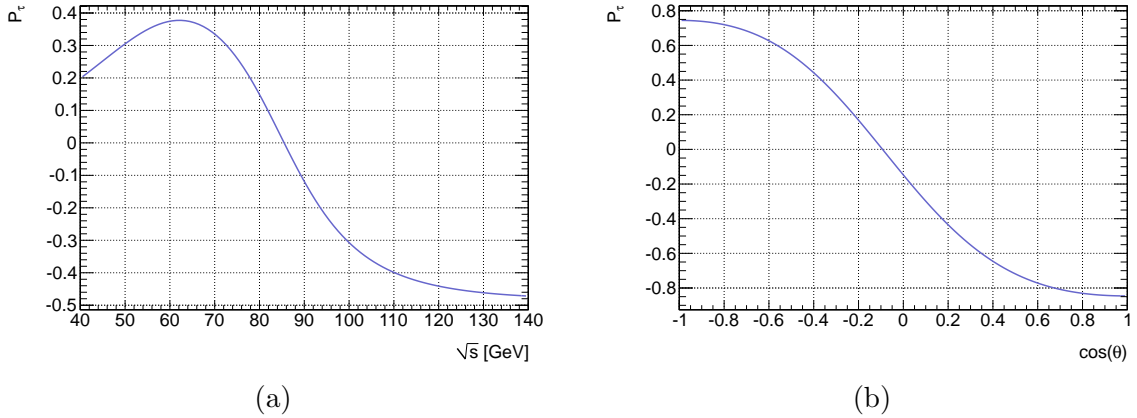
Figure 7.1: Tau polarization dependence on the center of mass energy taken at $\cos\theta^* = 0$ (a) and the scattering angle (b).

Due to the strong dependence of the tau polarization on the $\sqrt{s}$ and $\cos\theta^*$, it is not sufficient to know the overall polarization of the sample, but one must estimate the dependencies of Π on the center of mass energy and the scattering angle.

Estimating $\Pi(s, \cos\theta^*)$ in Monte Carlo

As discussed, it is necessary to estimate the average tau polarization as a function of s and $\cos\theta^*$, $\Pi(s, \cos\theta^*)$ from the Monte Carlo sample. $\Pi(s, \cos\theta^*)$ is used as an input in Equation 7.6.

Due to the dependence of Π on the scattering angle, θ^*, it is necessary to know the angle in the simulations. Information on the incoming quarks creating the Z boson is not available in the ATLAS simulations and it is therefore not possible to calculate θ^* directly. It is therefore assumed that the incoming quarks move along the beam axis, and from this the scattering angle can be calculated. Instead of using the approximate scattering angle, the pseudo-rapidity is used in the angle dependence study.

Event by event, the polarimeter vectors, h^+ and h^-, are calculated from the kinematics of the tau decays at truth level using TauSpinner. From the polarimeter vectors, w_{R} and w_{L} are calculated using Equation 7.4 and an asymmetry, A_w, is constructed from the calculated weights. The asymmetry is given as

$$A_w = \frac{w_{\mathrm{R}} - w_{\mathrm{L}}}{w_{\mathrm{R}} + w_{\mathrm{L}}} \tag{7.7}$$

All the calculations are done in bins of $\sqrt{s}$ and η to determine the energy and scattering angle dependence on Π. Distributions of A_w for different energy and scattering angle ranges are created. In Figure 7.2, the A_w distribution from the Monte Carlo sample of study is shown in the energy range around the Z peak ($90\mathrm{GeV} < \sqrt{s} < 92\mathrm{GeV}$) and for all θ^*.
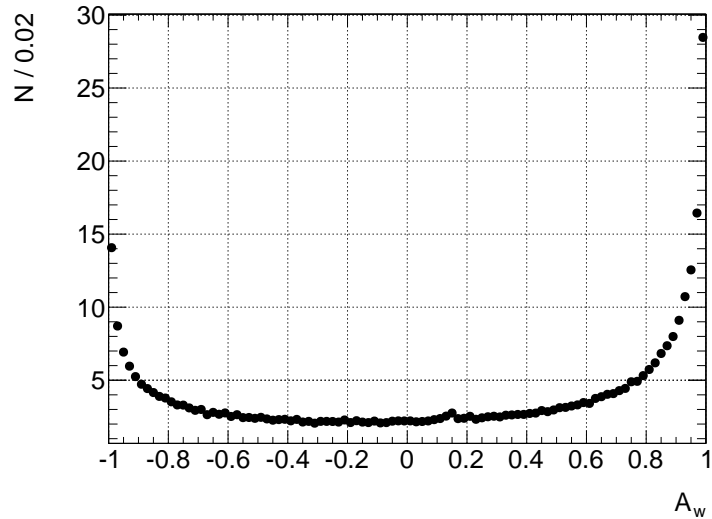
Figure 7.2: A_w from the ATLAS $Z \to \tau\tau$ Monte Carlo sample in the energy range $90\text{GeV} <$ $\sqrt{s} < 92\text{GeV}$ and for all θ^*. The distribution is normalized to 1 pb^{-1}.

To be able to measure Π in ATLAS $Z \to \tau\tau$ Monte Carlo samples, distributions of A_w for right-handed and left-handed τ^- are created in a Pythia and TAUOLA standalone[1] run where the helicity information of the taus is accessible. The standalone run used the same configuration of input parameters as was used for the production of the Monte Carlo samples under study. The A_w distributions for right-handed and left-handed τ^- from Pythia+TAUOLA are shown in Figure 7.3.

Π is measured by fitting the A_w distributions from the Monte Carlo samples of study with the sum of the A_w for right-handed and left-handed τ^- created with Pythia and TAUOLA.

The fitting was done using χ^2 fit.

To determine the tau polarization as a function of the center of mass energy, the Monte Carlo samples are divided into mass bins. The mass bins vary in size and are smallest around the Z peak where we wish to study the dependence in detail.

In Figure 7.4 the extracted tau polarization dependence on center of mass energy and pseudo-rapidity is seen. Compared to Figure 7.1 (b) the dependence on η is very weak. Since the initial state is symmetric in proton-proton collisions, the sign of the approximated θ^* is not meaningful and the θ^* dependence is somewhat evened out. By noting the different vertical scales between the two plots, it is seen that the pseudo-rapidity dependence is very weak compared to the dependence on center of mass. Hence, for the event-by-event assignment of spin-configurations according to Equation 7.6, the $\cos\theta^*$ dependence of Π has been ignored.

---

[1]The ATLAS software was not used in this process.
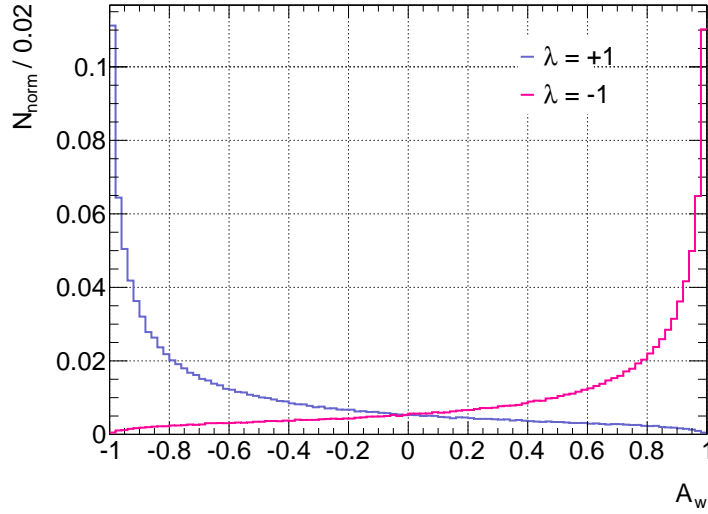
Figure 7.3: A_w for right-handed (blue) and left-handed (pink) τ^- created with Pythia and TAUOLA. Both distributions are normalized to unity.
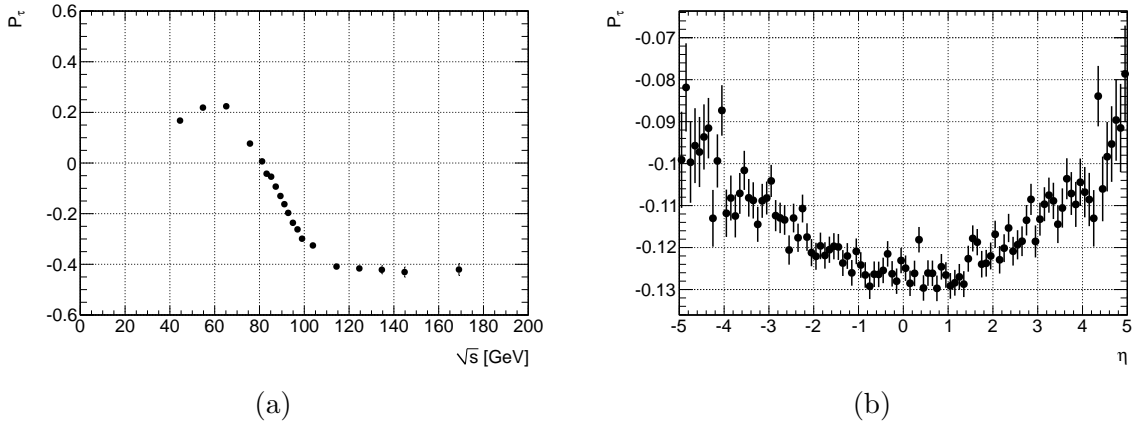
Figure 7.4: Extracted tau polarization values in the ATLAS $Z \to \tau\tau$ Monte Carlo samples as a function of center of mass energy (a) and pseudo-rapidity, η, (b).

The mass dependence observed in Figure 7.4 (a) is fitted to the function

$$\Pi(s) = \frac{A\left(1 - M_Z^2/s\right) + B}{\left(1 - M_Z^2/s\right)^2 + C\left(1 - M_Z^2/s\right) + D} \tag{7.8}$$

where A, B, C, and D are fit parameters. The functional form is inspired by Equation 3.7 for $\cos\theta^* = 0$ and ignoring the α dependence on $\sqrt{s}$.

The result of the fit can be seen in Figure 7.5 and in Table 7.1. It is seen that the fit is not good for energies above 120 GeV.

Comparing Figures 7.1 (a) and 7.5 it is seen that the polarization is lower for low center of mass energy in the measured sample than in the theoretical. This might be because the energy plotted is not the true energy, but reconstructed from the two taus.

Fitting Parameter	Value
A	-0.673 ± 0.013
B	-0.169 ± 0.005
C	-0.283 ± 0.026
D	1.012 ± 0.029

Table 7.1: Fitting parameters for the mass dependence fit.

If a tau has radiated a photon, the energy will be underestimated. The underestimation of the center of mass energy might affect the low energy region the most due to the large amount of events near the Z peak compared to the number of events with low energy.

Since the cross section of the Monte Carlo sample is dominated by the Z peak ($\sqrt{s} \sim$ 90GeV), most of the selected events will be at that energy. It is therefore important that $\Pi(s)$ describes the energy range around the Z peak well. As seen in Figure 7.5, the extracted tau polarization and $\Pi(s)$ agree around the Z peak.
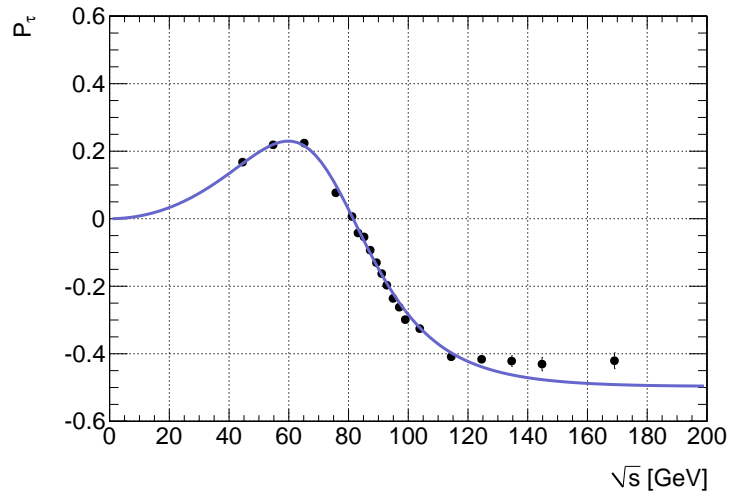
Figure 7.5: Tau polarization as a function of $\sqrt{s}$ fitted with Equation 7.8.

Samples	N_{tot}	N_L	N_R	Polarization
$Z \to \tau\tau + 0$ jets	3123597	1751102	1372495	-0.1212 ± 0.0006
$Z \to \tau\tau + 1$ jet	323746	182168	141578	-0.1254 ± 0.0017
$Z \to \tau\tau + 2$ jets	902192	501041	401151	-0.1107 ± 0.0010
$Z \to \tau\tau + 3$ jets	483736	267525	216211	-0.1061 ± 0.0014
$Z \to \tau\tau + 4$ jets	144706	79859	64847	-0.1037 ± 0.0026
$Z \to \tau\tau + 5$ jets	44925	24682	20243	-0.0988 ± 0.0047

Table 7.2: Number of $\tau_L^- \tau_R^+$ pairs (N_L), $\tau_R^- \tau_L^+$ pairs (N_R), and the polarization in a fraction of the signal Monte Carlo samples used in this thesis.

Results

The tau helicity is re-established using the method described in this section with an average tau polarization of the Z boson given by Equation 7.8 with parameters given in Table 7.1.

Due to a non-understood technical problem, for a small fraction of events (about 0.5%) the truth information on the tau decay products was not available in the data stream. These events have been ignored in the study.[2]

In Table 7.2 the number of right-handed τ^- (N_R) and left-handed τ^- (N_L) are listed for each of the signal Monte Carlo samples. The tau polarization is calculated as

$$P_\tau = \frac{N_R - N_L}{N_R + N_L} \tag{7.9}$$

and the uncertainty is found using error propagation and is given by

$$\sigma_{P_\tau} = 2\sqrt{\frac{N_R N_L}{(N_R + N_L)^3}} \tag{7.10}$$

As seen in Table 7.2, the tau polarization is varying between the samples. The combined, luminosity weighted polarization from all the Monte Carlo samples is $P_\tau = -0.1211 \pm 0.0005$.

In Figure 7.6 the visible energy fraction for different types of tau decays are shown. It is clear from especially Figure 7.6(a) that the helicity re-establishing method has worked well since the positive and negative helicity samples should follow, as we recall from Section 3.4, $\frac{1}{2}x$ and $\frac{1}{2}(1-x)$ respectively. Compared to the distributions in Figures 3.7 and 3.10 created with a Pythia and TAUOLA standalone run, it is seen that distributions in Figure 7.6 are indeed very similar.

---

[2]Some taus are not decayed properly in Monte Carlo and have no decay products. If a tau do not have any decay products, the weights in Equation 7.4 cannot be calculated and a tau helicity cannot be re-established. The helicity is in this case put equal to zero and will not be used in measurement of the tau polarization.
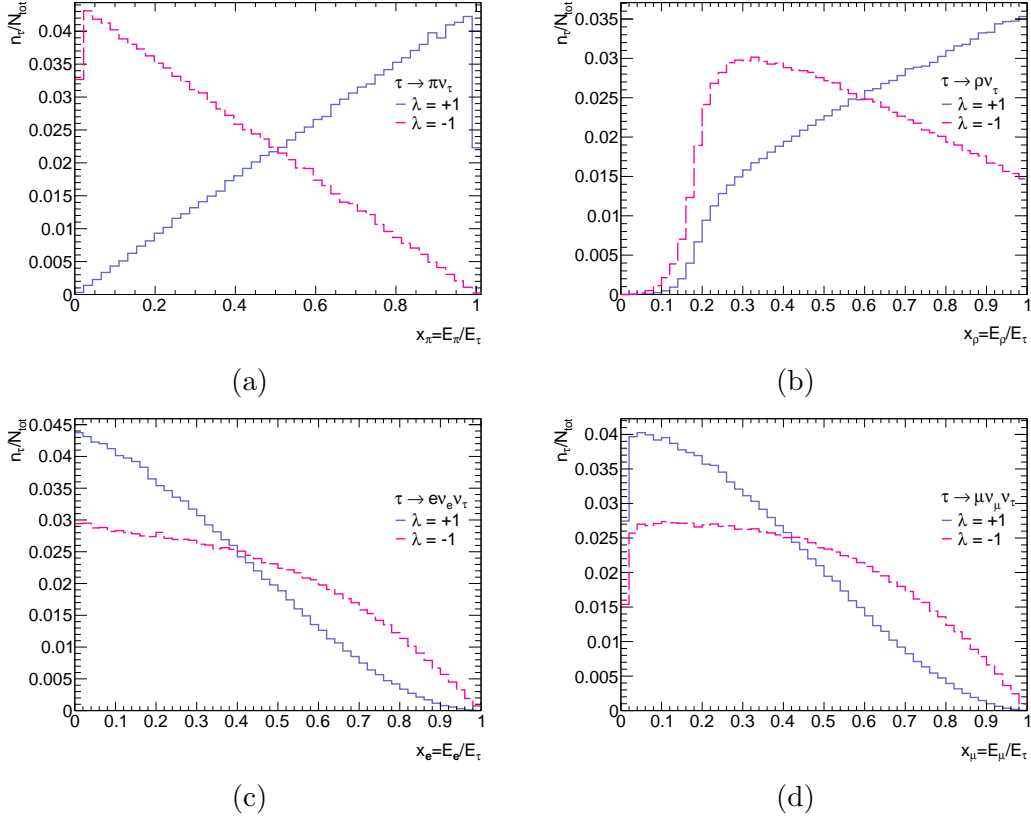
Figure 7.6: The visible energy fraction for pion (a), rho (b), electron (c), and muon (d) decays of tau divided into $\tau_R^- \tau_L^+$ pairs (blue) and $\tau_R^+ \tau_L^-$ pairs (pink). Both samples are normalized to one.

7.2   Detector Effects on the Tau Helicity

To measure the tau polarization the charged energy asymmetry is used. The energies used to calculate the charged energy asymmetry, Υ, defined in Equation 3.24 are not directly accessible in the data since the energy of the neutral pions is not reconstructed. Instead the total transverse calorimeter energy, E_T, and the transverse momentum of the charged tracks, p_T^Trk, are used. Υ is studied for taus with one track, one prong taus. The charged energy asymmetry is given in terms of observables as

$$\Upsilon = \frac{p_\text{T}^\text{Trk} - \left(E_\text{T} - p_\text{T}^\text{Trk}\right)}{p_\text{T}^\text{Trk} + \left(E_\text{T} - p_\text{T}^\text{Trk}\right)} = \frac{2p_\text{T}^\text{Trk}}{E_\text{T}} - 1 \tag{7.11}$$

since the energy of the neutral pions will be given by $E_\text{T}^{\pi^0} = E_\text{T} - p_\text{T}^\text{Trk}$.

However, the reconstructed Υ will differ from the truth Υ due to detector effects. The correlation between truth and reconstructed Υ is shown in Figure 7.7. The correlation factor is calculated to be 0.872 meaning that the reconstructed charged energy fraction corresponds well to the truth.
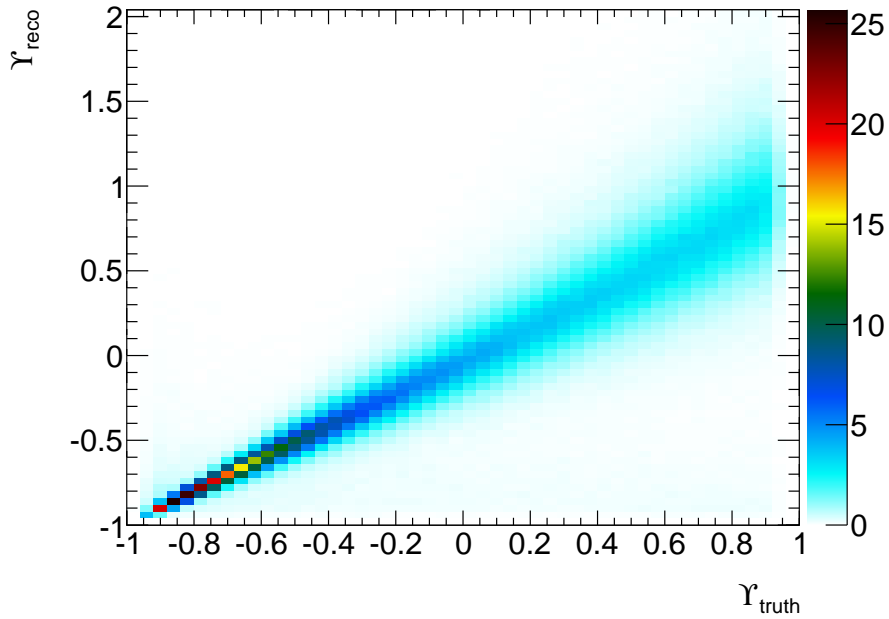
Figure 7.7: Correlation between truth and reconstructed charged energy asymmetry for truthmatched taus decaying to rhos.

The smearing of the energies by the detector will affect the separation between right-handed and left-handed τ^- in the charged energy asymmetry distribution. The sensitivity loss is estimated by comparing the sensitivity of truth taus to the sensitivity os truth-matched, reconstructed taus. Reconstructed taus are truthmatched if they are within a cone of radius $\Delta R = \sqrt{\Delta \eta^2 + \Delta \phi^2} = 0.4$ of a true tau.

(a)   (b)
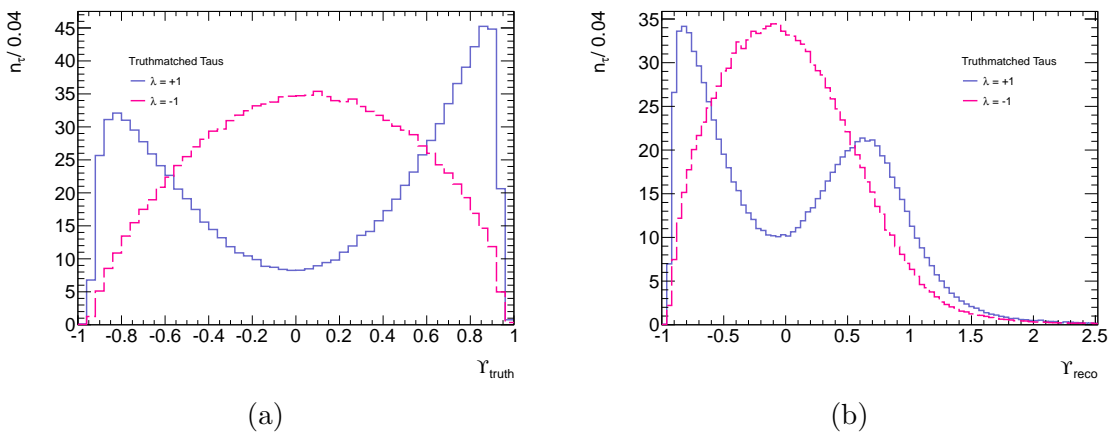
Figure 7.8: The truth (a) and reconstructed (b) charged energy asymmetry for truth-matched taus decaying to rhos. The distributions are normalized to unity.

	Sensitivity
Υ_{truth}	0.402
Υ_{reco}	0.326

Table 7.3: Sensitivity of the truth and reconstructed Υ for truthmatched taus decaying to rhos.

In Figure 7.8 the truth and reconstructed charged energy asymmetry are shown for truthmatched taus decaying to rhos. It is seen that around $\Upsilon = 1$, the reconstructed charged energy asymmetry is smeared out due to detector effects.

Sensitivities of truth and reconstructed charged energy asymmetry are calculated using Equation 3.23 taking the polarization to be -0.1211. The result is shown in Table 7.3 from which it is seen that the detector reduces the sensitivity by about 20%.

7.3   Effect of the Event Selection on the Tau Polarization

Besides the detector effects, the event selection can cause a bias in the selection towards right-handed or left-handed τ^-.

Effect of the Data Skimming

The data skimming, consisting of loose cuts described in Section 6.1, cuts harder on the right-handed τ^- than the left-handed τ^-. This is seen in Table 7.4 where the polarization asymmetry becomes more negative (from -0.1211 to -0.362) and thereby the difference between the number of left-handed and right-handed τ^- becomes larger.

This difference in efficiency caused by the trigger requirement in the skimming. The triggers, EF_mu18 and EF_mu18_medium, are fully efficient at $p_{\text{T}}(\mu)$ above 20 GeV and fire rarely if $p_{\text{T}}(\mu)$ is smaller than 20 GeV. From Figure 7.6 (d) it is that requiring $p_{\text{T}}(\mu) > 20\text{GeV}$, will cut harder on right-handed than on left-handed τ^-.

Cuts on the kinematics of the muon from a tau decay will affect the hadronically decaying tau as well since they are correlated through their spin.

Effect of the Event Selection

As seen in Table 7.4, the rest of the full selection cuts harder on the left-handed τ^- than on the right-handed τ^-. The bias from the skimming cuts are somewhat evened out resulting in a polarization of -0.231 after full selection. This is due to the cut on the transverse momentum of the hadronic tau. As it can be seen in Figures 7.6 (a) and (b), a cut on the p_{T} of the tau will cut harder on left-handed than on right-handed τ^-. Despite the fact that the cuts are not as hard on the right-handed taus in the final selection, the polarization after full event selection is still larger than the initial polarization of -0.1211.

Due to the different number of right-handed and left-handed τ^-, the fraction of QCD multijet events will be different in the two samples throughout the event selection.

The distributions of the reconstructed charged energy asymmetry for right-handed and left-handed τ^- are shown for all one prong taus passing the full selection in Figure 7.9. The sensitivity for the distributions in Figure 7.9 is calculated using Equation 3.23 with

Cut	N_L	N_R	P_τ
Full Sample	2764480 ± 1930	2167270 ± 1710	-0.121 ± 0.001
Skimming	148522 ± 217	69533 ± 148	-0.362 ± 0.001
Object Selection	8663 ± 85	4422 ± 63	-0.324 ± 0.008
Opposite Sign Charge	8555 ± 84	4378 ± 62	-0.323 ± 0.008
Dilepton Veto	8545 ± 84	4373 ± 62	-0.323 ± 0.008
W Suppression Cuts	6814 ± 77	3715 ± 58	-0.294 ± 0.009
$35\text{GeV} < m_{vis} < 75\text{GeV}$	5493 ± 69	3179 ± 54	-0.267 ± 0.010
One Prong Taus	3590 ± 55	2245 ± 45	-0.231 ± 0.012
(Polarization measurement only)			

Table 7.4: Number of $\tau_L^- \tau_R^+$ pairs (N_L), $\tau_R^- \tau_L^+$ pairs (N_R), and the tau polarization through the event selection. The luminosity is normalized to 4.63 fb^{-1}.

a polarization of -0.231 resulting in a sensitivity of 0.335. By comparing the sensitivity after selection with the sensitivity before, it is seen that they are comparable. Hence the selection do not affect the sensitivity of the charged energy asymmetry.
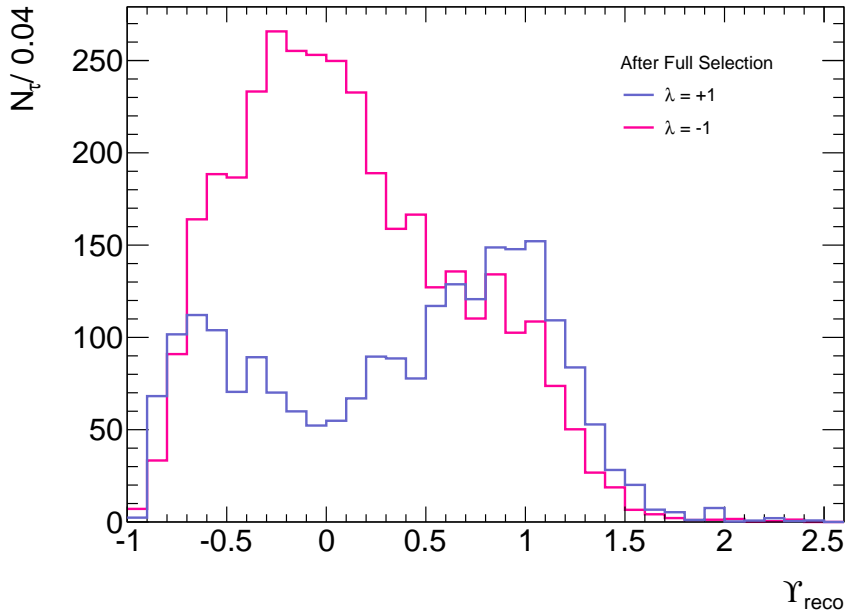
Figure 7.9: Reconstructed Υ for all one prong taus passing the full selection

7.4   Summary

In this chapter a method for re-establishing the tau helicity in a polarized Monte Carlo sample has been introduced. The method requires knowledge of the average tau polarization of Z as a function of the center of mass energy and scattering angle dependence of Z. It was found that the dependence on the pseudo-rapidity used to measure the scattering angle was negligible compared to the dependence on center of mass energy. The results of the tau helicity re-establishing method is seen to correspond well to the expected distributions. An average polarization of -0.1211 was found in the sample.

The decrease in sensitivity of the charged energy asymmetry due to detector effects have been investigated. The sensitivity is 20% lower for the reconstructed charged energy asymmetry compared to the truth value. A significant correlation was seen between reconstructed and truth charged energy asymmetry.

The data skimming cuts harder on right-handed than left-handed τ^- resulting in a more negative tau polarization. This is caused by the trigger requirement in the data skimming cuts. After the final selection the tau polarization is -0.231 compared to -0.1211 before any cuts were applied.

Polarization Measurement

In this chapter the method for measuring the tau polarization and the results of the measurement will be presented.

8.1 Charged Energy Asymmetry After Full Selection

In Figure 8.1, the charged energy asymmetry is plotted for data and Monte Carlo. The reconstructed taus in Monte Carlo have been matched to a true tau and associated with a pion, rho or other decays. The simulated taus not matched to true hadronic tau decays are labelled "Not Hadronic"
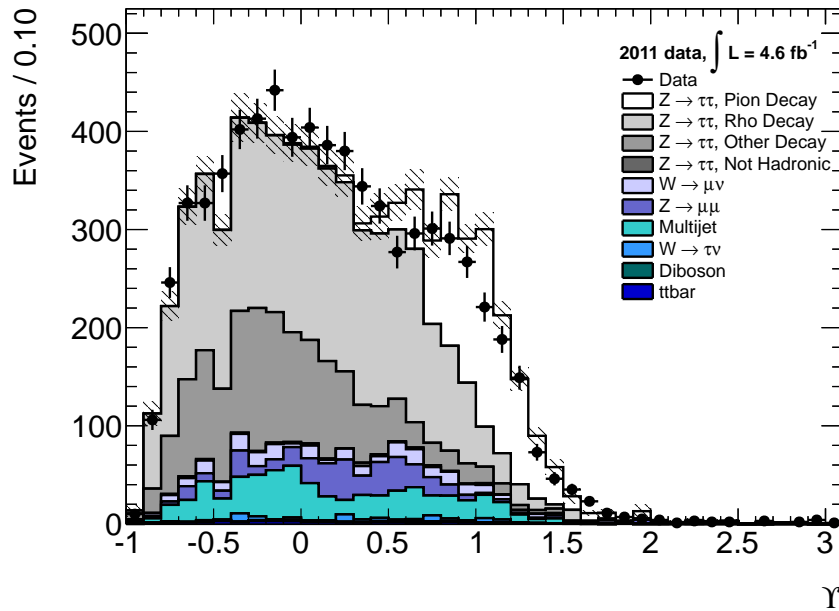
Figure 8.1: Charged energy asymmetry after the full selection. The simulated taus are divided into decay types. ATLAS TAUOLA default branching fractions used for Monte Carlo, see Table 8.1.

Decay Mode	Monte Carlo Samples Branching fraction [%]	Particle Data Group Branching fraction [%]
$h^- \nu_\tau$	13.04	11.61 ± 0.06
$h^- \pi^0 \nu_\tau$	26.75	25.94 ± 0.09
$h^- \geq 2\pi^0 \nu_\tau$	10.13	10.85 ± 0.11

Table 8.1: Branching fractions of one prong hadronic tau decays in the signal Monte Carlo sample and from the Particle Data Group[3]. h^- denotes a charged hadron. The statistical uncertainties on the Monte Carlo numbers are negligible.

By comparing branching fractions of taus in the simulation to the world average branching fractions from the Particle Data Group[3] (PDG), a difference was found. The branching fractions for one prong hadronic tau decays in the signal Monte Carlo sample and from the Particle Data Group are listed in Table 8.1. Especially the branching fraction for decays with one charged hadron and no π^0 differs substantially between the simulation and the value from PDG. It is therefore necessary to scale the contributions from each decay mode to the branching fraction from PDG.
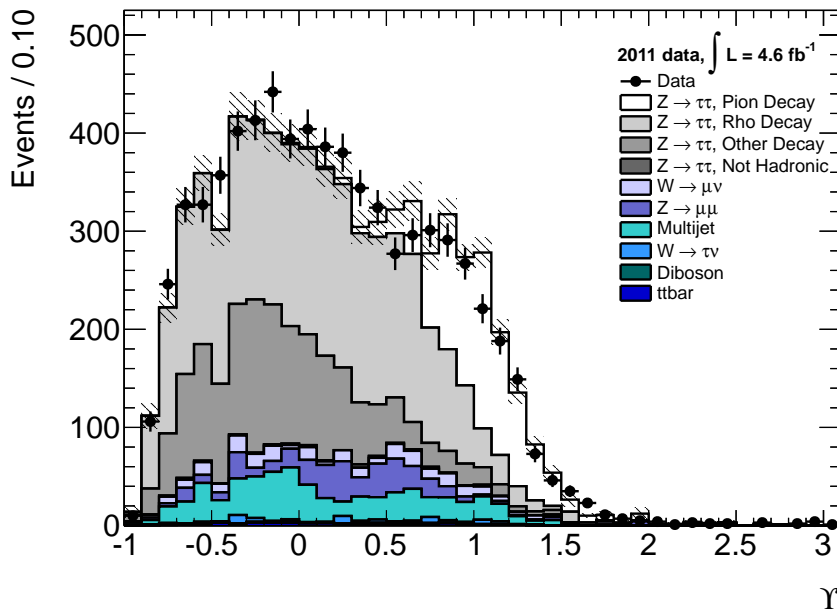
Figure 8.2: Charged energy asymmetry after the full selection. Monte Carlo branching fraction correct to PDG values, see Table 8.1.

In Figure 8.2, the charged energy asymmetry is plotted again, this time with the contributions from the different tau decay modes normalized to the branching fractions from the Particle Data Group. Whereas all plots presented previously in this thesis were based on the default ATLAS TAUOLA branching fractions, results from now on, will be based on the PDG numbers.

8.2 Fitting Method

The polarization is measured by fitting the sum of a right-handed and a left-handed template to data.

Two fitting methods is used, the method of least squares and a likelihood fit.

Fitting Templates

The templates used in the fit are the left-handed and right-handed simulated samples created with the method described in Section 7.1. The distributions consists of taus passing all cuts described in Chapter 6. Both templates are normalized separately to an integrated luminosity of 4.6 fb^{-1}.

In Figure 8.3 the fitting templates for right-handed and left-handed τ^- are shown along with the data points. The tau branching fractions in signal Monte Carlo are scaled to the values from Particle Data Group as discussed in Section 8.1. It is seen, that there are fewer right-handed τ^- compared to data and left-handed τ^-, and more left-handed τ^- than data. This is due to the difference between the cut efficiencies of $\tau_R^- \tau_L^+$ pairs and $\tau_L^- \tau_R^+$ pairs as discussed in Section 7.3.

The binning of the templates in Figure 8.3 have been chosen to reduce the bin-by-bin statistical fluctuations while retaining a sufficiently number of bins to keep the shape information of the Monte Carlo templates.

Method of Least Squares

In χ^2 fitting, or the method of least squares, the χ^2 function depending on the parameters you want to fit, is minimized. The χ^2 function is given as:

$$\chi^2 = \sum_{i=1}^{n_{bins}} \left(\frac{N_{\text{obs}}^i - N_{\text{exp}}^i}{\sigma_{N_{\text{obs}}}^i} \right)^2 \tag{8.1}$$

where N_{obs}^i and N_{exp}^i are the observed and the expected number of events in bin i, respectively, and $\sigma_{N_{\text{obs}}}^i$ is the uncertainty on the observed number of events in bin i. The observed number of events in each bin follows a Poisson distribution. By requiring $N_{\text{obs}}^i > 10$ in all bins, the uncertainty can be approximated to

$$\sigma_{N_{\text{obs}}}^i = \sqrt{N_{\text{obs}}^i} \tag{8.2}$$

The expected number of events, N_{exp}^i, depends on the fit parameters that are varied to minimize χ^2. It is calculated as

$$N_{\text{exp}}^i = N_{\text{MC}} \left(\left(\frac{1 - P_\tau}{2} \right) \mu_L n_L^i + \left(\frac{1 + P_\tau}{2} \right) \mu_R n_R^i + n_{EW}^i \right) + \mu_{QCD} \cdot n_{QCD}^i \tag{8.3}$$

Here the parameters left free to vary in the fit are

- P_τ: The tau polarization which is the parameter of interest in the fit.
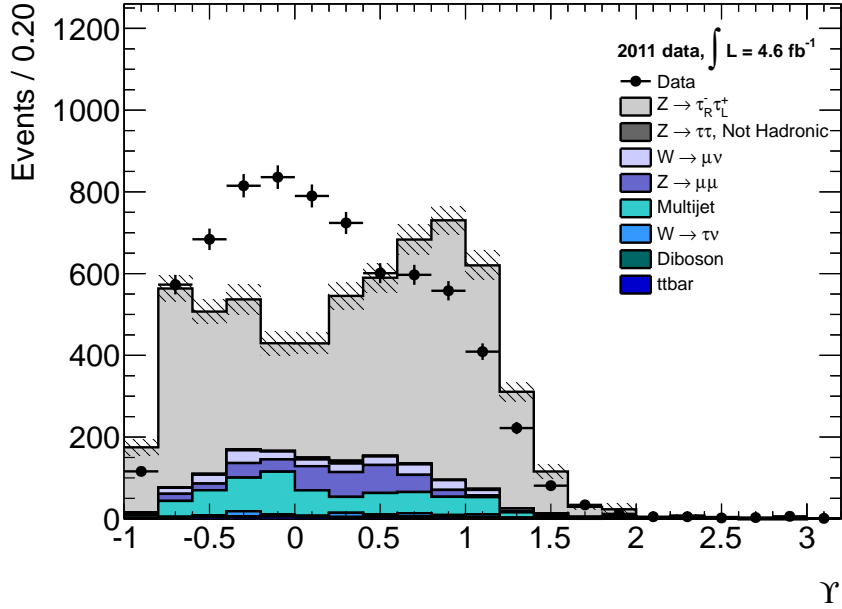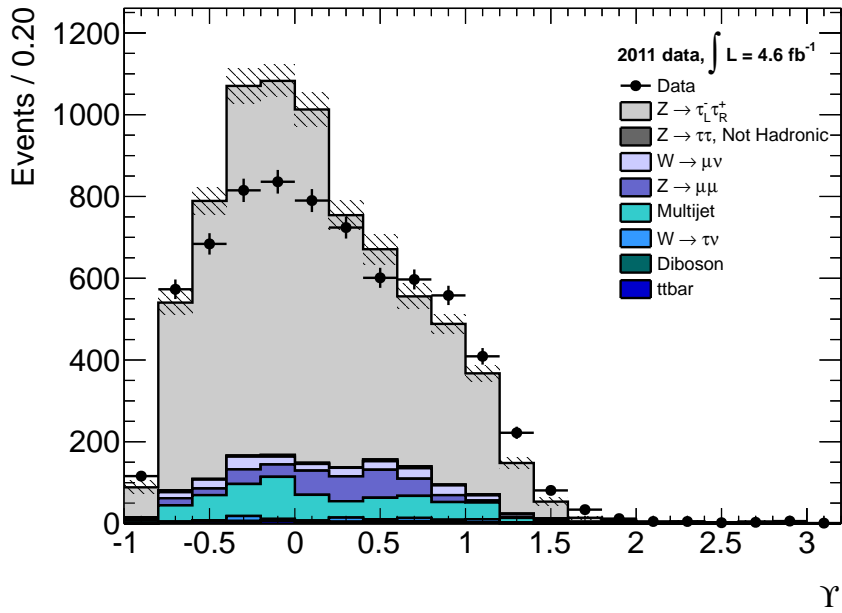
Figure 8.3: Templates of charged energy asymmetry for right-handed (a) and left-handed (b) τ^- compared to data. Each of the two Monte Carlo templates are normalized to 4.6 fb^{-1}.

- N_{MC}: A normalization factor to ensure that the Monte Carlo normalization is correct. N_{MC} is a nuisance parameter[1]. The nuisance parameter is kept in the fit to ensure that the tau polarization is not affected by the normalization.

whereas the other are

- n_L^i and n_R^i: Number of left-handed and right-handed taus in bin i of the two Monte Carlo templates, respectively.

- μ_L and μ_R: Luminosity normalization of the signal Monte Carlo.

- n_{EW}^i: Number of electroweak background in bin i given as

$$n_{EW}^i = \sum_b \mu_b n_b^i \tag{8.4}$$

where b is the background sources, μ_b is the luminosity normalization of background b, and n_b^i is the number of tau candidates in bin i of background b.

- n_{QCD}^i: The shape of the multijet QCD background in region C is expected to be the same as in the signal region as described in Section 6.7. It is given as

$$n_{QCD}^i = N_{obs,C}^i - N_{MC}\left(\left(\frac{1-P_\tau}{2}\right)\mu_L n_{L,C}^i + \left(\frac{1+P_\tau}{2}\right)\mu_R n_{R,C}^i + n_{EW,C}^i\right) \tag{8.5}$$

where the C in the subscript denotes that the number of events is in region C. The second term in Equation 8.5 is correcting for the presence of signal and electroweak background in region C before using the data in this region to estimate the multijet QCD background in the signal region.

- μ_{QCD}: The scale factor allowing us to use the QCD events in region C to estimate the QCD background in the signal region, A. It is given by

$$\mu_{QCD} = \frac{N_{QCD}^B}{N_{QCD}^D} \tag{8.6}$$

c.f. Equation 6.3.

To determine the goodness of a χ^2 fit the, calculated χ^2 is compared to the number of degrees of freedom[43], ndf, given as

$$\text{ndf} = n_{bins} - 2 \tag{8.7}$$

since we have two fit parameters, P_τ and the nuisance parameter, N_{MC}. From the calculated χ^2 and the number of degrees of freedom the probability of making an equally good or worse fit can be calculated.

The weakness of the method of least squares lies in bins with few observed events. In bins with few entries, Equation 8.2 breaks down and chi^2 is not appropriate.

---

[1] A nuisance parameter is a parameter that is not of immediate interest in the fit, but is kept in the fit to make it converge.

Method of Maximum Likelihood

The method of maximum likelihood uses a likelihood function, $\mathcal{L}$, that is maximized to find the optimal value for the fit parameters. The likelihood function describes the likelihood of an expected number of events given an observed number of events[43]. The probability is expected to be Poissonian leading to the following likelihood function

$$\mathcal{L}\left(P_\tau, \mathrm{N_{MC}}\right) = \prod_{i=1}^{n_\mathrm{bins}} \frac{e^{-\mathrm{N}_\mathrm{exp}^i} \left(\mathrm{N}_\mathrm{exp}^i\right)^{\mathrm{N}_\mathrm{obs}^i}}{\mathrm{N}_\mathrm{obs}^i!} \tag{8.8}$$

where the number of expected events in bin i, $\mathrm{N}_\mathrm{exp}^i$, depends on the fitting parameter P_τ and the nuisance parameter $\mathrm{N_{MC}}$ as described in Equation 8.3.

Instead of maximizing the likelihood, one minimizes minus 2 times the logarithm of the likelihood, $-2 \log \mathcal{L}$.

To determine the goodness of a likelihood fit, χ^2 with the fit parameters determined by the likelihood fit is calculated and compared to the number of degrees of freedom.

8.3   Fitting Results

The minimization of χ^2 and the likelihood function is performed using the MINUIT package[44] interfaced to ROOT. In particular, the MIGRAD minimization algorithm is used in the fitting.

The fit is performed in the range of the charged energy asymmetry from -1.0 to 2.0 with 15 bins in total. The number of degrees of freedom is therefore 13.

By using the templates from Figure 8.3 and the number of expected events given by Equation 8.3 the values for the fitting parameters, $\mathrm{N_{MC}}$ and P_τ, are given in Table 8.2. The correlation factor between the fit parameters and χ^2/ndf are stated as well.

From Table 8.2 it is seen that the value of the tau polarization for the maximum likelihood fit and the least square fit differs by 0.013. The χ^2/ndf are similar and thereby the goodness of the fits are equal. In Figure 8.4 the observed number of events is shown with both the χ^2 and the likelihood fit. It is seen that the two fits are virtually identical. Since the method of least squares does not handle bins with low statistics well, the values of the likelihood fit is used resulting in a tau polarization and Monte Carlo normalization factor of

$$P_\tau = -0.258 \pm 0.048$$
$$\mathrm{N_{MC}} = 0.992 \pm 0.014$$

In Figure 8.5 the likelihood fit is shown with the templates. The templates are scaled with the values of the fit parameters from the likelihood fit.

Parameter	Likelihood Fit			χ^2 Fit		
P_τ	-0.258	$\pm$	0.048	-0.271	$\pm$	0.048
N_{MC}	0.992	$\pm$	0.014	0.986	$\pm$	0.014
Correlation Factor	0.352			0.352		
χ^2/ndf	1.86			1.85		

Table 8.2: Result of fit without cut efficiencies.
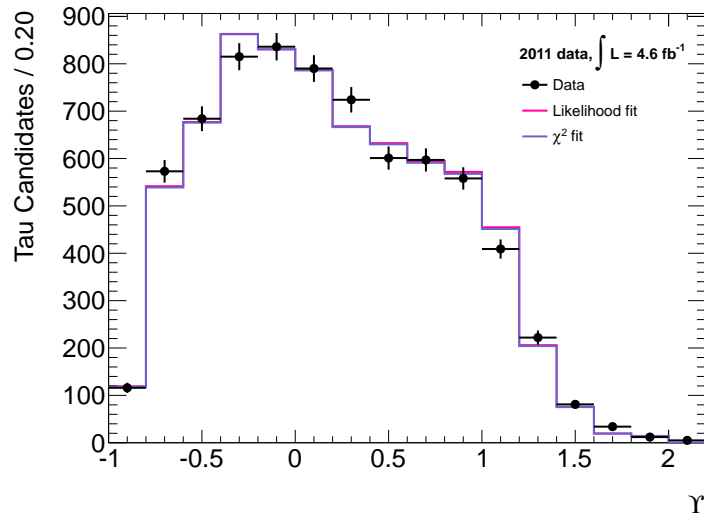
Figure 8.4: Template fit using the method of maximum likelihood (pink) and the method of least squares (blue).
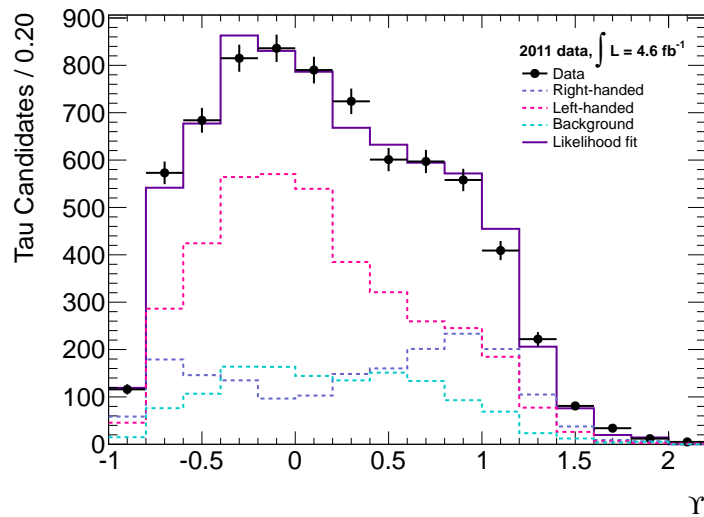
Figure 8.5: Template fit using the method of maximum likelihood (violet), the right-handed (blue) and left-handed (pink) templates excluding the background, and the background (cyan) scaled to the fit result.

8.4 Systematic Uncertainties

The measurement of the tau polarization is influenced by systematic uncertainties. In this section the sources of systematic uncertainties will be presented.

Effect of Limited Monte Carlo Statistics

In the fits, only the statistical uncertainty on data was taken into account and the statistical uncertainties on the Monte Carlo templates were ignored. They are, however, present and, as seen in Figure 8.3, of the same order as the uncertainties in data.

The templates are dominated by the statistics of the signal sample and especially the $Z(\to \tau\tau) + 0$ jets whose cross section is ~ 6 times higher than $Z(\to \tau\tau) + 1$ jet. From Table 6.1, it is seen that the simulated $Z(\to \tau\tau) +$ jets sample corresponds to about 2.7 times as much integrated luminosity as the real data. However, for the templates, the simulated data is divided into two almost equally large data sets resulting in 1.5 times as much statistics in the templates as in data. The other Monte Carlo samples will result in smaller statistical uncertainties due to their higher integrated luminosities.

In a dedicated Monte Carlo study, the sum of two templates each with 15000 entries were fitted to a distribution with 10000 entries. The fit was performed in two ways; first, by ignoring the uncertainties on the templates, then, by including the uncertainties with extra Poissionian terms for each bin in each template introducing a nuisance parameter for each bin in each template. This cannot be done in the real tau polarization fit, since there the templates contain weighted events that do not follow Poissonian statistics.

From this study, an increase in the uncertainties of the fit parameters of 16% was observed when including the statistical uncertainties on the templates. Assuming that the two contributions add in quadrature, this corresponds to an uncertainty from the template statistics of 60% of that of the data statistics. Transferring this result to the proper polarization fit gives:

$$P_\tau = -0.258 \pm 0.048(\text{stat.}) \pm 0.028(\text{MC})$$
$$N_{\text{MC}} = 0.992 \pm 0.014(\text{stat.}) \pm 0.008(\text{MC})$$

Pileup Reweighting Scale Factor

In the pileup reweighting described in Section 6.1, the entire Monte Carlo distribution of the number of primary vertices per bunch crossing should be scaled by a factor of $0.83^{+0.05}_{-0.08}$ according to ATLAS recommendations. To investigate the effect of the pileup reweighting on the polarization measurement the scale is increased by 0.05 and decreased by 0.08 and the entire analysis, including the $Z \to \tau\tau$ selection, is redone for both scales.

Tau Energy Scale

The energy of the hadronically decaying tau is calibrated. There are uncertainties on the scale dependent on the pseudo-rapidity, the p_{T}, and the number of tracks of the taus. In Table 8.3, the uncertainties on the tau energy scale for one prong taus as recommended by the ATLAS Tau Working Group are stated.

1 Prong Taus	$\lvert\eta\rvert < 1.3$	$1.3 < \lvert\eta\rvert < 1.6$	$1.6 < \lvert\eta\rvert$
$15\text{GeV} < p_\text{T} < 20\text{GeV}$	3.0%	3.5%	3.0%
$20\text{GeV} < p_\text{T} < 50\text{GeV}$	2.5%	3.0%	2.5%
$50\text{GeV} < p_\text{T}$	3.0%	3.5%	3.0%

Table 8.3: Uncertainties on the tau energy scale for one track taus.

Since the energy of the tau is used in the missing transverse energy reconstruction, the uncertainties on the tau energy will affect the E_T^miss as well. The E_T^miss is therefore scaled simultaneously with the tau energy scale as described in Reference [39].

The entire selection and the fit is redone with the tau energy scaled up and down by the amounts from Table 8.3, where full correlation has been assumed between the different points. The Υ variable was re-calculated with the new tau energy.

Tau Identification Uncertainty

The tau identification used in the selection, BDT tight, has an overall uncertainty of 4% estimated by the ATLAS Tau Working Group. This uncertainty is an overall number and the Tau Working Group provides no recommendations on the efficiency as function of Υ. By assuming the 4% to be flat in Υ, only the normalization factor will be affected.
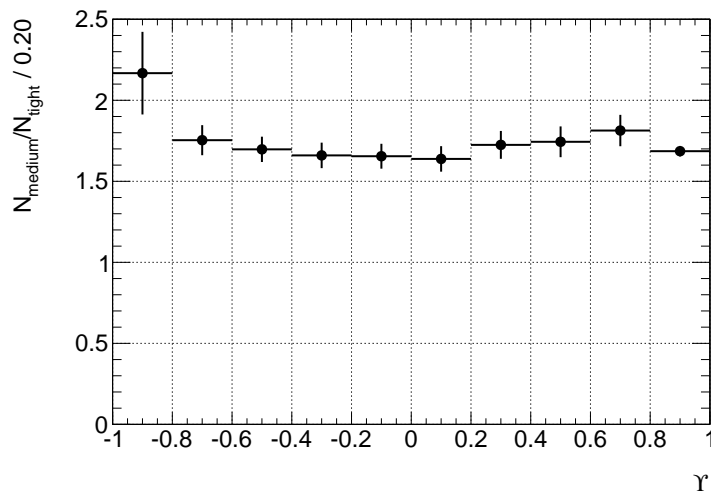
Figure 8.6: Number of taus passing BDT medium compared to number of taus passing BDT tight in the selection as a function of Υ.

The variables used in the charged energy asymmetry are also used by the tau BDT identification. To investigate the effect of lowering the tau identification cut, events passing the full selection with BDT medium is compared to events passing BDT tight in Monte Carlo. As seen in Figure 8.6, lowering the tau identification cut has an effect on the shape of the Υ variable. Lowering the cut to BDT medium has a large impact on the number

of identified taus and can thus not be directly compared to the overall tau identification uncertainty of 4%. The study of comparing taus passing BDT tight to taus passing BDT medium is used to indicate the shape of the tau identification uncertainty.

To investigate how the polarization is affected by a shape-dependent tau identification uncertainty, two different models for the uncertainty as a function of the charged energy asymmetry are studied, a linear model and a quadratic model. The two models are motivated by the study of the comparison of taus passing BDT medium and taus passing BDT tight.

For the signal the effect of the linear model is investigated by scaling the predicted number of right-handed and left-handed signal events in each bin with a linear function given by

$$f(\Upsilon) = 1 \pm 0.02y \quad \text{where} \quad \begin{cases} y = \Upsilon & \text{for } \Upsilon \leq 1 \\ y = 1 & \text{for } \Upsilon > 1 \end{cases} \tag{8.9}$$

Since $\Upsilon > 1$ is unphysical and caused by detector resolution, the correction for candidates with $\Upsilon > 1$ has been damped to what it would have been for $\Upsilon = 1$. It is estimated that the difference between the tau identification uncertainties between the neutral energy dominated region ($\Upsilon = -1$) and the charged energy dominated region ($\Upsilon = 1$) is 4%.

The quadratic model of the tau identification uncertainty for the signal is given by

$$f(\Upsilon) = 1 \pm 0.03y^2 \quad \text{where} \quad \begin{cases} y = \Upsilon & \text{for } \Upsilon \leq 1 \\ y = 1 & \text{for } \Upsilon > 1 \end{cases} \tag{8.10}$$

It is estimated that the difference between the uncertainty at the minimum (maximum) at $\Upsilon = 0$ and the maximum (minimum) at $\Upsilon = \pm 1$ is 3%.

The effects of the linear and quadratic model of the uncertainty dependence on the charged energy asymmetry for signal on the tau polarization are listed in Table 8.4.

The effect of the uncertainty of the tau identification on the normalization factor is investigated by scaling the signal sample with 4% according to the Tau Working Group recommendations.

Uncertainty on the Background Shape

The uncertainty on the shape of the background is assumed to be greater than for the signal because most of the background events arise from jets misidentified as taus.

To study the effect of the shape-dependent tau identification uncertainty of the background the linear and quadratic models from Equations 8.9 and 8.10 are used. The scales 0.02 and 0.03 are substituted with 0.20. Only the background is scaled while the signal is kept constant.

The effect on the tau polarization of the linear and quadratic model of the tau identification uncertainty for the background are listed in Table 8.4.

The uncertainty on the background shape will only affect the tau polarization since varying the shape is expected to have no influence on the normalization.

Tau Branching Fractions

As described in Section 8.1, the contributions from the different tau decay modes were normalized to the branching fraction from Particle Data Group. To investigate how the

Shape Model	Sample	Scale	ΔP_τ
Linear Model	Signal	$\pm 2\%$	0.022
Quadratic Model	Signal	$\pm 3\%$	0.033
Total	Signal		0.040
Linear Model	Background	$\pm 20\%$	0.021
Quadratic Model	Background	$\pm 20\%$	0.017
Total	Background		0.027

Table 8.4: Effect on the tau polarization of linear and quadratic model of the tau identification uncertainty of the signal and background separately.

tau polarization is affected by uncertainties on the tau branching fractions, the branching fractions are varied independently with the uncertainties listed in Table 8.1 and the fit is redone.

Other Systematic Uncertainties

The following systematic effects were investigated and it was found that they only had little or no impact on the tau polarization.

- Luminosity:

  There is a 3.7% uncertainty on the measurement of the integrated luminosity[45]. Since the luminosity only enters the fit in the luminosity scales, μ_L, μ_R, and μ_{EW}, in Equation 8.3 only the normalization parameter, N_{MC}, will be affected by the uncertainty on the integrated luminosity. The fit is redone with the luminosity scaled up and down with 3.7%.

- Muon p_T Smearing:

  The muon p_T is smeared in the Monte Carlo to resemble the resolution in data. Since we have selected a combined muon the p_T is smeared in both the inner detector and the muon spectrometer. An uncertainty arises from the smearing[46] and the effect of the uncertainty is investigated by varying the p_T smearing of the track in the inner detector and in the muon spectrometer separately. The event selection and the fit are redone with muon p_T resolution varied.

- Muon Efficiency:

  The efficiency of the muon reconstruction is scaled in Monte Carlo to resemble data. The muon efficiency scale factor has an uncertainty of less than 1%[47]. It is not expected to have a large impact on the tau polarization nor the normalization factor. It is studied by varying the muon efficiency scale factor up and down in Monte Carlo and redo the entire analysis including the $Z \to \tau\tau$ selection.

- Normalization Factors for W + jets background:

  The influence on the tau polarization and the normalization factor from the uncertainties on the normalization factor for the W + jets background described in

Section 6.7 is investigated by varying the normalization factors and redo the fit. The normalization factors of same sign and opposite sign charge regions are varied independently. The effect of this systematic is expected to be small since only few W+jets events pass the selection.

- Multijet Background:

  The estimation of the multijet QCD background has an uncertainty that will influence the polarization and normalization as it enters in Equation 8.3. The scale μ_{QCD} is

$$\mu_{QCD} = \frac{N_{QCD}^B}{N_{QCD}^D} = 1.049 \pm 0.019(\text{stat.}) \pm 0.032(\text{sys.}) \qquad (8.11)$$

  where B and D are control regions. The systematic uncertainty on μ_{QCD} is taken from Reference [39].

  The effect of the uncertainty on the estimation of QCD background is investigated by varying μ_{QCD} up and down by 0.04 and redo the fit.

- Theoretical Cross Sections

  The theoretical cross sections used to calculate the corresponding integrated luminosity in Table 6.1 have uncertainties affecting the luminosity scales, μ, in Equation 8.3.

  From the cut flow Table of the selection, Table 6.3, it is seen that the main contributions to the charged energy asymmetry distribution are $Z \to \tau\tau$, $Z \to \mu\mu$, $W \to \mu\nu$, and QCD background. It is therefore the uncertainties on the theoretical cross sections of $Z \to \ell\ell$ and $W \to \ell\nu$ that are investigated.

  The uncertainty on the $Z \to \ell\ell$ cross section is 5.1% and the uncertainty on the $W \to \ell\nu$ cross section is 5.0%[40]. The impact on the tau polarization and the normalization factor is studied by scaling the cross section independently and redo the fit.

  The uncertainty on the $W \to \ell\nu$ is not expected to influence the tau polarization nor the normalization factor very much since the number of $W \to \ell\nu$ that passed the full selection is very low. The uncertainty on the $Z \to \ell\ell$ cross section is on the other hand expected to affect the normalization factor since $Z \to \tau\tau$ events are dominating the charged energy asymmetry distribution.

- Fitting Method:

  The fit is done with 15 bins. To evaluate how the number of bins affect the measurement of the tau polarization and the normalization factor, the fit is redone with 30 bins still in the range $-1 < \Upsilon < 3$.

Summary of Systematic Uncertainties

The systematic uncertainties are summarized in Table 8.5. From this it is seen that the systematic uncertainty with the largest effect on the tau polarization is the shape

Source of Uncertainty	ΔP_τ	ΔN_{MC}
Luminosity	0.000	0.038
Pileup	0.030	0.013
Tau Energy Scale	0.046	0.059
Tau Identification, Signal	0.040	0.038
Uncertainty on Background Shape	0.027	-
Muon p_T Smearing	0.000	0.000
Muon Efficiency	0.000	0.000
W Normalization factors	0.000	0.000
Multijet Background	0.002	0.003
W Cross Section	0.001	0.001
Z Cross Section	0.001	0.051
Tau Branching Fractions	0.006	0.003
Fitting Method	0.001	0.000
Total Systematic Uncertainty	0.073	0.096

Table 8.5: Summary of the systematic uncertainties and their effect on the tau polarization and the normalization factor.

dependent tau identification uncertainty on the signal, whereas the largest effect on the normalization arises from uncertainties on the tau energy scale.

The systematic uncertainties are assumed to be uncorrelated and the total systematic uncertainty is:

$$\sigma_{tot}^{sys} = \sqrt{\sum_i \left(\sigma_i^{sys}\right)^2} \tag{8.12}$$

where i is the source of the systematic uncertainty. The total systematic uncertainties on the tau polarization and the normalization factor are listed in Table 8.5.

8.5 Summary

In this section, the charged energy asymmetry after full event selection was presented. It was found that the tau branching fractions in the $Z \rightarrow \tau\tau$ simulations were not in agreement with the values from Particle Data Group. Therefore the contributions from different tau decay modes were scaled to the branching fractions from Particle Data Group.

The method for measuring the tau polarization by fitting has been presented. The tau polarization has been measured to be

$$P_\tau = -0.258 \pm 0.048(\text{stat.}) \pm 0.0028(\text{MC}) \pm 0.073(\text{sys.})$$

where (stat.) refers to the statistical uncertainty of the fit, (MC) to uncertainties arising from the limited statistics in the simulations, and (sys.) refers to the systematic uncertainties.

In the tau polarization measurement, the Monte Carlo normalization was kept as a free parameter to make the measurement independent of the normalization. From the systematic uncertainties on the normalization factor listed in Table 8.5, it is seen that it

was a good choice to keep the normalization as a free parameter in the fit since some of the uncertainties on the normalization factor might have propagated into the tau polarization.

Conclusion

The tau polarization was measured in one prong hadronic tau decays, by use of the variable Υ, which measures the energy asymmetry between charged and neutral pions. Templates of right-handed and left-handed taus were fitted to the data. In the fit, the normalization was kept as a free parameter, and the tau polarization was extracted entirely from the shape of the charged energy asymmetry. It was found that the tau branching fraction in the signal Monte Carlo differed from the values from Particle Data Group (PDG), the signal Monte Carlo samples were therefore scaled to the tau branching fractions from PDG. The result of the measurement is

$$P_\tau = -0.258 \pm 0.048(\text{stat}) \pm 0.028(\text{MC}) \pm 0.073(\text{sys.})$$

The measured tau polarization lies within 1.5σ of the expected value of -0.120 from the Monte Carlo sample.

Another result of the study is expressed through a normalization factor, which is the ratio between the observed number of events in real data and in simulation. This was found to be

$$\text{N}_{\text{MC}} = 0.992 \pm 0.014(\text{stat.}) \pm 0.008(\text{MC}) \pm 0.096(\text{sys.}) \tag{9.1}$$

showing an excellent agreement between observation and expectation.

The effect of the systematic uncertainties and statistical uncertainties on the Monte Carlo samples where evaluated for both the normalization factor and the tau polarization.

The tau polarization depends on the center of mass energy. At the LHC a range of center of mass energies are studied and the result of the tau polarization measurement at the LHC can therefore not be directly compared to the result from LEP[1].

In the work with the tau polarization, it has been necessary to re-establish the tau helicity in the signal Monte Carlo samples. The original tau helicity was lost in the generation of Monte Carlo samples and therefore a method for restoring the tau helicity has been developed. The results of the re-establishment of tau helicity were compared to and agreed with a Pythia+TAUOLA standalone run, where the original tau helicity was accessible.

More data would improve the measurement of the tau polarization by reducing the statistical uncertainty of the fit. The systematic uncertainty on the tau polarization is of the same order as the statistical uncertainty and might be reduced by more data resulting by lowering uncertainties on tau energy scale, tau identification, etc.

It would also be beneficial for the tau polarization measurement to study more thoroughly the efficiencies as a function of Υ. It has been beyond the scope of this thesis to study these effects in detail.

In this thesis all one prong taus where used in the tau polarization measurement. However, the pion channel carries no information on the tau polarization in the charged energy asymmetry. By mixing the templates with events not sensitive to the tau polarization the sensitivity decreases. It would therefore improve the sensitivity of the templates if one knew the substructure of the reconstructed tau, i.e. number of neutral pions, and thereby reject pion decays which will have no neutral pions.

In conclusion, this thesis presents the first measurement of the tau polarization in $Z \to \tau\tau$ events at a hadron collider.

Part IV

Appendix

A

Appendix to $Z \rightarrow \tau\tau$ Selection

A.1 Jet Cleaning Cuts

The cuts for jet and tau cleaning are:

- $f_{\mathrm{em}} > 0.90$ and $|f_{\mathrm{quality}}| > 0.8$ and $|\eta| < 2.8$

- $|t| > 10$ ns

- $f_{\mathrm{em}} < 0.05$ and $f_{\mathrm{ch}} < 0.1$ and $|\eta| < 2.0$

- $f_{\mathrm{em}} > 0.95$ and $f_{\mathrm{ch}} < 0.05$ and $|\eta| \geq 2.0$

The cuts are applied with a logical "OR" condition. The variables used in the cleaning cuts are:

- f_{em} : Fractional energy measured in EM calorimeter

- $|f_{\mathrm{quality}}|$: Measure of the quality of the jet in the Liquid Argon calorimeter.

- f_{ch} : Charge fraction is the ratio of the sum of the transverse momenta of tracks associated to a jet and originating at the primary vertex, to the jet calorimetric transverse momentum.

- t : Jet time (energy-squared-weighted time of cells within a jet) with respect to the event time.

A.2   Muon Track Quality Cuts

The muon track quality cuts are

- no BlayerHit expected or nBLayerHits > 0

- nPixHits + nDeadPixelSensors > 1

- nSCTHits + nDeadSCTSensors > 5

- nPixHoles + nSCTHoles < 3

- Two cases for the track in the Transition Radiation Tracker (TRT):

   $|\eta| < 1.9$:
   nTRTOutliers / (nTRTHits + nTRTOutliers) < 0.9 and nTRTHits + nTRTOutliers > 5

   $|\eta| \geq 1.9$:
   (nTRTHits + nTRTOutliers > 5 and nTRTOutliers / (nTRTHits + nTRTOutliers) < 0.9)
   or nTRTHits + nTRTOutliers < 6

The variables used in the muon track quality cuts are

- no BlayerHit expected: The muon track passes through an uninstrumented or dead part of the barrel part of the pixel detector.

- nBlayerHits: Number of hits in the barrel part of the pixel detector

- nPixHits (nSCTHits): Number of track hits in the pixel detector (SCT detector)

- nDeadPixelSensors (nDeadSCTSensors): Number of dead Sensors in the pixel detector (SCT detector) traversed by the track.

- nPixHoles (nSCTHoles): Number of holes in the pixel detector (SCT detector) traversed by the track.

- nTRTHits: Number of hits in the TRT caused by the track.

- nTRTOutliers: Number of hits in TRT in the track associated as outliers (not caused by the muon).

List of Figures

List of Tables

Bibliography

[1] ALEPH Collaboration, DELPHI Collaboration, L3 Collaboration, OPAL Collaboration, SLD Collaboration, LEP Electroweak Working Group, and SLD Electroweak and Heavy Flavour Groups. Precision Electroweak Measurements on the Z Resonance. *Phys. Rep.*, 427, 2005.

[2] ALEPH Collaboration. Determination of the number of light neutrino species. *Physics Letters B*, 231(4):519–529, 1989.

[3] K. Nakamura et al. (Particle Data Group). The review of particle physics. *J. Phys. G*, 37, 2010.

[4] Jan Ambjørn and Jens Lyng Petersen. Quantum Field Theory. Niels Bohr Institute, University of Copenhagen, January 1999.

[5] Michael E. Peskin and Daniel V. Schroeder. *An Introduction to Quantum Field Theory*. Westview Press, 1995.

[6] Guy D. Coughlan, James E. Dodd, and Ben M. Gripaios. *The Ideas of Particle Physics*. Cambridge University Press, third edition, 2006.

[7] Francis Halzen and Alan D. Martin. *Quarks and Leptons: An Introductory Course in Modern Particle Physics*. John Wiley & Sons, 1984.

[8] Alessandro Bettini. *Introduction to Elementary Particle Physics*. Cambridge University Press, 2008.

[9] B. R. Martin and G. Shaw. *Particle Physics*. John Wiley and Sons Ltd, 2008.

[10] Mogens Dam. *Tests of the Electroweak Theory with the DELPHI Detector at LEP*. PhD thesis, Departments of Physics, University of Oslo, 1995.

[11] Yung-Su Tsai. Decay Correlations of Heavy Leptons in $e^+ + e^- \rightarrow l^+ + l^-$. *Phys. Rev. D*, 4(9):2821–2837, 1971.

[12] B.K. Bullock, K. Hagiwara, and A.D. Martin. Tau Polarization and its Correlations as a Probe of New Physics. *Nuclear Physics B*, 395(3):499–533, 1993.

[13] André Rougé. Tau decays as polarization analysers. *1st Workshop on Tau-lepton Physics, Orsay, France, 24-27 Sep 1990*, pages 213–222, 1991.

[14] M. Davier, L. Duflot, F. Le Diberder, and A. Rougé. The optimal method for the measurement of tau polarization. *Physics Letters B*, 306(3-4):411–417, June 1993.

[15] R. K. Ellis, I. Hinchliffe, M. Soldate, and J. J. Van Der Bij. Higgs decay to $\tau^+\tau^-$: A possible signature of intermediate mass higgs bsons at high energy handron colliders. *Nuclear Physics B*, 297(2):221–243, 1988.

[16] Z. Czyczula and M. Dam. Prospects of Measuring the Tau Polarization in $Z' \rightarrow \tau^+\tau^-$ events in ATLAS. Technical Report ATL-COM-PHYS-2009-174, CERN, Geneva, 2009.

[17] http://sherpa.hepforge.org/dokuwiki/lib/exe/detail.php?media=sketch.gif.

[18] Jonathan Pumplin, Daniel Robert Stump, Joey Huston, Hung-Liang Lai, Pavel Nadolsky, and Wu-Ki Tung. New Generation of Parton Distributions with Uncertainties from Global QCD Analysis. *Journal of High Energy Physics*, 017, 2002.

[19] Sidney D. Drell and Tung-Mow Yan. Partons and their applications at high energies. *Annals of Physics*, 66(2):578–623, 1971.

[20] J. M. Campbell, J. W. Huston, and W. J. Stirling. Hard interactions of quarks and gluons: a primer for LHC physics. *Reports on Prpgress in Physics*, 70(1), 2007.

[21] Ask Emil Jensen. *Dilepton final states with ATLAS at $\sqrt{s} = 7$ TeV.* PhD thesis, Copenhagen University, Copenhagen, Copenhagen, 2011.

[22] Torbjörn Sjöstrand, Stephen Mrenna, and Peter Skands. A brief introduction to PYTHIA 8.1. *Computer Physics Communications*, pages 852–867, 2008.

[23] H.L. Lai, J. Huston, S. Kuhlmann, J. Morfin, F. Olness, J.F. Owens, J. Pumplin, and W.K.Tung. Global QCD analysis of parton structure of the nucleon: CTEQ5 parton distributions. *The European Physical Journal C - Particles and Fields*, 12(3):375–392, 2000.

[24] B. Andersson, G. Gustafson, G. Ingelman, and T. Sjöstrand. Parton fragmentation and string dynamics. *Physics Reports*, 97(2-3):31–145, July 1983.

[25] G. Corcella, I. G. Knowles, G. Marchesini, S. Moretti, K. Odagiri, P. Richardson, M. H. Seymour, and B. R. Webber. HERWIG 6.5: an event generator for Hadron Emission Reactions With Interfering Gluons (including supersymmetric processes). *JHEP*, 01:010, 2001.

[26] Michelangelo L. Mangano, Mauro Moretti, Fulvio Piccinini, Roberto Pittau, and Antonio D. Polosa. Alpgen, a generator for hard multiparton processes in hadronic collisions. *JHEP*, 07, 2003.

[27] Stefano Frixione and Bryan R. Webber. Matching NLO QCD computations and parton shower simulations. *JHEP*, 06:029, 2002.

[28] J. Butterworth, J. Forshaw, and M. Seymour. Multiparton interactions in photo-production at HERA. *Zeitschrift für Physik C Particles and Fields*, 72(4):637–646, 1996.

[29] N. Davidson, G. Nanava, T. Przedziński, E. Richter-Wąs, and Z. Wąs. Universal interface of TAUOLA: Technical and physics. *Computer Physics Communications*, 183(3):821–843, 2012.

[30] Elzbieta Richter-Wąs, D Froidevaux, and Luc Poggioli. ATLFAST 2.0 a fast simulation package for ATLAS. Technical Report ATL-PHYS-98-131, CERN, Geneva, 1998.

[31] John Allison, K. Amako, J. Apostolakis, H. Araujo, and P. Arce Dubois. Geant4 developments and applications. *IEEE Transactions on Nuclear Science*, 53(1):270–278, 2006.

[32] Christian Lefèvre. The CERN accelerator complex. Complexe des accélérateurs du CERN. December 2008.

[33] The ATLAS Collaboration. The ATLAS Experiment at the CERN Large Hadron Collider. *Journal of Instrumentation*, 3(08):S08003, 2008.

[34] Joao Pequenao. Event Cross Section in a computer generated image of the ATLAS detector. 2008.

[35] ATLAS Collaboration. Jet energy measurement with the atlas detector in proton-proton collisions at $\sqrt{s} = 7$ tev. oai:cds.cern.ch:1410621. Technical Report arXiv:1112.6426. CERN-PH-EP-2011-191, CERN, Geneva, 2011.

[36] ATLAS Collaboration. Expected electron performance in the ATLAS experiment. Technical Report ATL-PHYS-PUB-2011-006, CERN, Geneva, 2011.

[37] ATLAS Collaboration. *Expected performance of the ATLAS experiment: detector, trigger and physics.* CERN, 2009.

[38] ATLAS Collaboration. Performance of the Reconstruction and Identification of Hadronic Tau Decays with ATLAS. Technical Report ATLAS-CONF-2011-152, CERN, Geneva, November 2011.

[39] ATLAS Collaboration. $Z \to \tau\tau$ cross section measurement in proton-proton collisions at 7 tev with the atlas experiment. Technical Report ATLAS-CONF-2012-006, CERN, Geneva, February 2012.

[40] J. M. Butterworth, E. Dobson, U. Klein, B. R. Mellado Garcia, T. Nunnemann, J. Qian, D. Rebuzzi, and R. Tanaka. Single boson and diboson production cross sections in pp collisions at $\sqrt{s}$=7 tev. Technical Report ATL-COM-PHYS-2010-695, CERN, Geneva, August 2010.

[41] ATLAS Statistics Forum. ABCD method in searches. 2012.

[42] Z Czyczula, T Przedzinski, and Z Was. Tauspinner program for studies on spin effect in τ production at the lhc. Technical Report arXiv:1201.0117. CERN-PH-TH-2011-307, CERN, January 2012.

[43] Glen Cowan. *Statistical Data Analysis.* Oxford Science Publications, 1998.

[44] F. James. *MINUIT - Function Minimization and Error Analysis - Reference Manual. Version 94.1.* CERN Program Library Long Writeup D506, CERN, Geneva, 1994.

[45] ATLAS Collaboration. Luminosity Determination in pp Collisions at sqrt(s) = 7 TeV using the ATLAS Detector in 2011. Technical Report ATLAS-CONF-2011-116, CERN, Geneva, August 2011.

[46] ATLAS Collaboration. Muon Momentum Resolution in First Pass Reconstruction of pp Collision Data Recorded by ATLAS in 2010. Technical Report ATLAS-CONF-2011-046, CERN, Geneva, 2011.

[47] ATLAS Collaboration. Muon reconstruction efficiency in reprocessed 2010 LHC proton-proton collision data recorded with the ATLAS detector. Technical Report ATLAS-CONF-2011-063, CERN, Geneva, April 2011.